Multiscale thermal hydraulic analysis of fuel assembly and system of SFR

Zur Erlangung des akademischen Grades
Doktor der Ingenieurwissenschaften
von der KIT-Fakultät für Maschinenbau
Karlsruher Institut für Technologie (KIT)

genehmigte
Dissertation
von

M. Sc. Xi Wang

Tag der mündlichen Prüfung: 13. Mai 2019

Hauptreferent: Prof. Dr.-Ing. Xu Cheng

Korreferent: Prof. Dr.-Ing. Thomas Schulenberg

I declare that I have developed and written the enclosed thesis completely by myself, and have not used sources or means without declaration in the text.

Karlsruhe, 13.05.2019

.....

(**Xi Wang**)

Acknowledgements

Great thanks to Prof. Dr.-Ing. Xu Cheng for accepting me as a PhD. student of KIT in 2015. With the precious opportunity, I was able to immerse myself into the academic atmosphere. During the 4 years doctoral study, I was involved in the SESAME H2020 research project for the 4th generation liquid metal cooled nuclear reactor. The project experience and the detailed guidance from Prof. Cheng improved my research skills and also broaden my vision. I would also thank Prof. Cheng for the chance to write this thesis under his supervision.

I would also like to thank Prof. Dr.-Ing. Thomas Schulenberg for being the second expert of this thesis.

Thanks to all my excellent colleagues at IFRT, with whom we learned a lot from each other and had a great time together. Without your suggestions and comments, this thesis would not be what it has become.

At last, I would thank my wife who gave up her position at Beijing to stay together with me in a foreign country. With a great support from my wife, I could focus on my research work.

Xi Wang
Karlsruhe, May 2019

Kurzfassung

Als einer der innovativen nuklearen Reaktoren der vierten Generation, hat der schnelle natriumgekühlte Reaktor (sodium cooled fast reactor SFR) einzigartige Eigenschaften in Bezug auf Wärmeübertragung und Konversionsrate.

Aufgrund des großen Verhältnisses von Brennstoff zu Kühlmittel, werden die Brennstäbe in der Regel in einer dreieckigen Anordnung untergebracht. Schraubenförmige Drahtabstandshalter kommen bei dieser Art von Reaktor zum Einsatz. Ein anderes wichtiges Designmerkmal dieses Reaktortypes ist die sogenannte Pool-Bauweise. Der bekannteste Demonstrationsreaktor dieser Art ist der Phenix Reaktor, der im Jahr 2009 abgeschaltet wurde. Die Weiterentwicklung des Phenix Reaktors ist ASTRID [Le Coz et al. (2011)].

Im Vergleich zu den vielen Erfahrungen aus dem kommerziellen Einsatz von wassergekühlten Reaktoren, resultieren die speziellen Eigenschaften des SFR immernoch in großen Herausforderungen bezüglich der Brennelemente und des Systems. Einige dieser Herausforderungen sind hier aufgelistet.

1. Thermohydraulische Phänomene der Brennelemente
    a) Durch die Abstandshalter verursachte Drall-Strömung
    b) Der lokale Wärmeübergang in den dreieckig angeordneten Brennstäben mit ihren Abstandshaltern
    c) Unterkanal Analyse der Brennelemente unter Berücksichtigung der oben genannten Punkte
2. Thermohydraulische Phänomene des Reaktorsystems
    a) Die lokalen dreidimensionalen Phänomene im Inneren des Pool, welche mit dem gesamten Systemverhalten eng verbunden sind

Die thermohydraulischen Eigenschaften eines SFR-Brennelements sind hauptsächlich durch die schraubenförmigen Abstandshalter, sowie der Anordnung der Brennstäbe bestimmt. Einer der Haupteffekte der Drahtabstandshalter ist das Verstärken des Queraustauschs von Kühlmittel in der dreieckigen Anordnung. Um die Eigenschaften der Kühlmittelströmung zwischen den Brennelementen zu untersuchen, wurden in dieser Arbeit Methoden der numerischen Strömungsmechanik (computational fluid dynamics, CFD) angewandt. Hierzu wurde die Strömung und die Wärmeübertragung in einem 19-Brennstab-Brennelement mit schraubenförmigen Drahtabstandshaltern untersucht. Diese CFD Untersuchungen konzentrieren sich nur auf einen Abschnitt des Brennelements. Die Länge des CFD-Modells, mit periodischen Einlass- und Auslassrandbedingungen beträgt eine Drahtumwendung. Als Turbulenzmodell wurde das $k-\omega$ SST-Modell eingesetzt. Der Einfluss des Drahtabstandhalters auf die Geschwindigkeitsverteilung im Spalt zwischen zwei Unterkanälen wurde untersucht. Basierend auf der Kräftebilanz aus Wake-Kraft und Oberflächenreibungskraft in Umfangsrichtung der Brennstäbe wurde ein theoretisches Modell zur Vorhersage des mittleren Massenstroms der Drall-Strömung, hervorgerufen durch einen einzigen Draht,

abgeleitet. Die Simulationsergebnisse zeigen, dass das Verhältnis aus Brennstababstand (P) zum Brennstabdurchmesser (D) einen großen Einfluss auf die Geschwindigkeit der Drall-Strömung hat. Die normalisierte Drall-Strömungsgeschwindigkeit steigt mit dem P/D Verhältnis an. Die Simulationsergebnisse sind in guter Übereinstimmung mit dem vorgeschlagenen theoretischen Modell. Zusätzlich hat noch das Verhältnis aus Drahtumwendlungslänge (H) und Brennstabdurchmesser einen Einfluss auf den Queraustausch: ein kleines H/D Verhältnis führt zu einem größeren Queraustausch. Eine Korrelation basierend auf beiden Verhältnissen, sowohl P/D als auch H/D, zur Vorhersage der Drall-Strömungsgeschwindigkeit wurde in dieser Arbeit vorgeschlagen.

Aufgrund der Drall-Strömung und der dreieckigen Anordnung der Brennstäbe könnte der Wärmeübergang in Umfangsrichtung der Brennstäbe eine nicht-uniforme Verteilung ausweisen. Eine uniforme Verteilung wurde bisher in den meisten Unterkanalanalysen angenommen. Da das lokale Strömungsfeld zwischen den einzelnen Unterkanälen stark durch die Drahtabstandshalter beeinflusst ist, hängt auch der Wärmeübergang in diesem Breich von der Anordnung der Brennstäbe und deren Abstandhalter ab. Um den lokalen Wärmeübergang der Brennelemente zu untersuchen, wurde der CFD Code OpenFOAM verwendet. Ebenfalls wurde die Wärmestromverteilung auf der Brennstaboberfläche, sowie die Temperaturverteilung auf Brennstab und Abstandshalter analysiert. In dieser Arbeit wurden zwei CFD Modelle zur Untersuchung des Wärmeübergangs verwendet. Ein 19 Brennstab-Brennelement mit Drahtabstandhalter und ein Modell ohne Drahtabstandhalter. Für das Modell ohne Abstandhalter wurde eine periodische Randbedingung eingesetzt, um den Wärmeübergang in der entwickelten Strömung zu untersuchen. Für das 19 Brennstab-Brennelement mit Draht wurden gewöhnliche Einlass- und Auslassranbedingungen gesetzt. Die Länge des Modells betrug zwei Drantumwendungen. Bei beiden Modellen wurden sowohl die flüssigen Regionen, als auch die Festkörper simuliert. Als Turbulenzmodell wurde das k-omega SST Modell verwendet. Die Simulationen zeigen einen kosinusförmigen lokalen Wärmeübergang in Umfangsrichtung der Brennstäbe.

Neben der detaillierten Untersuchung der dreieckig angeordneten Brennstäbe, wurde auch das Unterkanalprogramm MATRA für die Berechnung von flüssigem Natrium erweitert. Hierzu wurden die physikalischen Eigenschaften von Natrium, sowie Korrelationen für Druckverlust, Wärmeübergang und turbulente Vermischung aus vorhandener Literatur entnommen und implementiert. Eine automatische Nodalisierungsfunktion für die Generierung der Eingabedatei wurde entwickelt. Ebenfalls wurde die hier vorgeschlagene Korrelation implementiert, um lokale Oberflächentemperaturen und Wärmeübergangskoeffizienten ausgeben zu können. Schließlich wurde der modifizierte MATRA Code zur Analyse eines Brennelements des ASTRID Reaktors verwendet.

Das thermohydraulische Verhalten des SFR ist maßgebend beeinflusst durch die Poolbauweise. Der Kühlkreislauf weist starke lokale dreidimensionale Phänomene im kalten und heißen Plenum auf. Diese Phänomene sind mit dem gesamten Systemverhalten eng verbunden. In dieser Arbeit wurde der System Code ATHLET und der CFD Code OpenFOAM miteinander verbunden, um den “dissymmetrie Test” des Phenix Reaktors zu simulieren. Die Ergebnisse dieser Simulationen wurden mit experimentellen Daten verglichen und bewertet.

Die wesentlichen Erkenntnisse aus dieser Arbeit sind: (1) Ein neues Modell zur Vorhersage der von Drahtabstandhaltern hervorgerufenen Drall-Strömung wurde vorgeschlagen; (2) Eine neue Korrelation zur Berechnung des Wärmeübergangs bei dreieckig angeordneten Brennstäben wurde aufgestellt; (3) Das Unterkanalprogramm MATRA wurde angepasst, um die Berechnung von Brennelementen von SFR zu ermöglichen; (4) Eine Kopplungsmethode von ATHLET und OpenFOAM wurde angewandt, um den Phenix “dissymmetrie Test” zu simulieren.

Abstract

As one of the innovative 4th generation nuclear reactors, the sodium cooled fast reactor (SFR) has unique advantages on heat transfer efficiency and breeding ratio. Due to the design requirement of a high fuel-coolant ratio, the fuel rods are usually arranged in triangular array. Helical wire spacers are widely used in the sodium cooled fuel assemblies. Another important feature is the pool type design of SFR. The most famous demonstration of SFR is Phenix reactor, which was closed in 2009. The upgraded future design version of Phenix is ASTRID [Le Coz et al. (2011)].

Comparing with water reactors which have a long term commercial operating experience, the special features of SFR result several unique detailed thermal hydraulic issues of fuel assembly and system. The engineering interested several points are listed as below.

1. Thermal hydraulic issues of the fuel assembly
    a) Sweeping flow induced by the special wire spacers
    b) Local heat transfer due to the triangular fuel rod arrangement and spacers
    c) Sub-channel analysis of fuel assembly by considering the above two points
2. Thermal hydraulic issue of the reactor system
    a) The local detailed 3D phenomena inside the reactor pool, which is coupled with the system behavior

The thermal hydraulic of SFR fuel assembly is mainly influenced by its helical spacers and fuel rod arrangement pattern. One of the main effects of the wire spacers is enhancing the inter-channel cross flow in the triangular arrayed rod bundles. To study the characteristic of sweeping flow rate across the gaps between the sub-channels, the computational fluid dynamics (CFD) method is used in the present study to analyze the flow field in a 19-rod bundle with wire wraps. This CFD work only considers the fluid zone of one section of the rod bundle. The height of the CFD model with a periodic inlet and outlet boundary condition is one wire pitch. The $k-\omega$ SST model is used as the turbulent model. The wire effect on the velocity distribution of the flow across the interface between two sub-channels is investigated in the CFD study. Based on the force balance equation between the wire wake force and the surface friction force of rods in the circumferential direction, a theoretical model for estimating the average swirling flow rate driven by one single wire is proposed. The simulation shows that the ratio of rod pitch (P) to rod diameter (D) has a strong effect on the velocity of sweeping flow. The normalized sweeping flow velocity increases with the P/D ratio. The simulation agrees well with the proposed model. In addition, the effect of the ratio of wire pitch (H) to rod diameter has also an influence on the cross flow rate: A small H/D ratio leads to higher cross flow velocity. A correlation as a function of both P/D ratio and H/D ratio is proposed to predict the sweeping flow velocity by the present study.

Relating to the sweeping flow and the triangular arrangement pattern, the circumferential heat transfer of fuel rod may have an uneven distribution rather than the uniform

distribution assumed in most of the sub-channel approaches. Since the local flow field in the coolant flow passage is influenced by the wires, which induce the diversion flow, the circumferential heat transfer of the rod is strongly affected by both the arrangement and the wire spacer. To study the local heat transfer behavior of wire-wrapped rod bundle, the CFD code OpenFOAM is used in present study to figure out the detailed temperature and heat flux distributions on the surface of rod and wire. In present study, two CFD models for both bare rod bundle and wire wrapped 19-rod bundle are created. For the bare rod model, a periodical boundary condition is used to simulate the heat transfer of developed flow. For the wire wrapped 19-rod bundle case, the normal inlet outlet boundary is imposed to the fluid region with a length of two wire pitches. In the CFD studies, the models are split into solid and fluid regions. The k-omega SST model is used for turbulent simulation. The simulation result shows a cosine like local heat transfer distribution in the circumferential direction of the rod.

Besides the detailed investigation of the triangular arrayed fuel assembly, the sub-channel approach code MATRA is improved for the coolant of sodium and local heat transfer calculation. The thermal properties functions for sodium are implemented. The pressure drop correlation, heat transfer correlation and turbulent mixing coefficient for sodium coolant from the literatures are also implemented. An automatic nodalization function is created for generating the input deck. Besides that, the proposed local heat transfer model is implemented for local cladding temperature and heat transfer coefficient output. Finally, the modified MATRA code is used for the fuel assembly analysis of ASTRID reactor.

The thermal hydraulic of SFR reactor system is mainly influenced by its pool type design. The coolant loops of the sodium cooled reactor involve a strong local 3D phenomena in hot plenum and cold plenum, which are coupling with the system behavior. In present study, the system thermal hydraulic code ATHLET and CFD code OpenFOAM are coupled to simulate the dissymmetric test of the Phenix reactor. The simulation results are compared with experimental data.

The main achievements of present study includes: (1) A new physical model is proposed for the sweeping flow induced by the wire spacers; (2) A new local heat transfer correlation is proposed for the triangular arrayed fuel rods; (3) The code MATRA is improved for simulating the fuel assemblies of the sodium cooled reactor; (4) The ATHLET and OpenFOAM coupling scheme is applied to analyze the dissymmetric test of the Phenix reactor.

Contents

Nomenclature

Latin Symbols

Symbol	Dimensions	Description
A	$m^2, -$	area, coefficient
B	$-$	coefficient
C	$-$	coefficient
C_s	$-$	inter-gap sweeping crossflow coefficient
c	m	width of gap
c_p	$J/kg/K$	thermal capacity
D	$m, m, -$	rod diameter, diameter, coefficient
e	$-$	natural number
E	$J/kg, -$	total energy, coefficient
F	$N, -, kg/m^2/s, -$	force, factor, mass flux, fluid part
G	kg/s	mass flow rate
g	m/s^2	gravity
H	m	wire pitch
htc	$W/m^2/K$	heat transfer coefficient
h	J/kg	enthalpy
i	$-$	index
j	$-$	index
k	$m^2/s^2, -$	turbulent kinetic energy, characteristic value
L	m	characteristic length, length
m	$-$	coefficient
n	$-$	normal vector, surface normal, integer number
Nu	$-$	Nusselt number
P	m	rod pitch
p	Pa, m	pressure, perimeter
Pe	$-$	Pelect number
Pr	$-$	Prandtl number
Q	W/m^3	heat source
q	W/m^2	heat flux
q'	W/m	linear power
R	m	radius
r	m	radial distance
Re	$-$	Reynolds number
S	$m, m^2, -$	width of gap, surface area, source term
t	s	time
T	K	temperature
V	$m/s, m^3$	velocity magnitude, volume
u	m/s	velocity
x	m	axial coordinate
$y+$	$-$	dimensionless wall distance
z	m	wire axial position, axial distance

Greek Symbols

Symbol	Dimensions	Description
α	m^2/s	thermal diffusivity
β	m^2/s	turbulent mixing coefficient
ϵ	$-$	error
γ	$^\circ, -$	flow velocity to axis angle, dimensionless radial distance
Γ	m^2/s	diffusivity
λ	$W/(mK)$, $-$	heat conduction coefficient, character value
μ	$Pa \cdot s$	dynamic viscosity
ν	m^2/s	kinematic viscosity
ω	$1/s$	specific dissipation rate
ω'	$-$	turbulent mixing rate
ρ	kg/m^3	density
τ	Pa	shear stress
θ	$^\circ$, $-$	wire incline angle, dimensionless temperature
φ	$^\circ$	circumferential angle
ϕ	$-$	dimensionless forced-flow mixing rate, physical variable
ψ	$kg/s/m^3, -$	interphase mass exchange per unit volume, intermittent factor

Subscripts

Symbol	Dimensions	Description
a	–	axial
av	–	average
b	–	bulk
c	–	cladding
ci	–	cladding inner wall
$circ$	–	circuit
cl	–	cladding
co	–	cladding outer wall
D	–	drag
$drive$	–	driving
e	–	heated
F	–	face
f	–	friction, fuel
$frict$	–	friction
fc	–	fuel center
g	–	gas gap
gap	–	gap
i	–	index
l	–	liquid coolant
L	–	liquid
m	–	melting point
max	–	maximum
o	–	outer, last time step
r	–	rod
t	–	transverse, turbulent
V	–	volume
w	–	wall
W	–	wall

Superscripts

Symbol	Dimensions	Description
$'$	–	linear, sensitive, modified, first order differential
$''$	–	second order differential
$*$	–	normalized
w	–	wire

Abbreviations

Abbreviation	long form
ATHLET	Analysis of THermal-hydraulics of LEaks and Transients
ASTRID	A 600 MW sodium-cooled fast breeder reactor design
ALFRED	The Advanced Lead Fast Reactor European Demonstrator
CAD	Computer Assisted Design
CEA	Alternative Energies and Atomic Energy Commission
CATHARE	A system thermal hydraulic code developed by CEA
CFD	Computational Fluid Dynamics
COBRA	A sub-channel code
DYN2B	A system thermal hydraulic code
ENERGY	A sub-channel code
FVM	Finite Volume Method
GRS	Gesellschaft für Anlagen- und Reaktorsicherheit gGmbH
KAERI	Korea Atomic Energy Research Institute
KIT	Karlsruhe Institute of Technology
LMR	Liquid metal cooled reactor
MATRA	Multichannel Analyzer for steady states and Transients in Rod Arrays
MYRRHA	Multi-purpose hYbrid Research Reactor for High-tech Applications
OpenFOAM	A C++ toolbox for the development of customized numerical solvers
ORRIBLE	A computer code for flow in rod bundle with inlet blockage conditions
Phenix	A small-scale (233 MWe) prototype fast breeder reactor
PWR	Pressurized water reactor
RANS	Reynolds averaged Navier Stokes equations
SESAME	A European H2020 research project for LMR
STH	System thermal hydraulic
SST	Shear stress transport
SABRE4	A sub-channel code
SLTHEN	A sub-channel code
SFR	Sodium Cooled Fast reactor
TRIO-U	A CFD code developed by CEA
TFO	Thermo Fluid Object
THINS	Thermal Hydraulics Inovative Nuclear Systems
UK	United Kingdom

1. Research background

1.1. Motivation

As one of the Generation IV nuclear systems, the liquid metal cooled reactor (LMR) is given a role to the future application of fast reactors for the production of sustainable nuclear energy. LMR is already demonstrated by a lot of national and international projects [Rodriguez et al. (2005), Guidez and Martin (2004), IAEA (2008)]. In Europe, several LMR demonstration projects are undergoing: a sodium cooled fast reactor prototype ASTRID, a multipurpose fast neutron spectrum irradiation facility MYRRHA, and a lead cooled fast reactor ALFRED [Belloni et al. (2011)]. In the framework program of the European community, the THINS project was launched for the fundamental study of the 4th generation reactors [Cheng et al. (2015)]. After the THINS project, the SESAME project continues the research work. SESAME focuses on pre-normative, fundamental, safety-related, generic challenges of LMR.

The liquid sodium cooled fast reactor (SFR) is the most important type of LMR. The liquid sodium coolant removes the heat quickly, and allows higher power density. The study and design work has been carried out for about 60 years [Yamaki et al. (1982)]. During the past decades, our understanding of the SFR has been improved significantly. One of the most outstanding demonstrations of SFR is the prototype reactor Phenix, which has been operated for about 100,000 hours at a core outlet temperature of 560 $^{\circ}C$. The breeding ratio of the Phenix reactor is 1.16, and its thermal efficiency is 45.3% [Sauvage (2004)]. The SFR shows distinguished advantages like the high breeding ratio, and the high thermal efficiency. From the thermal hydraulic point of view, the common features of most designs of SFR are:

1. Liquid sodium is used as the coolant
2. Wire wrapped fuel rods are arranged in a triangular array
3. Pool type design for the primary coolant loop

Concerning the above features, a lot of numerical and experimental studies were carried out for the improvement of the safety and design [Chang et al. (2017), Wang (2017), Wang et al. (2018)]. In the numerical studies, the SFR involves numerous thermal-hydraulics phenomena with different scales, which are shown in Fig. 1.1. The multi-scale thermal-hydraulics numerical approaches for the SFR are:

1. System approach

2. Sub-channel approach
3. CFD approach

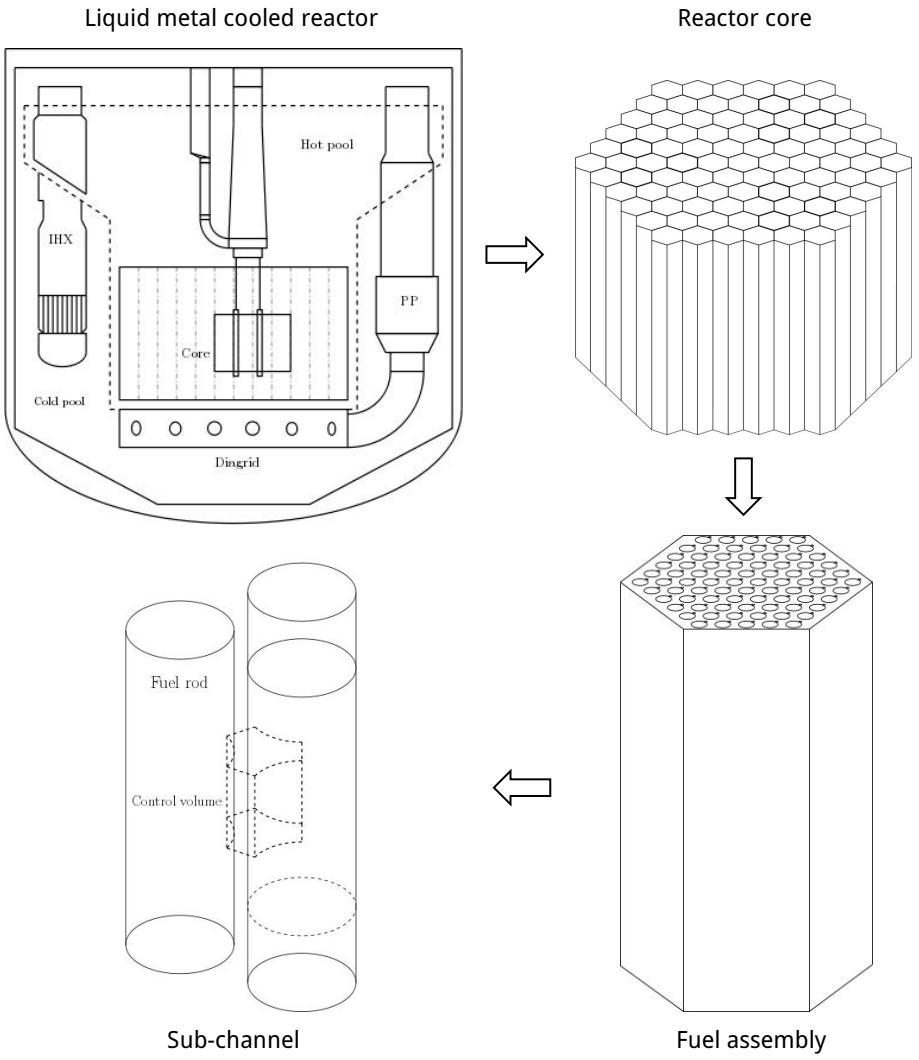

Figure 1.1.: Multiple scales of reactor thermal hydraulics

The methodologies have already been improved within the studies of their respective field. The numerical schemes have been applied in many practical engineering use cases. Based on these already established and proven methods, the idea of combining two or three of them together in one simulation is very interesting [Grunloh and Manera (2017), Bandini et al. (2015), Papukchiev et al. (2015), Wei et al. (2018), Huber (2017)]. With this coupling approach, phenomenon at different scales, such as the system behavior and the detailed local 3D flow, can be resolved in one simulation and the feedback of the different scales is captured by the simulation. For example, the hot pool and cold pool of Phenix reactor can be resolved with CFD for the local phenomena, while the core, pump and IHX can not be represented with the system approach. With the transient STH-CFD simulation of Phenix reactor, the detail local 3D phenomena like the transient primary pump inlet temperature can be solved. So the multi-scale simulations for the thermal-hydraulics of SFR is strongly connected to each other. Besides the system scale simulation, a more detailed solution of the fuel assembly thermal hydraulic issue is also interested by the practical engineering. The most important methodologies for the thermal hydraulic study of fuel assembly are sub-channel approach and CFD approach. Within the sub-channel approach, the coolant flow passage is divided by the rod gaps into different channels which

are represented by control volumes. The local flow and temperature field inside one sub-channel control volume can not be resolved. With the CFD method, the geometry details can be simulated, and the local flow and heat transfer can be solved. While the CFD method can not be used instead of the sub-channel approach, this is because of the its computational cost, and lack of the specific empirical models of the sub-channel approach method. The current system, sub-channel and CFD approaches are numerical methods in different scales.

With the current numerical methodologies, we are still facing some challenges for the SFR thermal hydraulics simulation:

1. Resolve the detailed flow and heat transfer of wire wrapped fuel assembly
2. The coupling simulation of the reactor system for detailed local 3D phenomena

The present work focuses on the research subject related to the above issues. This work involves the CFD approach, the sub-channel approach, and also the system thermal hydraulic approach coupled with CFD. Besides the simulation work, several fundamental mathematical derivations are also carried out to understand the mechanism of the phenomena and figure out the principle of it. The thermal hydraulic study can be divided into two parts, the research points are listed:

1. Thermal hydraulic phenomena of LMR fuel assembly
   a) The sweeping flow of wire wrapped rod bundle
   b) The local heat transfer of rod bundle
   c) Sub-channel scale approach of the fuel assembly
2. Thermal hydraulic phenomena of LMR reactor system
   a) The 3D flow field in the hot and cold plenums of Phenix dissymmetric test

The sweeping flow and local heat transfer are indicated as Fig. 1.2. The local heat transfer is the non-uniform circumferential heat transfer distribution. The non-uniform distribution is resulted by the fuel rod arrangement pattern and the flow field. The sweeping flow refers to the inter-channel cross flow induced by the wire spacers. The cross flow diverted by the spiral wires results the mass exchange between the sub-channels.

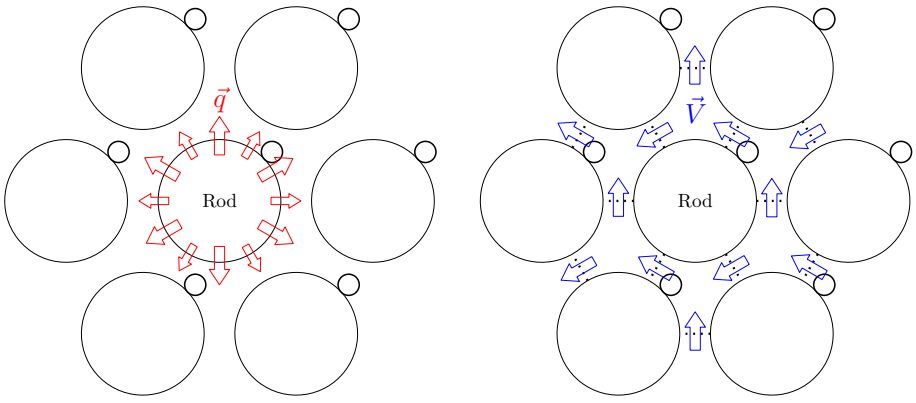

Figure 1.2.: Schematic of local heat transfer and sweeping flow

The thermal hydraulics of LMR is a huge research topic which has been studied by thousands of researchers in the past half century. Based on the previous studies, the present study focuses on the 4 detailed unresolved research points and new engineering applications related to the reactor system and fuel assembly.

1.2. State of the art

Corresponding to the challenges, 4 specific research points are targeted. a literature review focused on the 4 related points is carried out.

Sweeping flow of wire wrapped rod bundle

In the fuel assemblies of the fast reactors, the fuel rods are usually arranged in a triangular array, the aim of the arrangement is to reduce the coolant to fuel ratio. The flow passage of the sub-assembly can be divided into sub-channels by the narrow gaps between the fuel pins. The width of the gap is very close to the diameter of the wires, and the wires of two fuel rods next to each other come into the gap alternatively. The inter-channel cross flow direction also changes periodically. The coolant of the hot channels can be mixed with the coolant from the cold channels as a result of the wire mixing effect, and the cross flow between the flow channels induced by the wire is called sweeping flow. Since one of the design criteria is that the temperature of fuel and cladding should be kept in a safe range to their upper limits [Cha et al. (2018)]. The wires flatten the temperature distribution of the coolant passage of the sub-assembly. So the understanding of the mechanism, and a good prediction of the sweeping flow rate will have a practical engineering value to get a more accurate core thermal hydraulic simulation result.

In the past decades, a lot of numerical approaches and experimental studies were carried out. Numerous models were proposed for the sub-channel analysis. For the sub-channel code, a model named forced flow inter-channels mixing was proposed by Ginsberg (1972). In this model, the normalized transverse flow velocity calculation is purely based on the geometry consideration, and the flow rate is presumed maximum where the wire cross the gap. The cross flow distribution is expressed as a cosine function. The comparison of the forced flow and the turbulent mixing model reveals the inter-channels flow of fuel assembly with the wire spacer systems is dominated by the sweeping flow. The equations of the Ginsberg model is given as following:

$$\phi = F(\frac{P}{D_r}, \frac{H}{D_r}, Re)\frac{D_r + D_w}{H} \tag{1.1}$$

where ϕ is the dimensionless cross flow rate magnitude. D_r and D_w are the rod diameter and the wire diameter. H is the helical wire pitch. F is a function of $\frac{P}{D_r}$, $\frac{H}{D_r}$, and Reynolds number Re. The quantity F must be obtained from experiment [Ginsberg (1972)]. The cross flow distribution is well represented by

$$u_t^* = \frac{u_t}{u_a} = \phi \cos(2\pi \frac{z}{H} + \varphi_0) \tag{1.2}$$

where u_t^* is the normalized transverse velocity, which equals to the ratio of transverse velocity u_t and axial mean velocity u_a. φ_0 represents the initial wire off gap angle at the inlet position of the rod bundle.

In the sub-channel code ORRIBLE, an approximate correlation was proposed by Wantland (1974) to predict the pressure diversion cross flow due to the wire wrap. The turbulent mixing and transverse thermal conduction were considered here. In this kind of sub-channel approaching, the investigation assumes the flow direction goes with the helical wire, and the maximum transverse velocity is also assumed to occur on the position where the wire spacer crosses the gap, and the wire spacer is assumed to occupy no flow area. Within this assumption, the ratio of transverse flow velocity to axial velocity is obtained from the wire to axial angle. If the wire position is more than 60 degrees from the gap, the influence is assumed negligible. For less than 60 degrees, the flow is strongly influenced by the wire. This model is also simply based on a geometrical consideration that the flow

velocity direction is parallel to the wire spacer. The Wantland model is given as following equation:

$$u_t^* = \frac{u_t}{u_a} = C_S \frac{\pi(D_r + D_w)}{2H}[1 + \cos(3\varphi)] \quad for \quad |\varphi| < 60^\circ \tag{1.3}$$

where C_s is a user given coefficient, it can be obtained from the experimental study. φ is the wire off gap angle, which is illustrated as Fig. 1.3.

$$u_t^* = \frac{u_t}{u_a} = 0 \quad for \quad |\varphi| > 60^\circ \tag{1.4}$$

where the "angle of influence" of the wire wrap for interior gap sweeping cross flow is 120 degree.

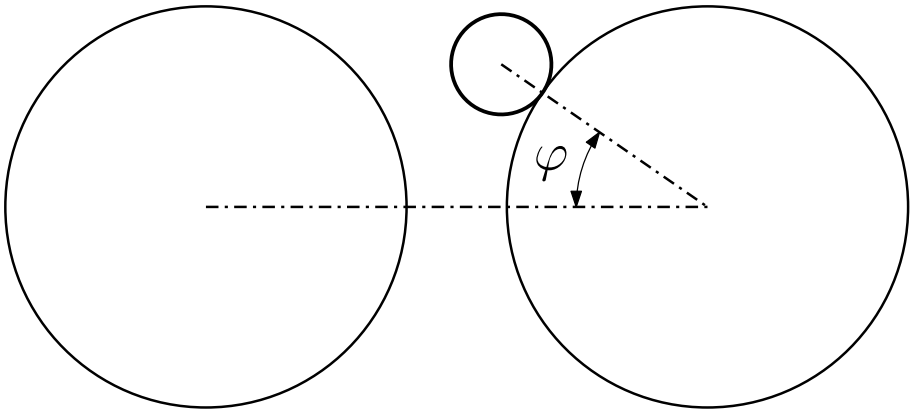

Figure 1.3.: The wire off gap angle

Ninokata et al. (1987) proposed the distributed resistance model as an alternative model to the forced flow inter-channels mixing model. The force exerted on the fluid by the solid is called the distributed resistance term. It includes the friction and form drag from the surface of rod and wire.

In recent 10 years, the computational fluid dynamics(CFD) technology was widely used in the reactor core thermal hydraulic design. Hu and Fanning (2013) developed a momentum source model to simulate the anisotropic flow in the wire wrap pin bundle without the need to resolve the geometry details of the wire. The source term is only dependent on the local velocity profile. Both CFD models of complex geometry and bare bundle with momentum source term are evaluated. A CFD simulation from Raj and Velusamy (2016) gives the prediction result of the friction factor, Nusselt number, and transverse flow rate. An empirical correlation based on CFD simulation results was given by Raj and Velusamy (2016), the correlation gives a more accurate prediction on the position of the maximum transverse velocity compared with Wantland correlation. Although the maximum velocity position has been figured out with the CFD results, the transverse flow rate is estimated in a similar way to the sub-channel approach, a linear regression to the ratio of wire pitch to rod diameter and the axial mean velocity. The empirical correlation obtained by Raj and Velusamy (2016) from his CFD study is given as:

$$u_t^* = \frac{u_t}{u_a} = \frac{1.5\pi(D_r + D_w)}{H}\left(\cos\varphi + \frac{N}{2}\cos(6\varphi)\right) \tag{1.5}$$

where N is a user coefficient defined as

$$\begin{aligned} N = 1 \quad & for \quad (110^\circ < \varphi < 120^\circ) \\ N = -1 \quad & for \quad (290^\circ < \varphi < 310^\circ) \\ & else \quad N = 0 \end{aligned}$$

In conclusion, as shown in Eqn. 1.2, the sweeping flow distribution in axial direction should be a function of rod pitch to rod diameter ratio (P/D), wire helical pitch to rod diameter ratio (H/D), and Reynolds number (Re). The study of Zhao et al. (2017) figured out the normalized transverse flow velocity is independent of the Re. All the previous studies assume it only depends on the H/D ratio. None of the previous studies figured out the effect of the P/D ratio. As a key design parameter, the P/D effect still requires a further study. The motivation of this work is giving a better correlation with a physical explanation of the effects of the main geometry parameters. In some previous studies, diameter D refers to the sum of the rod diameter D_r and the wire diameter D_w. In the present study, D indicates the rod diameter D_r.

Local heat transfer of rod bundle

The local heat transfer of the rod bundle is mainly affected by both the shape of the cross section of the sub-channel and the wire spacer. A few experimental and theoretical studies have been performed for water cooled reactors and liquid metal cooled reactors.

One experimental study carried out by Subbotin et al. (1961) investigated the heat transfer in mercury and water in packed bare rods. In this experiment, the rods contact each other, so the P/D ratio is 1.0. The 7 rods bundle was heated by electricity. An obvious non-uniform distribution of the surface temperature was found in the test. The study also gives a procedure for an approximate thermal calculation.

A theoretical analysis dealing with the heat transfer of a 2D bare rod was given by Nijsing and Eifler (1969). In this study, the symmetrical boundary condition was used for a two dimensional finite element of fuel rod and coolant. The energy equations for the fuel, gas gap, cladding and coolant are solved. Finally, the semi-analytical solution gives the distribution function of the temperature of cladding, and the distribution of the surface heat flux. The result shows the local heat transfer of a bare rod bundle depends on the geometry parameter and the thermal properties of fluid and the flow condition. This kind of theoretical method can be used for both rectangular and triangular rod bundles. The correlation is available for both laminar flow and turbulent flow. The equation for the circumferential temperature is given as:

$$\frac{T_{o,cl} - T_{o,cl,av}}{q'} = \frac{1}{2\pi\lambda_c} \sum_{n=1}^{N} (E_n + F_n) \cos(sn\varphi) \tag{1.6}$$

where $T_{o,cl}$ is the cladding outer surface local temperature, $T_{o,cl,av}$ refers to the outer surface average temperature. q' is the linear power. λ_c is the thermal conductivity of the cladding material. The coefficients E_n and F_n are determined by the boundary and continuity conditions. s denotes the rod array number($s = 6$ for a triangular array, $s = 4$ for a rectangular array).

In the research work carried out by Cheng and Yu (2009), both the experimental and CFD studies were used to investigate the local heat transfer of 7 bare rods. In the experimental study, Freon was used as the working fluid in the loop with a pressure from 1 to 3 MPa. The length of the test section is 1.24 m of which only 0.6 m is heated with a uniform power. The rod diameter is 9.5 mm, and the rod pitch is 10.9 mm. The 7 rods are arranged in a triangular array. In the experiment, the mass flow rate range is 1 to 6 kg/m^2s. The test gives the surface temperature distribution of the rod in the circumferential direction. Besides the experimental study, the CFD method is also used to study the non-uniform distribution of the heat transfer. CFD result shows a strong non-uniform distribution of temperature on the rods. The study suggests further improvements on the sub-channel approach and the CFD simulations are required.

In the study of Yang et al. (2013), a semi-analytical solution of the temperature distribution of the rod bundle was obtained based on the theoretical results and CFD sensitivity analysis. The correlation was implemented into a sub-channel code. The correlation proposed by T. Yang for the central sub-channnel is given as

$$\frac{htc(\varphi)}{htc_{av}} = 1 - \frac{\cos(4\varphi)}{1 + c_0(P/D-1)^{n_1} Pr^{n_2}(\lambda_c/\lambda_l)} \tag{1.7}$$

where $htc(\varphi)$ is the local heat transfer coefficient, and htc_{av} is the average heat transfer coefficient. λ_c and λ_l represent the heat conductivity of the cladding material and the liquid coolant. c_0, $n1$ and $n2$ are fitting coefficients defined by the author. φ is the circumferential angle around the fuel rod.

The research work of Yang et al. (2013) focuses on the bare rod bundle, so the proposed correlation and CFD models are only for the bare rod bundle. The local heat transfer of wire wrapped rod bundle is not investigated in the previous works.

Sub-channel approaches for LMR

The sub-channel approach is widely used to analyze the thermal-hydraulics behavior of the fuel assemblies in nuclear reactors. In the sub-channel codes, the mass conservation equation, axial momentum equation, lateral momentum equation, and energy equation are solved with the initial boundary conditions, as introduced by Stewart et al. (1977). The sub-channel code was firstly used for the water reactors, and great effort was devoted to improve it for the liquid metal cooled reactors. As mentioned in the work of Dobson and Neill (1992), SABRE4 is a 3D sub-channel code for the sodium cooled fast reactor, and it is widely used in UK. SLTHEN is a modified version of ENERGY specifying on LMR. The computational efficiency was also improved by Yang (1997). COBRA-LM is developed from the code of COBRA-IV by Liu and Scarpelli (2015) to deal with the liquid sodium and lead-bismuth eutectic cooled bundles, and confirmed by benchmark analysis.

The original MATRA code was developed by Yoo et al. (1999) from KAERI. This code is used for calculating the enthalpy and flow distribution in the fuel rod bundle elements. But the code of MATRA is designed for the single and two phase flow problems of PWR. MATRA-LMR is an improved version from the code MATRA by Kim et al. (2002). In the present study, the source code MATRA-X0 is only available for water cooled rod bundle. The research on sub-channel approach in present study is based on the code MATRA-X0.

Coupling simulation of the coolant loop of SFR

Phenix is a pool type reactor equipped with three sodium secondary loops. The nominal power of Phenix reactor is 560 MWt/250 MWe. Before the shut down of the Phenix sodium cooled reactor in 2009, several ultimate tests were performed to provide the validation data for future development of numerical tools. During the final test, one secondary loop was not available due to safety constraints. In the frame of the THINS project, the natural circulation test was selected for the benchmark. In this project, CEA, IRSN and KIT used different codes (CATHARE, DYN2B and ATHLET) to simulate the benchmark test. More detailed information is given in the publication of Pialla et al. (2015). The scenario of the final natural circulation test was introduced in the article written by Gauthé et al. (2012). The main phenomena involved in the transient includes: (1)The reactor was stabilized at a power of 120 MWt and a core inlet temperature of 360 °C, with the three primary pumps in operation, but one secondary circuit not operating. (2) Manual dry-out of the two steam generators to reduce the temperature difference between the primary and secondary sodium at the inlet of the intermediate heat exchanger. (3) Manual scram 460 s later when this difference of temperature (primary and secondary IHX inlet temperatures)

was lower than 15 °C. (4) Manual trip on the three primary pumps 8 s after the scram, with pumps speed decreasing to zero on their own inertia. (5) Secondary pumps speed decreases automatically to 110 rpm in about 1 min after the scram. (6) Onset and development of natural convection in the primary circuit. (7) Three hours later, opening of the steam generator casing, which induced an efficient air natural circulation in the steam generator and the recovery of an efficient heat sink.

In the work carried out by CEA, the CATHARE code is coupled with TRIO-U. CATHARE is a system thermal hydraulics code. A further development and validation for new fluid calculations was carried out by Tenchine et al. (2012). TRIO-U is a CFD code which is designed for general purpose industry calculations. The coupling between CATHARE and TRIO-U is done with an overlapping method. The system-code gives mass flow rate and temperature conditions at the CFD boundaries. The CFD domains give momentum and enthalpy feedback to the system code.

The ATHLET 2.2 code was improved for SFR by Zhou et al. (2013) and Huber (2017) from KIT. To extend the ATHLET code's application range to SFRs, a property package calculating the sodium thermo-physical and transport properties was implemented into the code. This modified version of ATHLET was coupled with an open source CFD code OpenFOAM. The region of the primary circuit is calculated with CFD (hot plenum) in the coupled simulation with ATHLET and OpenFOAM. For the hot plenum CFD calculation, a RANS (Reynolds Averaged Navier Stokes) with $k-\omega$ turbulence model and wall functions is used. The fluid properties are specified with temperature dependent polynomial functions. At the inlets, the turbulent intensity and the turbulent mixing length are specified for k and ω. The values of mass flow rate, temperature and pressure must be exchanged from ATHLET to OpenFOAM as boundary conditions. The developed methodology considers an iterative approach. The full transient is iterated between ATHLET and OpenFOAM. As soon as exchanged values show non-significant changes at boundaries in comparison to the previous result, iterations are stopped.

In the study of Huber (2017), the ATHLET-OpenFOAM coupling scheme is already applied on the Phenix Natural Circulation test. A further simulation of the Phenix dissymmetric test is required to be carried out in the frame of SESAME 2020 project. The coupling simulation in present study is mainly an engineering application on the Phenix dissymmetric test.

1.3. Objective

The present work focuses on the thermal-hydraulics of the liquid sodium cooled fast reactor. The main research targets are:

1. Improvement of thermal hydraulic analysis of fuel assembly of LMR
    a) Develop a new sweeping flow correlation for wire wrapped fuel assembly based on a force balance model
    b) Derive a new local heat transfer correlation for the triangular arrayed rod bundle by considering the sweeping flow
    c) Improve the MATRA-X0 code for LMR, and implement the local heat transfer correlation for detailed circumferential heat transfer output.
2. Thermal hydraulic analysis of LMR system
    a) Application of ATHLET-OpenFOAM coupling scheme to Phenix dissymmetric test

The present study involves mathematical solution, sub-channel approach, CFD simulation and system calculation. The engineering application of present work is mainly for the Phenix reactor and its next generation ASTRID reactor.

2. Thermal hydraulic simulation methods

In the present study, multi-scale simulation methods are used for the study of the thermal hydraulics of the fuel assembly and the primary loop of the sodium reactor. The CFD approach is used for a detailed high resolution simulation of fuel rod bundle and reactor pool. The sub-channel approach is used to get practical engineering results for the fuel assembly. The system thermal-hydraulics (STH) approach is based on the lump parameter method and 1D simulation method. The reactor core, heat exchangers and primary pumps are simulated with the STH code. Governing equations for multi-scale approaches are given as below.

2.1. Governing equations

The liquid sodium coolant of SFR is a special fluid. The governing equations for fluid are similar for the numerical approaches with different scales. Based on the Eulerian system, the general governing equations are given as below.

Mass continuity equation:

$$\frac{\partial \rho}{\partial t} + \nabla \cdot (\rho \vec{u}) = 0 \tag{2.1}$$

where ρ is density, and t is time. $\vec{u}$ is the flow velocity vector.

Momentum equation:

$$\frac{\partial (\rho \vec{u})}{\partial t} + \nabla \cdot (\rho \vec{u} \vec{u}) = -\nabla p + \rho \vec{g} + \nabla \cdot \tau \tag{2.2}$$

where p is pressure, $\vec{g}$ is gravity, τ is the derivatoric stress tensor.

Energy equation:

$$\frac{\partial (\rho E)}{\partial t} + \nabla \cdot (\rho \vec{u} E) + \nabla \cdot (\vec{u} p) = -\nabla \cdot \vec{q} + \nabla \cdot (\tau \cdot \vec{u}) + \rho \vec{u} \cdot \vec{g} \tag{2.3}$$

where E is the total energy, and $\vec{q}$ is the heat flux.

The general governing equations are applicable for most of the engineering problems. Some terms should be omitted or added for some special issues. Depending on the physical issue, the additional transportation equations may be required for turbulence, void fraction or concentration.

For CFD, sub-channel and system thermal-hydraulics approaches, the governing equations are quite similar, the only differences are the equation transformation, simplification and source terms. In sub-channel and STH approaches, more empirical models are implemented. All the three different numerical schemes are based on the finite volume method. One of most important differences between CFD, sub-channel and system approaches is the definition of their control volumes, which are specified on different geometry shapes with different scales.

2.2. CFD approach

The governing equations for the CFD approach are almost the same as the general governing equations. The main difference is the expansion and deformation of the momentum equation and the energy equation [Jasak et al. (2007)]:

Momentum equation:

$$\frac{\partial(\rho\vec{u})}{\partial t} + \nabla\cdot(\rho\vec{u}\vec{u}) = -\nabla p + \rho\vec{g} + \nabla\cdot(2\mu_{eff}D(\vec{u})) - \nabla(\frac{2}{3}(\nabla\cdot\vec{u})) \tag{2.4}$$

where μ_{eff} is the effective viscosity, and the rate of strain tensor is defined as

$$D(\vec{u}) = \frac{1}{2}(\nabla\vec{u} + (\nabla\vec{u})^T) \tag{2.5}$$

Energy equation:

$$\frac{\partial(\rho h)}{\partial t} + \nabla\cdot(\rho\vec{u}h) + \frac{\partial(\frac{1}{2}\rho|\vec{u}|^2)}{\partial t} + \nabla\cdot(\rho\vec{u}\cdot\frac{1}{2}|\vec{u}|^2) - \frac{\partial p}{\partial t} = \nabla^2(\alpha_{eff}h) + \rho\vec{u}\cdot\vec{g} \tag{2.6}$$

where h denotes enthalpy, and α_{eff} is effective thermal diffusivity.

The governing equations of the solver for different engineering problems are slightly different, for example the buoyancy term is added to the momentum equation when buoyant approximation is adopted. The governing equations for the steady state can be obtained by removing the time dependent terms. The turbulence is simulated with RANS/LES models [Robertson et al. (2015)].

The control volumes in CFD are the cells, and the cells can be in a shape like hexahedron, prism, tetrahedron. The parameters in the finite volume discretisation are illustrated as Fig. 2.1. Within finite volume method, the governing equations should be integrated over the volume of the cell.

The Laplacian term is integrated over the control volume and linearized as follows:

$$\int_V \nabla\cdot(\Gamma\nabla\phi)dV = \int_S d\vec{S}\cdot(\Gamma\nabla\phi) = \sum_f \Gamma\vec{S}_f\cdot(\nabla\phi) \tag{2.7}$$

where Γ represents the diffusion coefficient, ϕ is the physical quantity. V is the volume, and S is the surface area, and f indicates the surface patch.

When the length vector d between the interest cell P and its neighbour cell N is orthogonal to the face panel, the face gradient discretization is implicit.

The convection term is integrated over a control volume and linearized as follows:

$$\int_V \nabla\cdot(\rho\vec{u}\phi)dV = \int_S d\vec{S}\cdot(\rho\vec{u}\phi) = \sum_f \vec{S}_f\cdot(\rho\vec{u})_f\phi_f = \sum_f \vec{F}\phi_f \tag{2.8}$$

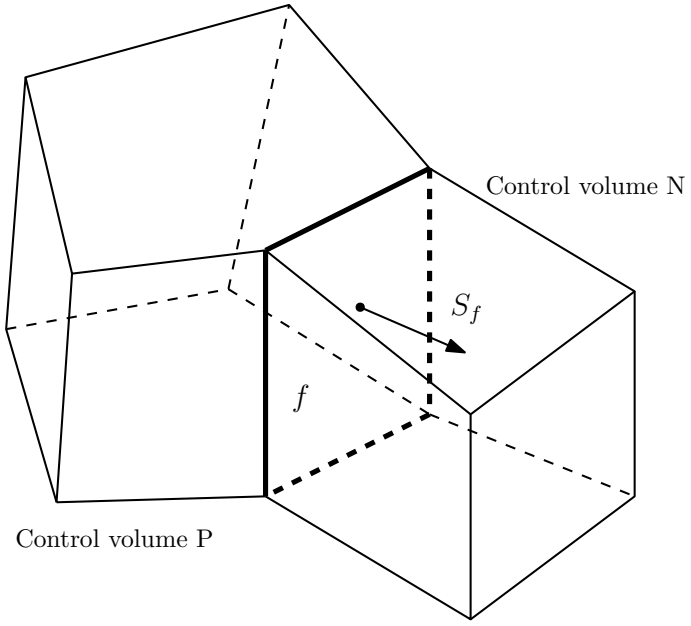

Figure 2.1.: Parameters in finite volume discretization of OpenFOAM

where $\vec{F}$ is the mass flux on the surface of control volume.

The face field can be evaluated using different schemes: central differencing, up-wind differencing and blended differencing.

The first time derivative term is integrated over the control volume and discretized by the Euler implicit scheme:

$$\frac{\partial}{\partial t}\int_V \rho\phi dV = \frac{(\rho_p\phi_p V)^n - (\rho_p\phi_p V)^o}{\Delta t} \tag{2.9}$$

where n and o refer to the new time step and the old time step. The subscript p indicates the present control volume.

For further information about the numerical scheme of OpenFOAM, see reference OpenFOAM (2011).

2.3. Sub-channel approach

The MATRA code is based on the finite volume method in an Eulerian system [Stewart et al. (1977)]. One sub-channel is discretized into a number of volumes in axial direction. The control volume of the sub-channel is shown as Fig. 2.2. In this figure, F refers to the fluid part of the surface area, and W is the wall portion of the surface area. $\vec{n}$ is the outward surface normal vector. The volume of the control volume is V. With the integration operation over the control volume, the integral form of governing equations can be formed.

Mass continuity equation:

$$\frac{\partial}{\partial t}\int_V \rho \mathrm{d}V + \int_F \rho(\vec{u}\cdot\vec{n})\mathrm{d}A = 0 \tag{2.10}$$

Momentum equation:

$$\frac{\partial}{\partial t}\int_V \rho\vec{u}\mathrm{d}V + \int_F \rho\vec{u}(\vec{u}\cdot\vec{n})\mathrm{d}A = \int_V \rho\vec{g}\mathrm{d}V - \int_F p\vec{n}\mathrm{d}A + \int_F (\tau\cdot\vec{n})\mathrm{d}A - \int_W p\vec{n}\mathrm{d}A + \int_W (\tau\cdot\vec{n})\mathrm{d}A \tag{2.11}$$

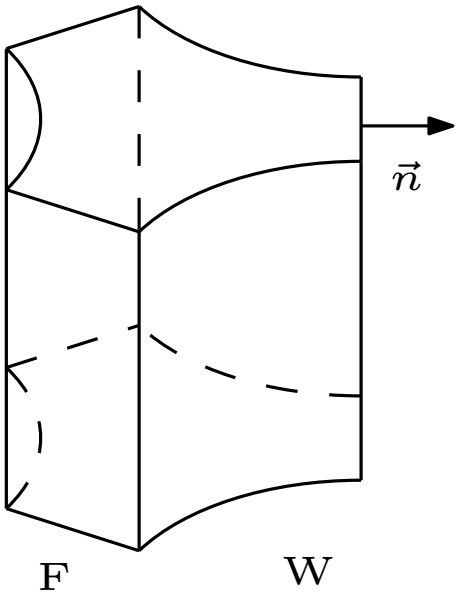

Figure 2.2.: Wall portion and fluid portion of a sub-channel

The momentum equation shown as above is split into an axial equation and a lateral equation in the discretization. So MATRA is more close to a two dimensional solver. For the lateral momentum equation, the pressure loss through the gap is modeled by an overall loss coefficient, which accounts for friction as well as the form drag caused by the area change [Stewart et al. (1977)].

$$F_d = \frac{1}{2} K_G < \rho v^2 >_S S\Delta X \tag{2.12}$$

where S is the gap width, and K_G is the drag coefficient. The definitions of the rest parameters are given in Fig. 2.3.

The inter-channel sweeping flow is obtained by the net pressure and the inter-channel resistance calculations. Instead of the numerical calculation with sub-channel approach, an alternative algebraic calculation with a derived correlation is proposed in Chapter 3.

Energy balance equation

$$\frac{\partial}{\partial t}\int_V \rho h \mathrm{d}V + \int_F \rho h(\vec{u}\cdot\vec{n})\mathrm{d}A = -\int_F \lambda(\Delta T\cdot\vec{n})\mathrm{d}A + \int_W htc(T_W - T_F)\mathrm{d}A \tag{2.13}$$

where h is the enthalpy, and λ is the thermal conductivity. htc is the heat transfer coefficient.

In the energy equation, both the wall temperature T_W and the heat transfer coefficient htc are considered as a uniform distribution in the circumferential direction of the fuel rod. T_F is the bulk temperature of the fluid. The detailed non-uniform heat transfer around the fuel rod will be discussed in Chapter 4.

2.4. System approach

The code ATHLET is designed for both water and liquid metal fluids [Austregesilo et al. (2012)]. For water, both the liquid and vapor phases are solved. In the present study, the coolant is liquid sodium. For sodium, only the liquid phase is simulated. Since the void fraction is 0, the one dimensional governing equations for the liquid phase are:

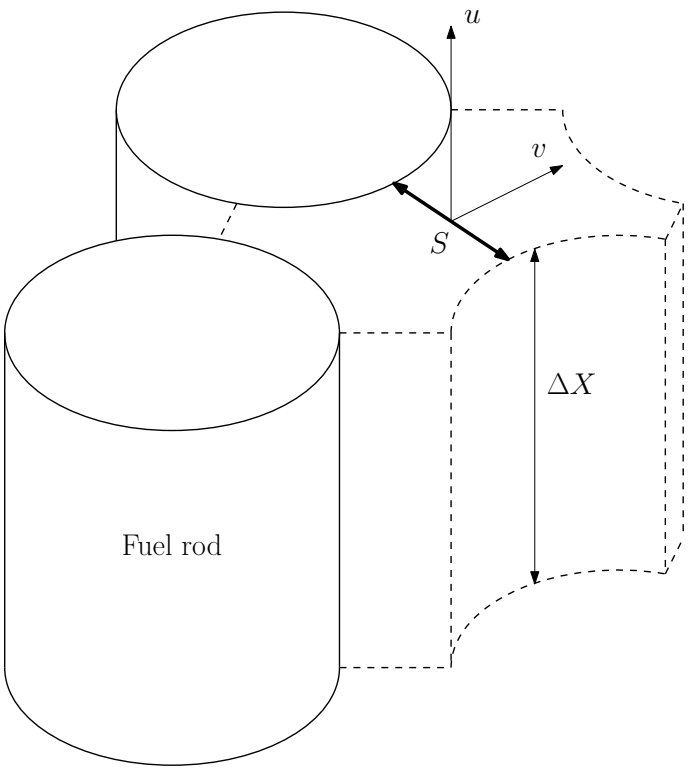

Figure 2.3.: A sub-channel control volume

Liquid mass equation:

$$\frac{\partial \rho_l}{\partial t} + \nabla \cdot (\rho_l \vec{u}_l) = 0 \tag{2.14}$$

where $\vec{u}_l$ refers to the velocity of liquid phase in the one dimensional control volume. The subscript l refers to the liquid phase, while the governing equations for the vapor phase is not introduced here.

Liquid momentum equation:

$$\frac{\partial \rho_l \vec{u}_l}{\partial t} + \nabla \cdot (\rho_l \vec{u}_l \vec{u}_l) + \nabla p = \vec{f}_w - \rho_l \vec{g} + S_{I,l} \tag{2.15}$$

where the terms on the right hand side are wall friction $\vec{f}_w$, gravitation $\rho_l \vec{g}$ and external momentum source terms (e.g. pumps) $S_{I,l}$.

Liquid energy equation

$$\frac{\partial \left[\rho_l (h_l + \frac{1}{2}\vec{u}_l \vec{u}_l) - \frac{p}{\rho_l}\right]}{\partial t} + \nabla \cdot [\rho_l \vec{u}_l (h_l + \frac{1}{2}\vec{u}_l \vec{u}_l)] = \vec{\tau}_i \vec{w}_l + \dot{q}_{wl} + S_{E,l} \tag{2.16}$$

where the terms on the right hand side are shear work $\vec{\tau}_i \vec{w}_l$, heat flux $\dot{q}_{wl}$ and external energy source terms $S_{E,l}$.

As illustrated in Fig. 2.3, the thermal-fluiddynamic object of ATHLET is composed of two basic elements: the control volumes and their interconnections, called junctions. The control domain of the junction is defined between the centers of adjacent control volumes. This leads to a staggered grid.

Taking the mass conservation equation as an example here: by using Gaussian integral law and integrating over a control volume, the mass conservation equation can be written in the form:

$$\int_V \frac{\partial \rho_l}{\partial t} dV + \int_A \rho_l \vec{u}_l d\vec{A} = -\int_V \psi dV \tag{2.17}$$

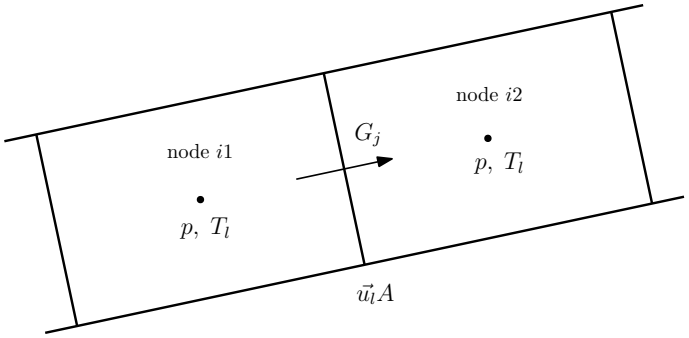

Figure 2.4.: Displaced grid of CVs and junctions

where ψ is the inter phase mass exchange per unit volume.

Performing the integration, the following equations are obtained:

$$\frac{dM_l}{dt} = \sum_{in} G_l - \sum_{out} G_l - \psi \tag{2.18}$$

where G is the mass flow rate through the control volume interface.

The integration of momentum and energy equations are similar. The physical models used in ATHLET are more close to the lump parameter method. For example, the wall friction model for laminar flow is based on the Hagen - Poiseuille correlation for a one dimensional pipe. The pump is simulated by an special thermal-fluiddynamic object with different pump models. For further information, please find it in [Austregesilo et al. (2012)].

2.5. Comparison of the 3 approaches

The three different approaches are all based on the finite volume method within the Eulerian system. The governing equations are very similar. The main difference between the three approaches are:

1. The shape of control volumes are different: (1) The control volume of CFD simulation is the mesh with varying shapes like Hexahedron, pyramid and Wedge; (2) The sub-channel approach has a unique shape of the control volumes specified by the sub-channel; (3) In most cases, the control volume of STH is one dimensional. The discretisation form of the governing equations are dependent on the control volumes.

2. The number of dimensions are different: (1) CFD is a two or three dimensional solver; (2) The sub-channel code split the momentum equation into an axial one and a lateral one, so it is a 2 dimensional approach; (3) The STH code is usually a 1 dimensional code, the velocity has only one component.

3. The physical models are totally different: (1) CFD code is a general fluid dynamics code. Pressure drop and heat transfer are solved by transport equations and the selected turbulence model; (2) A lot of empirical correlations obtained from the sub-channel experimental studies are implemented into the sub-channel approaches, for example the turbulent mixing model and pressure drop model; (3) The models for STH are usually based on experiments of pipe flow, for example the wall friction model.

For further detailed information about the physical models of the three approaches, please find it in the relevant literature [Jasak et al. (2007), Stewart et al. (1977), Austregesilo et al. (2012)].

3. Inter-channel sweeping flow

In the thermal-hydraulic analysis of the reactor core, the coolant flow passage can be divided into sub-channels by the narrow gaps between the fuel rods. In SFR fuel assembly, with the effect of the helical wire spacers, the flow is diverted from one sub-channel to another. The inter-channel sweeping flow plays an important role for the inter-channel mass, energy and momentum exchange. To estimate the sweeping flow rate, the models proposed by Wantland (1974), Ginsberg (1972) and Raj and Velusamy (2016) are based on a simple geometry consideration of the H/D ratio. In the present study, a further investigation of the P/D ratio is carried out. The present study includes theoretical derivation and CFD simulation.

3.1. Theoretical model

The introduction of the theoretical model for inter-channel sweeping flow starts from the definition of the geometric parameters. The most crucial geometry parameters are shown on Fig. 3.1. The pitch of rods P refers to the distance between the center points of two rods, while the wire pitch H refers to the length of one section of the wire spacer. Usually, the gap width is very close to the diameter of the wire. In SFR fuel assembly, the fuel rods are packed tightly together with a spacing of the wire spacer. The P/D ratio is the most important parameter in the fuel assembly design. The position in axial direction z can also be represented by the wire position angle φ.

$$\varphi = 2\pi \frac{z}{H} \tag{3.1}$$

where z is the position in axial direction. φ can be used to indicate the relative wire off gap angle, if the start point is assumed at the position where the wire moves across the gap. Both z and φ can be considered as relative values. In the present study, φ refers to the "wire off gap" angle, which is illustrated as Fig. 1.3.

The normalized sweeping flow velocity across the gap is the ratio of average transverse flow velocity to axial mean velocity over a specified cross section. The normalized sweeping flow velocity is defined as

$$u_t^*(\varphi) = \frac{u_t(\varphi)}{u_a} = \frac{1}{cu_a} \int_0^c \vec{u}_t(\varphi) \cdot \vec{n} \mathrm{d}x \tag{3.2}$$

where $c = P - D_r$ is the width of gap, and u_a is the average velocity of the axial flow. $\vec{n}$ is the normal vector of the gap panel. Transverse velocity u_t is a function of the wire off gap angle φ.

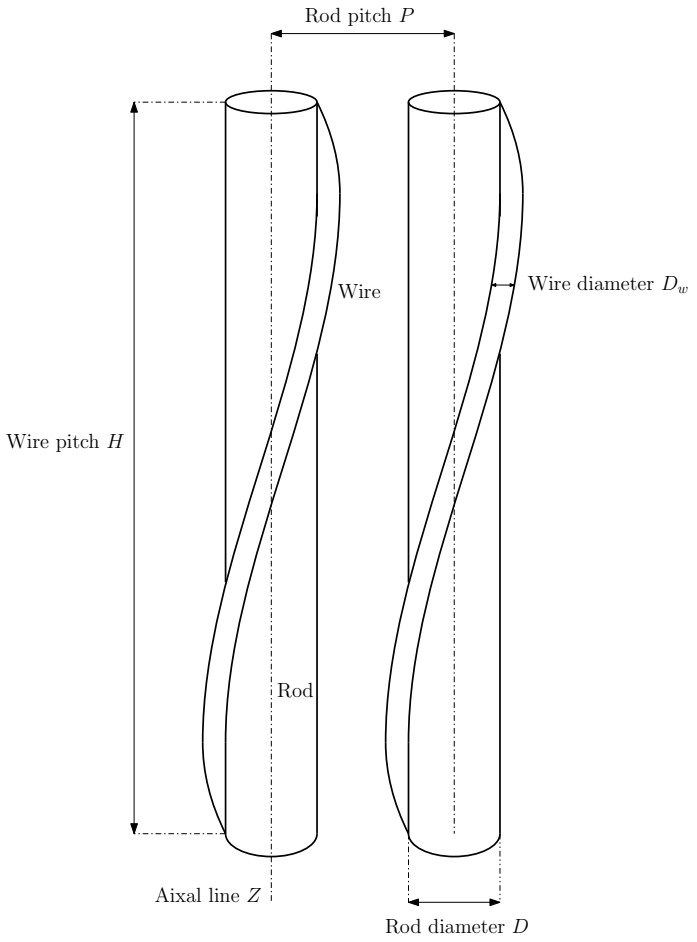

Figure 3.1.: Schematic diagram of rods and wires

As given in Eqn. 3.2, the normalized sweeping flow velocity is a function of the wire position angle. Because the wires of the two neighbour rods enters into the gap alternatively, the sweeping flow velocity magnitude and direction are both affected by the wires. The change of the sweeping flow velocity is usually assumed as a cosine like periodical distribution. But the magnitude of the normalized sweeping flow velocity requires a theoretical investigation. A correlation with a physical explanation is required, and both P/D and H/D effects should be investigated.

Instead of diving into a real wire wrapped fuel assembly, the present study starts from figuring out the mechanism of the transverse flow velocity magnitude of a hypothetical single wire wrapped rod in a group of bare bundles. In this case, only the central rod is wrapped with a wire spacer, the surrounding ones are bare rods. The transverse sweeping flow is considered to be driven by the circumferential pressure difference which is induced by the wake effect of the only helical wire spacer. When the fluid flows across the wire, the pressure difference between the upwind side and the behind side of the wire drives the fluid flowing across the gaps. In previous studies, the flow is assumed to be going along with the wire, so the flow velocity direction is the same as the wire direction. The transverse flow rate can be obtained with the simple geometry consideration. If the flow direction is parallel to the wire, the velocity component perpendicular to the wire is 0, then the driving force for the circumferential flow would disappear. Obviously, this is a paradox. The present study is going to figure out if the flow direction is parallel to the wire or not.

In the present study, the flow direction is assumed to be not parallel to the wire, so there must be an angle between flow direction and wire direction. As shown in Fig. 3.2, the

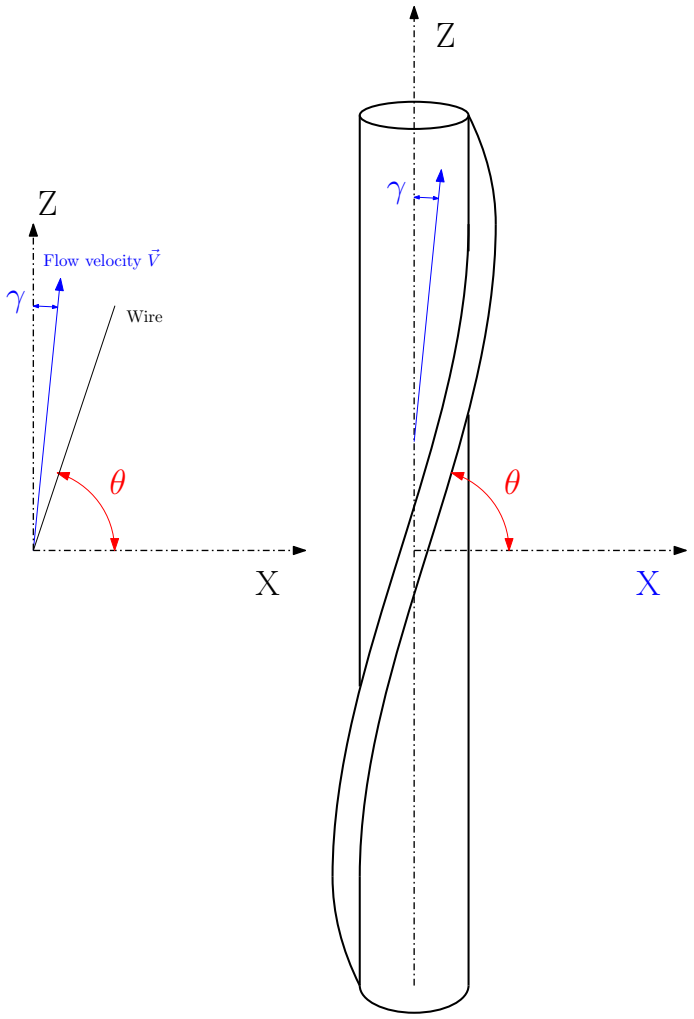

Figure 3.2.: The definition of the flow and wire angle to rod

angle between the wire and the rod axis is $\pi/4 - \theta$. The angle between the flow direction and the rod axis is defined as γ. The flow velocity vector can be decomposed into two components, one is parallel to the wire, and another one is perpendicular to the wire. The perpendicular component flow over the wire caused the wake effect. The pressure on the wire upwind side facing to the flow is higher than the pressure on the back side. The pressure difference between the two sides of the wire is considered as the driving force. The driving force induced by the wire is estimated by the drag force equation:

$$F_w = \frac{1}{2} C_D^w \rho (V \sin(90^\circ - \theta - \gamma))^2 D_w \Delta L \tag{3.3}$$

where V is the magnitude of the flow velocity, C_D^w is the drag force coefficient of wire, and D_w is the diameter of wire. ΔL is the height of an infinite small section of the rod bundle. The definition of angle γ and θ are illustrated in Fig. 3.2.

Then it is possible to get the pressure gradient of the driving force in the circumferential circuit path around the rod.

$$\nabla P_{drive} = \frac{C_D^w \rho (V \sin(90^\circ - \theta - \gamma))^2 D_w \Delta L}{2\pi D_r D_w \Delta L} = \frac{C_D^w \rho (V \sin(90^\circ - \theta - \gamma))^2}{2\pi D_r} \tag{3.4}$$

This assumption is based on a hypothesis of the geometric configuration as Fig. 3.3. One wire wrapped rod is surrounded by the bare rods. The flow circuit passage around the

wrapped rod is enclosed by the six gaps between the six nearby bare rods. The CFD simulation of the present study shows the inter-channel flow rate across the gap between bare rods is neglectable compared with the cross flow over the gaps connected to the central wire wrapped rod. The CFD result is illustrated as Fig. 3.7. So the circumferential flow around the wire wrapped rod is assumed to be enclosed in the circuit. Within the circuit, the 6 sub-channels linking to each other are simplified into an annular channel shape.

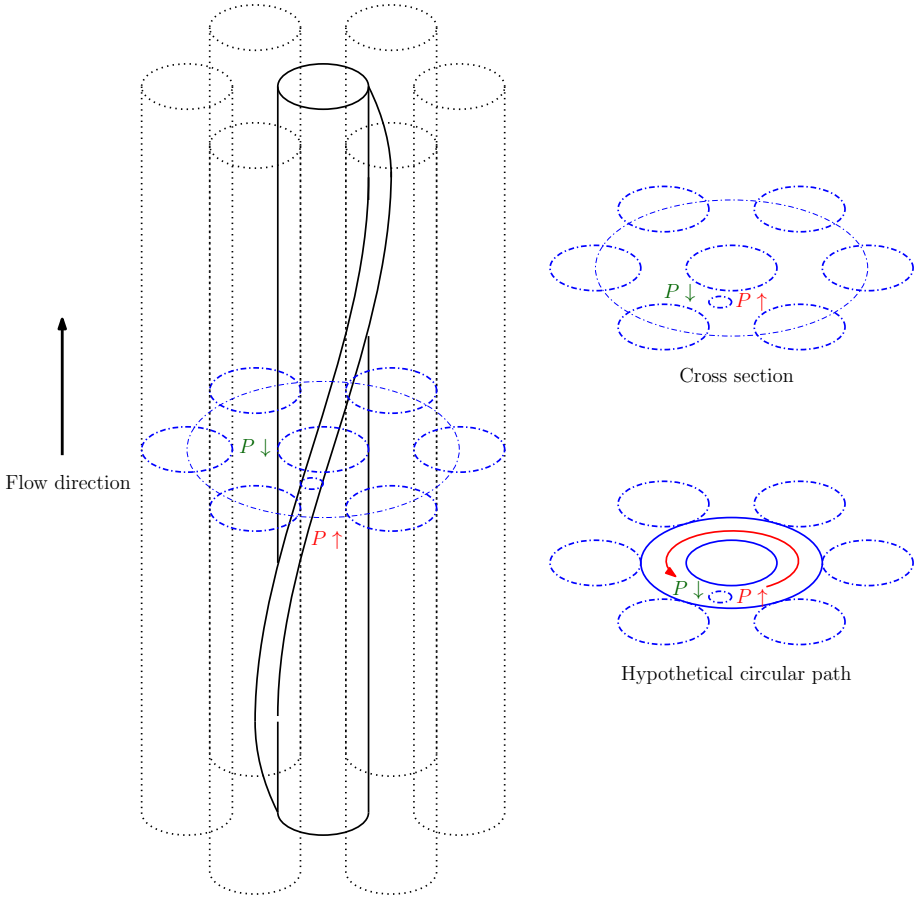

Figure 3.3.: Model of a closed circuit for swirling flow

Based on the principle of force balance, the resistance force that balances the driving force is the surface friction force. At the gap position, the surfaces of the two neighbor rods work like two parallel walls. The pressure gradient caused by the surface friction on the gap position can be estimated by the friction force equation.

$$F_f = \frac{1}{2} C_f \rho u_t^2 A \tag{3.5}$$

where A is the surface area. The friction factor C_f can be estimated with the equation from Kaviany (1985) for a laminar flow between parallel plates:

$$C_f = \frac{24}{Re} = \frac{24\nu}{V D_r} \cdot \frac{D_r}{P - D_r} = C_f' \frac{D_r}{P - D_r} \tag{3.6}$$

where Re is the Reynolds number, and ν is the kinematic viscosity. In the present study, the gap width $P - D_r$ is considered as the characteristic length. C_f' denotes the modified friction factor.

With the correlation of the friction factor, the pressure gradient caused by the surface

friction force is obtained:

$$\nabla P_{frict} = \frac{24 C'_f \rho u_t^2 \pi D_r^2 \Delta L}{2\left(P - D_r\right)^2 \pi D_r \Delta L} = \frac{12 C'_f \rho u_t^2 D_r}{\left(P - D_r\right)^2} \tag{3.7}$$

In the steady state, based on the principle of force balance, the pressure gradient induced by the friction should be equal to the pressure gradient resulted from the driving force.

$$\frac{12 C'_f D_r \rho u_t^2}{\left(P - D_r\right)^2} = \frac{C_D^w D_w \rho (V \sin(90° - \theta - \gamma))^2}{2\pi D_r D_w} \tag{3.8}$$

Solving equation 3.8, by substituting

$$u_t = V \sin(\gamma) \tag{3.9}$$

Then, we get

$$\frac{12 C'_f D_r V^2 \sin^2(\gamma)}{\left(P - D_r\right)^2} = \frac{C_D^w (V \sin(90° - \theta - \gamma))^2}{2\pi D_r} \tag{3.10}$$

The transformation of the equation is

$$\frac{12 C'_f D_r^2 \sin^2(\gamma)}{\left(P - D_r\right)^2} = \frac{C_D^w \cos^2(\theta + \gamma)}{2\pi} \tag{3.11}$$

With the square root operation on both left and right hand sides, we get

$$\sqrt{\frac{24\pi C'_f}{C_D^w}} \frac{D_r}{P - D_r} \sin\gamma = \cos(\theta + \gamma) \tag{3.12}$$

With the trigonometric formula

$$\cos(\theta + \gamma) = \cos\theta \cos\gamma - \sin\theta \sin\gamma \tag{3.13}$$

The expression of velocity direction angle γ, as a function of H/D and P/D can be obtained.

$$\cot\gamma = \frac{\sqrt{24\pi C'_f / C_D^w}}{(P/D_r - 1)\cos\theta} + \tan\theta \tag{3.14}$$

where θ can be obtained from equation

$$\tan\theta = \frac{H}{\pi(D + D_w)} \tag{3.15}$$

With the expression of γ, the normalized transverse flow velocity can be estimated with the following equation:

$$u_t^* = \frac{u_t}{u_a} = \tan\gamma = \frac{1}{\frac{\sqrt{24\pi C'_f / C_D^w}}{(P/D_r - 1)\cos\theta} + \tan\theta} \tag{3.16}$$

The normalized transverse flow velocity induced by a single wire spacer is a function of both P/D ratio and H/D ratio. Here, the angle θ is an alternative expression of the H/D ratio. This correlation is mainly used to estimate the magnitude of the sweeping flow. To validate the correlation, CFD simulations are carried out and presented in the following chapters.

3.2. The CFD model

To validate the theoretical model proposed in the present study, the open source computational fluid dynamics code OpenFOAM is used to simulate the sweeping flow in a wire wrapped 19 rod bundle.

3.2.1. Governing equations and turbulent model

In the present study, the liquid sodium is considered as an in-compressible isothermal fluid. The SIMPLE method is used to calculate the steady state of the flow field. The pressure equation, momentum equation, and two turbulent equations are solved. The convection terms in all equations were discretized by Gauss limited linear scheme and the diffusion terms were discretized by a second-order central scheme.

Continuity equation:

$$\nabla \cdot (\rho \vec{u}) = 0 \tag{3.17}$$

Momentum equation:

$$\frac{\partial \vec{u}}{\partial t} + \nabla \cdot (\vec{u}\vec{u}) = \nabla \cdot (\nu_t \nabla \vec{u}) - \nabla p \tag{3.18}$$

Based on the authors' research conclusion in the study of a 7-rod bundle Zhao et al. (2017), a robust RANS based $k - \omega$ Shear-Stress Transport (SST) turbulent model is selected for the 19-rod bundle case, which is feasible for a wide range of $y+$ values. The Spalding (1961) wall function is used to simulate the turbulence near the wall. The wall function covers laminar, transition and turbulent regions.

3.2.2. Geometric descriptions and mesh generation

To study the P/D ratio effect on the sweeping flow, a group of different geometric parameters are used for a sensitivity study. The parameters are shown as Table 3.1.

Table 3.1.: Geometric parameters for P/D ratio effect study

P/D	$D_w[mm]$	$D_r[mm]$	$P[mm]$	$H[mm]$
1.06	0.5	9.7	10.25	180
1.11	1.0	9.7	10.8	180
1.17	1.5	9.7	11.35	180
1.23	2.0	9.7	11.9	180
1.28	2.5	9.7	12.45	180
1.34	3.0	9.7	13.0	180

In the present study, a hex dominated mesh is generated by the snappyHexMesh utility. The cross section of the mesh for a 19 rod bundle ($P/D = 1.34$) is illustrated in Fig. 3.4. With snappyHexMesh, the mesh generation is divided into 3 steps:

1. A Cartesian background mesh, defined by the user, would be refined inside the geometry. The cells outside the geometry are removed, then the mesh close to the surfaces is refined to a user defined level.

2. In the snapping step, mesh points closest to the surfaces are moved exactly to the surfaces.

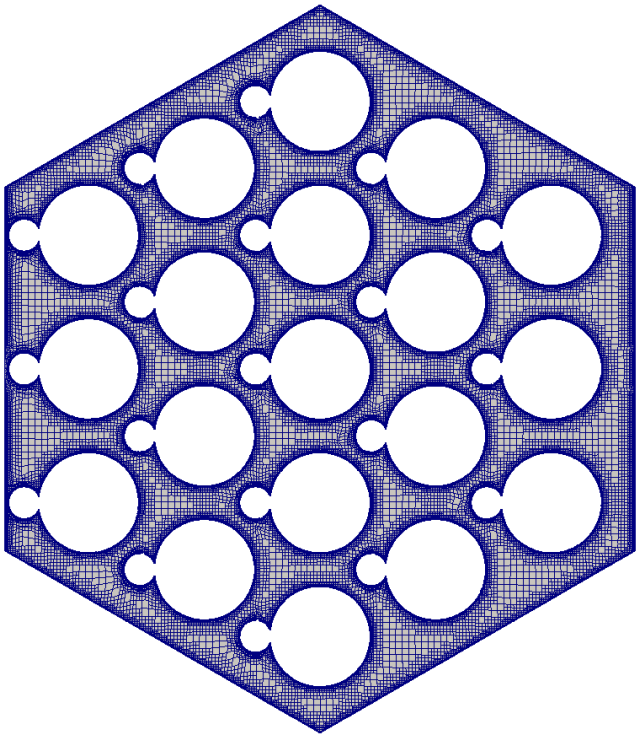

Figure 3.4.: OpenFOAM mesh for 19 rod bundle(P/D=1.34)

3. The last step is adding the wall boundary layers. In the present study, the wire regions and rod surfaces are refined, and 3 boundary layers are added on the rod surfaces.

In the CFD model, only one wire section is modeled with inlet outlet periodical boundary condition to study the developed flow. The mean flow velocity is given as the user input, a developed velocity field is passed from the outlet boundary to the inlet boundary. Then the pipe inlet effect can be removed. The hexagon can surrounding the flow region is treated as an wall boundary.

A group of meshes are generated for the cases with different P/D ratios and number of wires. A mesh sensitivity study is carried out to investigate the mesh effect on the swirling flow velocity induced by a single wire of a 19-rod bundle. In this case, only the central rod is wrapped with a wire, and the surrounding 18 rods are bare rods ($P/D = 1.11$). The normalized cross flow velocity varying along the axial position is studied with 5 different mesh resolutions. Imagine a cross plane of the rod bundle moving along the axial flow direction, the cross section of the wire rotates around the rod. When the cross section of the wire moves through the gap, the rotating direction is defined as the positive flow direction. The mesh effect on the swirling flow velocity is shown in Fig. 3.5, it can be seen that the cross flow velocity almost doesn't change with an increase of the grid number from 3.8 million up to about 8 million. For this reason and to save the computational resources, the mesh with a total grid number of about 3.8 million is selected to be used for further studies.

The aim of the CFD simulation is to study a developed flow, therefore, as mentioned before, only one wire section is modeled with periodical boundary conditions at the inlet and the outlet. The mean flow velocity is given as a user input, but the velocity distribution at inlet panel is calculated. The Reynolds number of the case with $P/D = 1.11$ is about 2.25×10^4, which is in the range of low Reynolds turbulence. The hexagonal wrapper surrounding the flow region is treated as an wall. The average $y+$ on the surface of the

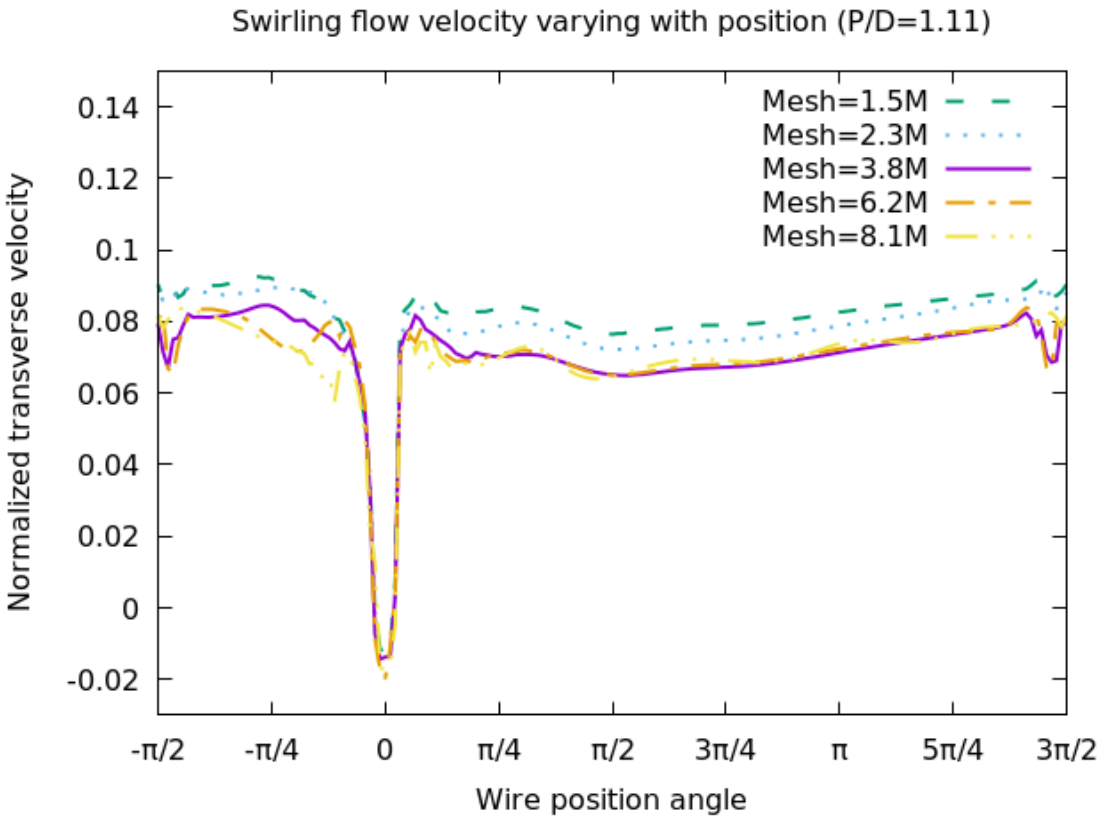

Figure 3.5.: Mesh sensitivity study on single wire induced swirling flow (P/D=1.11)

rods is 7.25, while the maximum and minimum are 47.47 and 0.29. After the calculation reaches a convergence criteria, the velocity fields on the gaps are retrieved to study the flow characteristics.

3.3. CFD results

Based on the CFD model for a wire wrapped 19-rod bundle, two sensitivity studies and one analysis are carried out:

1. P/D ratio effect on the single wire induced sweeping flow velocity.
2. comparing the rod bundle model with one single wire to the cases with 2, 4, 19 wires. The aim is investigating the effect of the wires from the neighbour rods on the flow distribution shape.
3. The flow field of fully wire wrapped 19-rod bundle

With the CFD results, the present study is going to investigate the effect of a single wire of the central rod on the swirling flow velocity magnitude and characteristics. Besides the effect of a single wire, the effect of the wires from the surrounding rods are also studied, to figure out the combination effect of multiple wires on one gap. Finally, the flow field of 19-rod bundle is analyzed.

3.3.1. One single wire induced swirling flow

The transverse flow across the gap is influenced by the rod's wire and the wires from surrounding rods. The combined effects from multiple wires are complex. So the present study starts from the analysis of the effect of a single wire. In this case, one wire wrapped

rod is surrounded by 18 bare rods as shown in Fig. 3.6. Then the sweeping flow across the gap between central channels is only affected by a single wire.

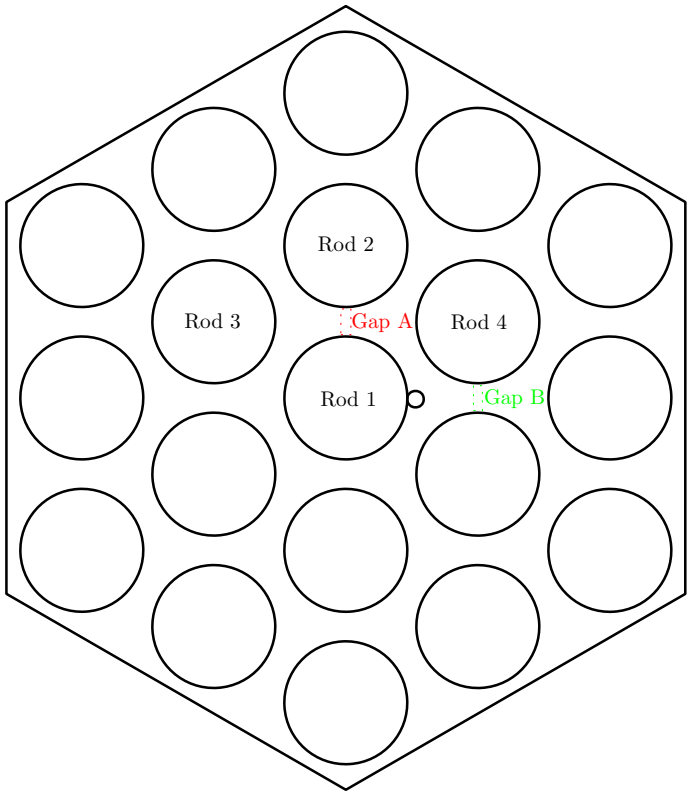

Figure 3.6.: Positions of gap A and B in the one wire rod bundle case

Based on the CFD simulation, the flow velocity at gap A which is next to the wire wrapped rod is compared with the velocity at gap B which is not directly influenced by the wire. The exact positions of the two gaps are shown in Fig. 3.6, and the comparison of the transverse velocities is shown in Fig. 3.7.

As shown in Fig. 3.7, the transverse flow velocity in gap A is much higher than in gap B. Since the flow across gap B is relatively low, it is considered as a non-dominant effect to simplify the boundary for a possible manual derivation. The manual derivation is based on the assumption of a closed circuit model in Fig. 3.3. The cross flow velocity distribution varying with the wire position angle is almost uniform, except the point where the wire crosses the gap A, the velocity changes immediately. To validate the model of Eqn. 3.16, the parameters from Table 3.1 are used for the sensitivity study. The simulation results of P/D ratio effect are shown in Fig. 3.8. The normalized average velocity is defined as the ratio of area weighted cross flow velocity over a length of one wire pitch to the mean axial flow velocity. This normalized sweeping flow velocity is used to estimate the magnitude of the normalized sweeping velocity with multiple wire spacers.

As shown in Fig. 3.8, the proposed theoretical model agrees well with the CFD results. The result shows a big effect of the P/D ratio on the magnitude of the transverse flow velocity induced by a single wire. In previous studies, the sweeping flow is assumed independent of the P/D ratio. While, the present study proves the P/D ratio effect can not be ignored, and the theoretical correlation proposed by the present study is a function of both P/D ratio and H/D ratio. Here, the H/D ratio of different CFD models are consistent, but the variant P/D ratios are studied. The new correlation can give a more accurate prediction of the magnitude of the sweeping flow.

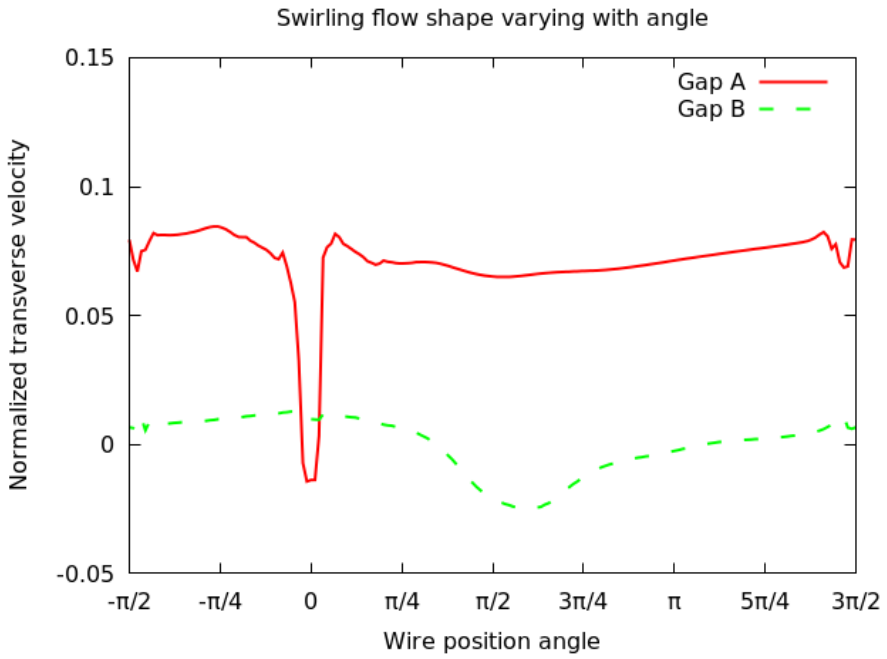

Figure 3.7.: The swirling flow shape in the single wire rod bundle(P/D=1.11)

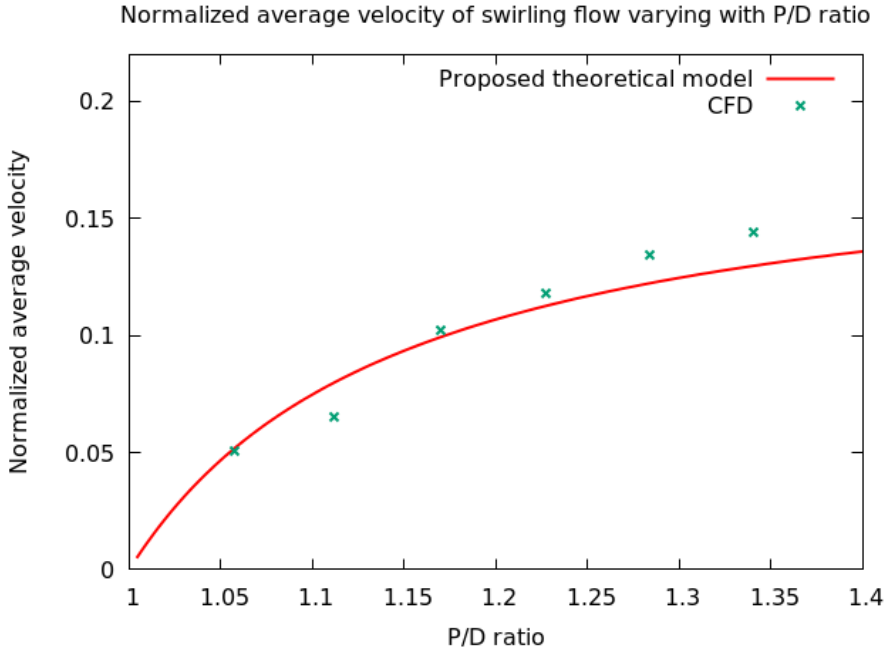

Figure 3.8.: The effect of P/D ratio on the transverse velocity induced by a single wire

The empirical correlation gives a good explanation on the relationship between normalized transverse velocity induced by a single wire, and the P/D, H/D ratio. The angle θ is a function of H/D ratio. The bigger the P/D ratio, the higher the transverse velocity. The bigger the H/D ratio, the lower the transverse velocity. In the extreme hypothetical condition, the wire spacer is parallel to the rod which means the H/D ratio is infinite, then we get a result of 0 m/s with Eqn. 3.16. In the opposite extreme hypothetical condition, the wire spacer is perpendicular to the rod, the normalized sweeping flow velocity tends to be infinite, by the indication of the theoretical model. The proposed model gives a good

physical explanation of the two extreme hypothetical conditions.

The single wire case is an ideal case, but in the real fuel assembly each rod is wrapped with a wire spacer.

3.3.2. Multiple wires effect on the transverse flow

In the fuel assembly, the sweeping flow must be affected by multiple wires of the rods surrounding the gap. To figure out the influence from the wires, a sensitivity study of the effect of number of wires on the transverse flow is carried out. The result is shown in Fig. 3.9.

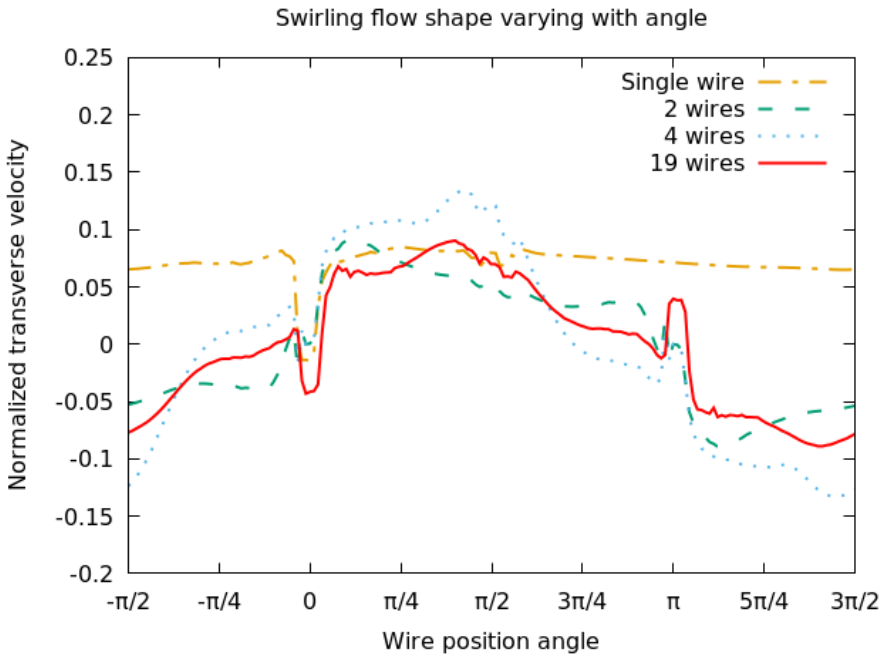

Figure 3.9.: The effect of wire numbers on the transverse flow shape

In present study, it is assumed that the transverse flow on gap A is mainly affected by the wires of its surrounding rods. The surrounding rods are marked as Rod 1-4 in Fig. 3.6. The wires of Rod 1 and Rod 2 enters into the Gap A alternatively. While the wires of Rod 3 and Rod 4 move into the two sub-channels on the both side of the Gap A. So, 4 simulation cases with a wires number of 1, 2, 4, 19 are compared. Fig. 3.9 shows that the transverse flow gives almost a uniform distribution with the effect of a single wire. If both rods (Rod 1 and Rod 2 as shown in Fig. 3.6) next to the gap A are wire wrapped, and the rest are bare rods, then the shape is completely different from the single wire case. Since the cross sections of the two wires rotate around the two rods in the flow direction, they cross the gap between the two rods alternately in opposite directions. It can be seen, that the cross flow direction changes with the two wires entering the gap periodically. The curve of “19 wires” shows the velocity distribution shape of a full wire wrapped 19-rod bundle, in which case each rod is wrapped with a wire. The effect from the four wires of the closest four rods (Rod 1-4 as shown in Fig. 3.6) around the gap is very close to the case with 19 wires. So, the transverse flow distribution shape is mainly dominated by the four wires surrounding the gap. Most importantly, the amplitude of the transverse flow is not effected by the number of wires. The magnitude of the transverse flow can be estimated with the proposed empirical model for the single wire case. With multiple wires, the flow direction changes periodically with the effects of the helical wires.

3.3.3. Flow field of the wire wrapped 19-rod bundle

In the 19 wire wrapped rod bundle, the wires rotate in the anti clock-wise direction along the flow direction. The whole flow field of the coolant channel is affected by both, the wires and the wall of the fuel assembly box. The CFD simulation result of the case with $P/D = 1.11$ is selected for analysis. The results of other cases are quite similar. From the top to down view of the cross section of the rod bundle, the wire spacer rotates in the anti-clock wise direction along the flow direction. Tow cross sections with a phase different of π are retried for explanation. At the axial angular positions of $2\pi/3$ and $4\pi/3$, the pressure fields are illustrated in Fig. 3.10 (a) and (b). The unit of pressure is Pa.

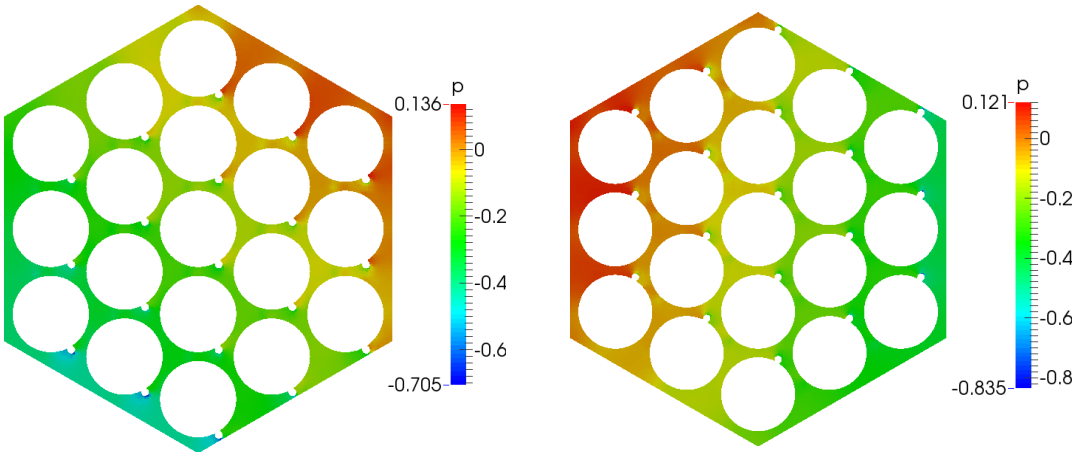

(a) $\varphi = 2\pi/3$ (b) $\varphi = 4\pi/3$

Figure 3.10.: Pressure field of flow cross section at different axial positions

As shown in the pressure field, the higher pressure zone also rotates in anti-clock wise direction. Since the gravity force is considered to have no influence to the wire induced sweeping flow, the gravity term is not included in the momentum equation. The pressure given in the figures is relative pressure, both the hydrostatic pressure and atmospheric pressure are not included. A small interesting detail can be found in the pressure field, it is that the pressure at the upwind side of the wire is relatively higher than the back side. This proves the assumption of the wire induced wake effect, which is used in the derivation of the new sweeping flow correlation.

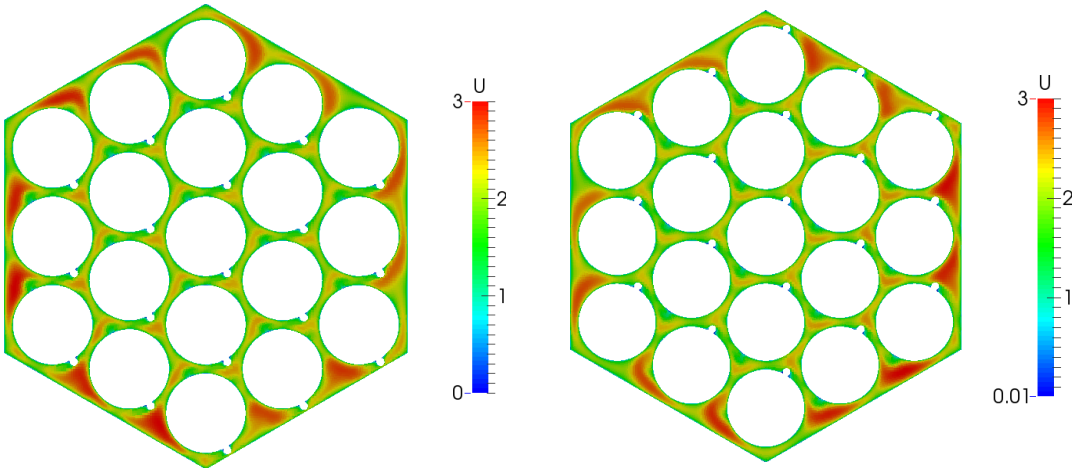

(a) $\varphi = 2\pi/3$ (b) $\varphi = 4\pi/3$

Figure 3.11.: Velocity field of flow cross section at different axial positions

Fig. 3.11 shows the velocity field of the flow channel's cross section. The unit of the velocity is m/s. The influence of the wire position on the velocity magnitude is small. The flow velocity magnitude in the wall channels is higher than in the internal channels. It is because of the hydraulic diameter of a wall channel is larger than the hydraulic diameter of an internal channel, and the wall channel only faces to one wire wrapped rod. The velocity magnitude includes the velocity component in axial direction. The higher velocity can be observed at the inter-channel zone, this is the transverse sweeping flow.

By analyzing both the pressure field and the velocity, it gives a further confirmation of the theory proposed in present study. For a quantitative evaluation, the CFD calculated normalized sweeping flow velocity curve is compared with the result estimated by the new proposed model.

3.4. Assessment of the new model

In the models proposed by the previous studies of Wantland (1974), Ginsberg (1972) and Raj and Velusamy (2016), the sweeping flow distribution shape in the axial direction is represented as a cosine function. This is caused by the wire spacers from the two neighbouring rods enter into the gap between the two rods alternatively. This results a periodical change of transverse flow direction across the gap. For the fully wire wrapped rod bundle, the present study keeps the cosine like function for the velocity distribution shape, and use the proposed Eqn. 3.16 to estimate the amplitude of the sweeping flow. By combining the cosine function with Eqn. 3.16, we get a new correlation:

$$u_t^*(\varphi) = \frac{\cos(\varphi - \frac{\pi}{3})}{\frac{\sqrt{24\pi C_f'/C_D^w}}{(P/D_r - 1)\cos\theta} + \tan\theta} \tag{3.19}$$

where, the angular position φ can be considered as the wire off gap angle. If the wire is exactly at the gap position, $\varphi = 0$. The CFD result shows the maximum velocity point is 60 degrees from the gap, so a constant of $\pi/3$ is used. The drag coefficient C_D^w is 1.17 for wire spacer. C_f' is estimated with Eqn. 3.6.

In Fig. 3.12, the proposed correlation is compared with the CFD results for the 19-rod bundle cases with different P/D ratios of 1.11, 1.23, and 1.34. The proposed correlation agrees well with the simulation results. Since, the Wantland model assumes the flow goes along with the wire, the maximum velocity occurs on the position where the wire enters the gap. In Fig. 3.12, it can be seen that, Wantland's correlation fails to predict the accurate maximum velocity position based on purely geometric considerations. Another main difference between the new model and Wantland model is that, the P/D ratio effect is included in the new correlation. So, the new correlation is able to get a good prediction on the amplitude of the distribution's shape.

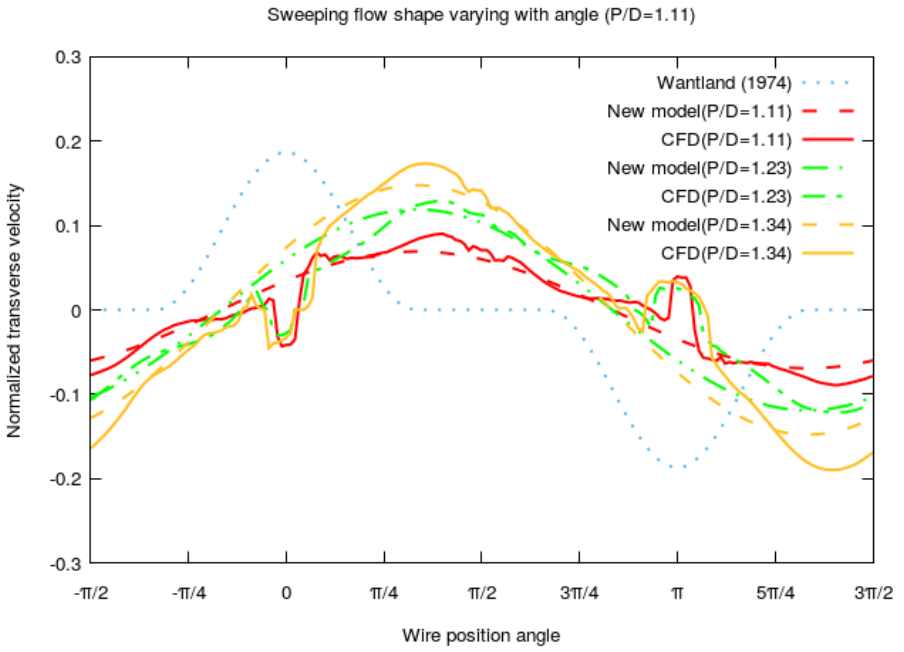

Figure 3.12.: Normalized transverse flow distribution shape in axial direction

4. Local heat transfer

In practical engineering applications, the circumferential heat transfer of a fuel rod is usually assumed to be a uniform distribution. For example, the cladding temperature in MATRA code is assumed to uniform, since the sub-channel control volume is the base element, and the detailed internal temperature field is not resolved. In the sodium cooled fast reactor, the fuel rods are arranged in triangular shape, the local heat transfer is influenced by the shape of the cross section of the coolant region. The heat transfer of the surface wall area of a fuel rod facing to the center of a sub-channel is different from the wall surface area at the rod to rod gap position. The wire spacer also affects the local heat transfer of the fuel rod. The local heat transfer is mainly dominated by the fuel rod arrangement pattern and the flow field. The flow field is divided into axial flow and sweeping flow. For the sweeping flow, we already get some research results in the previous chapter. Describing the detailed local heat transfer distribution has a practical engineering interest. In this chapter, both theoretical and CFD studies are carried out to investigate the local heat transfer in the typical SFR fuel assembly.

4.1. Theoretical model

4.1.1. Governing equations

To derive the local heat transfer model for the wire wrapped fuel rods, the wires are assumed to occupy zero space in the fluid zone. Then, it is possible to solve the heat conduction equations in a two dimensional panel. But the sweeping flow in the 2D cross section of the flow zone should be considered. In a hypothetical fuel rod bundle with an infinite number of triangular arrayed fuel rods, the symmetrical boundaries can be applied to the fuel rod and coolant linking one rod center to its surrounding rod centers, and also to the middle point of the line connection between two neighboring rods. In the fuel assembly of triangular arrayed rods, one basic fuel-coolant element with an angle of 30 degrees is studied in the polar coordinate. The original point is the center of one fuel rod, and the other two vertexes of the triangular shape are the center point of one sub-channel and the middle point between two rods. The three edges of the triangular are symmetrical boundaries.

As shown in Fig. 4.1 the radius of the fuel is R_f, the inner radius of cladding is R_{ci}, and the outer radius of cladding is R_{co}. $\frac{P}{D}$ is the pitch to diameter ratio of rods. $\frac{P}{D}R_{co}$ is equal to $\frac{1}{2}P$, the distance from the rod center point to the middle point of the gap. For the

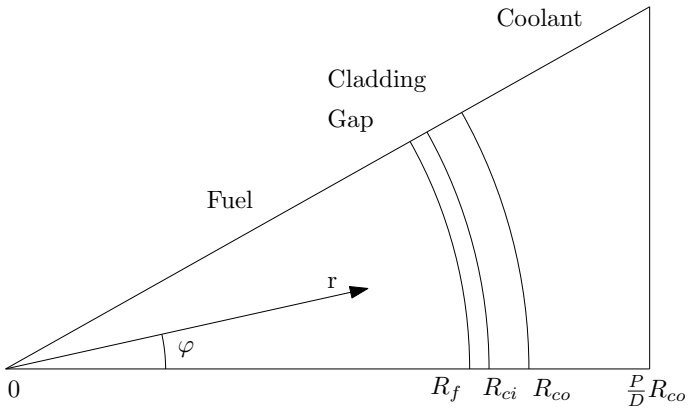

Figure 4.1.: The cross section of finite fuel and coolant element.

heat balance in steady state, the governing equations are given as following for different regions.

The heat conduction equation for the fuel zone:

$$\lambda_f \frac{\partial^2 T_f}{\partial r^2} + \frac{\lambda_f}{r}\frac{\partial T_f}{\partial r} + \frac{\lambda_f}{r^2}\frac{\partial^2 T_f}{\partial \varphi^2} + Q_v = 0 \tag{4.1}$$

where T_f is the fuel temperature, and λ_f is the thermal conductivity of fuel. r is the radial position, and φ is the circumferential angle. Q_v refers to the volume heat source.

The heat conduction equation for the gas gap:

$$\lambda_g \frac{\partial^2 T_g}{\partial r^2} + \frac{\lambda_g}{r}\frac{\partial T_g}{\partial r} + \frac{\lambda_g}{r^2}\frac{\partial^2 T_g}{\partial \varphi^2} = 0 \tag{4.2}$$

where λ_g is the effective heat conductivity of gas gap between the fuel and the cladding. The subscript g indicates the gas gap.

The heat conduction equation for the cladding:

$$\lambda_c \frac{\partial^2 T_c}{\partial r^2} + \frac{\lambda_c}{r}\frac{\partial_c}{\partial r} + \frac{\lambda_c}{r^2}\frac{\partial^2 T_c}{\partial \varphi^2} = 0 \tag{4.3}$$

where the subscript c indicates the cladding material.

For the liquid sodium coolant zone, the flow velocity in the radial direction is neglected, since it is perpendicular to the wall surface. But both the axial flow and the circumferential sweeping flow are considered in the equation.

The heat conduction equation for the liquid sodium coolant:

$$\rho c_p \left(\frac{1}{r}u_\varphi \frac{\partial T_l}{\partial \varphi} + u_z \frac{\partial T_l}{\partial z}\right) = \lambda_l \frac{\partial^2 T_l}{\partial r^2} + \frac{\lambda_l}{r}\frac{\partial T_l}{\partial r} + \frac{\lambda_l}{r^2}\frac{\partial^2 T_l}{\partial \varphi^2} \tag{4.4}$$

where c_p is the thermal capacity of liquid coolant, and ρ is the density. u_φ is the circumferential velocity which is varying with the angle. The circumferential velocity can be estimated from the propsed sweeping flow correlation for the gap. The coordinate z is the axial position, and u_z is the local axial velocity.

While, based on the principle of energy balance, the heat removed by the coolant equals to the heat transferred from the cladding surface. The coolant temperature gradient in the axial direction can be represented as the following equation:

$$\rho c_p \frac{\partial T}{\partial z} u_a = \frac{4 q_{av}}{D_e} \tag{4.5}$$

where u_a is the bulk velocity of the coolant in the axial direction. q_{av} is the average wall heat flux on the cladding surface, the unit is W/m^2. D_e is the heated hydraulic diameter of the coolant zone.

Then the energy equation for the coolant is reformed.

$$\lambda_l \frac{\partial^2 T_l}{\partial r^2} + \frac{\lambda_l}{r}\frac{\partial T_l}{\partial r} + \frac{\lambda_l}{r^2}\frac{\partial^2 T_l}{\partial \varphi^2} = \rho c_p \frac{1}{r} u_\varphi \frac{\partial T_l}{\partial \varphi} + \frac{4u_z}{D_e u_a} q_{av} \tag{4.6}$$

where u_φ is calculated by the new proposed Eqn. 3.19 in previous chapter. For the triangular arrayed rod bundle, the heated hydraulic diameter is

$$D_e = \frac{2\sqrt{3}p^2 - \pi D^2}{\pi D} \tag{4.7}$$

All the equations are rewritten into the dimensionless form. The definition of dimensionless temperature is

$$\theta = \frac{T - T_b}{T_{co,av} - T_b} \tag{4.8}$$

where T_b is the bulk coolant temperature, and $T_{co,av}$ is the average cladding outer surface temperature.

The dimensionless form of temperature is used for fuel, gap, cladding, and coolant. The definition of the bulk temperature is

$$T_b = \frac{\int_0^{\frac{\pi}{6}} \int_{R_{c0}}^{\frac{PR_{c0}}{D\cos\varphi}} T_l u_z r \mathrm{d}r \mathrm{d}\varphi}{\int_0^{\frac{\pi}{6}} \int_{R_{c0}}^{\frac{PR_{c0}}{D\cos\varphi}} u_z r \mathrm{d}r \mathrm{d}\varphi} \tag{4.9}$$

So the dimensionless form of the governing equations for the 4 regions are

$$\frac{\partial^2 \theta_f}{\partial(\frac{r}{R_f})^2} + \frac{1}{(\frac{r}{R_f})}\frac{\partial \theta_f}{\partial(\frac{r}{R_f})} + \frac{1}{(\frac{r}{R_f})^2}\frac{\partial^2 \theta_f}{\partial \varphi^2} + 2\frac{\lambda_l}{\lambda_f} Nu = 0 \tag{4.10}$$

$$\frac{\partial^2 \theta_g}{\partial(\frac{r}{R_{ci}})^2} + \frac{1}{(\frac{r}{R_{ci}})}\frac{\partial \theta_g}{\partial(\frac{r}{R_{ci}})} + \frac{1}{(\frac{r}{R_{ci}})^2}\frac{\partial^2 \theta_g}{\partial \varphi^2} = 0 \tag{4.11}$$

$$\frac{\partial^2 \theta_c}{\partial(\frac{r}{R_{co}})^2} + \frac{1}{(\frac{r}{R_{co}})}\frac{\partial \theta_c}{\partial(\frac{r}{R_{co}})} + \frac{1}{(\frac{r}{R_{co}})^2}\frac{\partial^2 \theta_c}{\partial \varphi^2} = 0 \tag{4.12}$$

$$\frac{\partial^2 \theta_l}{\partial(\frac{r}{R_{co}})^2} + \frac{1}{(\frac{r}{R_{co}})}\frac{\partial \theta_l}{\partial(\frac{r}{R_{co}})} + \frac{1}{(\frac{r}{R_{co}})^2}\frac{\partial^2 \theta_l}{\partial \varphi^2} = \frac{1}{\alpha}\frac{R_{co}u_\varphi}{(\frac{r}{R_{co}})}\frac{\partial \theta_l}{\partial \varphi} + \frac{4R_{co}u_z}{D_e u_a} Nu \tag{4.13}$$

To solve the governing equation group, the boundary conditions are required.

4.1.2. Boundary conditions

Assuming the temperature field is symmetrical, then the boundary condition at the borders of the finite triangular element is symmetry. The temperature gradient at the symmetrical boundary must be 0.

If $\varphi = 0$, $0 \le \frac{r}{R} \le 1$, or $1 \le \frac{r}{R} \le \frac{P}{D\cos\varphi}$, then

$$\frac{\partial \theta}{\partial \varphi} = 0 \tag{4.14}$$

If $\varphi = \frac{\pi}{6}$, $0 \leq \frac{r}{R} \leq 1$, or $1 \leq \frac{r}{R} \leq \frac{P}{D\cos\varphi}$, then

$$\frac{\partial\theta}{\partial\varphi} = 0 \tag{4.15}$$

Based on the definition of the dimensionless temperature, the integration of the dimensionless temperature over the cladding outer surface equals to a constant.

If $\frac{r}{R_{co}} = 1$, then

$$\frac{6}{\pi}\int_0^{\frac{\pi}{6}} \theta_c d\varphi = 1 \tag{4.16}$$

For the fuel zone, the central temperature is not infinite. The fuel center temperature must be a finite value.

The temperature and heat flux of two contacting regions should be consistent at their interface. The temperatures of the two regions are equal to each other at the same position. The heat fluxes are also the same at the interface location.

If $\frac{r}{R_f} = 0$, then

$$\theta = limited \tag{4.17}$$

If $\frac{r}{R_f} = 1$, $0 \leq \varphi \leq \frac{\pi}{6}$, then

$$\theta_f = \theta_g \tag{4.18}$$

$$\lambda_f \frac{1}{R_f}\frac{\partial\theta_f}{\partial(\frac{r}{R_f})} = \lambda_g \frac{1}{R_{ci}}\frac{\partial\theta_g}{\partial(\frac{r}{R_{ci}})} \tag{4.19}$$

If $\frac{r}{R_{ci}} = 1$, $0 \leq \varphi \leq \frac{\pi}{6}$, then

$$\theta_g = \theta_c \tag{4.20}$$

$$\lambda_g \frac{1}{R_{ci}}\frac{\partial\theta_g}{\partial(\frac{r}{R_{ci}})} = \lambda_c \frac{1}{R_{co}}\frac{\partial\theta_c}{\partial(\frac{r}{R_{co}})} \tag{4.21}$$

If $\frac{r}{R_{co}} = 1$, $0 \leq \varphi \leq \frac{\pi}{6}$, then

$$\theta_c = \theta_l \tag{4.22}$$

$$\lambda_c \frac{\partial\theta_c}{\partial(\frac{r}{R_{co}})} = \lambda_l \frac{\partial\theta_l}{\partial(\frac{r}{R_{co}})} \tag{4.23}$$

For the liquid sodium fluid zone, it is also assumed that the temperature field is symmetrical at the boundaries.

If $\frac{r}{R_{co}} = \frac{P}{D\cos\varphi}$, $0 \leq \varphi \leq \frac{\pi}{6}$, then

$$\frac{\partial\theta_l}{\partial(\frac{r}{R_{co}})} = \frac{\sin\varphi}{P/D}\frac{\partial\theta_l}{\partial\varphi} \tag{4.24}$$

With the boundary conditions, the second order differential equations of temperatures can be solved. Besides the boundary conditions, the velocity distribution should be given with some assumptions. The sweeping flow velocity at the gap interface can be obtained from Eqn. 3.19. The axial velocity distribution is assumed dependent on the wall distance.

4.1.3. Distribution of axial velocity

In the coolant zone, the axial velocity distributes as a function of the radial distance to the wall. The sweeping velocity is a function of the wire to gap angle and the circumferential angle. The velocity distribution in the radial direction can be obtained by the law of the wall assumption [Munson et al. (2013)]. The dimensionless axial velocity and wall distance are

$$u^+ = \frac{u_z}{(\frac{\tau_w}{\rho})^{\frac{1}{2}}} \tag{4.25}$$

where τ_w is the wall shear stress.

$$r^+ = \frac{(r - R_{co})(\frac{\tau_w}{\rho})^{\frac{1}{2}}}{\nu} \tag{4.26}$$

For a wide range of channel flow, it is possible to use a power law expression to give a good approximation of the radial velocity distribution.

$$u^+ = c(r^+)^m \tag{4.27}$$

where the constant coefficients c and m depend on the Re number.

The wall shear stress can be obtained by

$$\tau_w = \frac{D_e}{4}(\frac{\Delta P}{L}) \tag{4.28}$$

where D_e is the hydraulic diameter. ΔP is the pressure drop over the axial length of L.

The pressure drop is calculated from the equation:

$$\Delta P = C_f \frac{L}{D_e} \frac{\rho u_a^2}{2} \tag{4.29}$$

where C_f is the friction factor. It depends on the type of sub-channel. Some correlations were proposed to calculate the friction factor of the wire wrapped rod bundles [Novendstern (1972), Rehme (1973), Cheng and Todreas (1986)].

The simplified Cheng and Todreas (1986) correlation gives the correlations of friction factor for laminar, transition and turbulent regions. The correlations are illustrated as below.

For the laminar region:

$$C_f = \frac{C_{fL}}{Re} \tag{4.30}$$

For the transition region:

$$C_f = (\frac{C_{fT}}{Re^{0.18}})\psi^{\frac{1}{3}} + (\frac{C_{fT}}{Re})\psi^{\frac{1}{3}} \tag{4.31}$$

For the turbulent region:

$$C_f = \frac{C_{fT}}{Re^{0.18}} \tag{4.32}$$

The intermittent factor is

$$\psi = \frac{\log(Re/Re_L)}{\log(Re_T/Re_L)} \tag{4.33}$$

$$C_{fL} = [-974.6 + 1612.0(\frac{P}{D}) - 598.5(\frac{P}{D})^2](\frac{H}{D})^{0.06-0.085(P/D)} \tag{4.34}$$

$$C_{fT} = [0.8063 - 0.9022\log(\frac{H}{D}) + 0.3526(\log(\frac{H}{D}))^2](\frac{P}{D})^{9.7}(\frac{H}{D})^{1.78-2(P/D)} \tag{4.35}$$

By substituting the pressure drop Eqn. 4.29 into the wall shear stress Eqn. 4.28, the wall shear stress correlation is reformed to

$$\tau_w = \frac{C_f}{8}\rho u_a^2 \tag{4.36}$$

Substituting the above equation into the power law expression, we can get

$$u_z = c\frac{(r - R_{co})^m(\frac{C_f}{8})^{\frac{1}{2}(m+1)}u_a^{m+1}}{\nu^m} \tag{4.37}$$

$$\frac{u_z}{u_a} = c\frac{(r - R_{co})^m(\frac{C_f}{8})^{\frac{1}{2}(m+1)}u_a^{m}}{\nu^m} \tag{4.38}$$

The last term of Eqn. 4.13 can be rewritten as

$$\frac{4R_{co}(r - R_{co})^m(\frac{C_f}{8})^{\frac{1}{2}(m+1)}u_a^{m}}{D_e\nu^m}Nu \tag{4.39}$$

Finally, Eqn. 4.13 is reformed into

$$\frac{\partial^2\theta_l}{\partial(\frac{r}{R_{co}})^2} + \frac{1}{(\frac{r}{R_{co}})}\frac{\partial\theta_l}{\partial(\frac{r}{R_{co}})} + \frac{1}{(\frac{r}{R_{co}})^2}\frac{\partial^2\theta_l}{\partial\varphi^2} = \frac{1}{\alpha}\frac{R_{co}}{(\frac{r}{R_{co}})}u_\varphi\frac{\partial\theta_l}{\partial\varphi} + \frac{4R_{co}(r - R_{co})^m(\frac{C_f}{8})^{\frac{1}{2}(m+1)}u_a^{m}}{D_e\nu^m}Nu \tag{4.40}$$

This transformed governing equation for the liquid sodium region is used in the further derivation.

4.1.4. Equation solving

Refereed to the research work of Nijsing and Eifler (1969), a similar differential equation solving procedure is carried out. By combining the homogeneous and non-homogeneous parts of Eqn. 4.10, a general solution of the second order differential equation for the fuel temperature field is

$$\theta_f = A + B\ln(\frac{r}{R_f}) + \sum_{i=1}^{\infty}\left[C_i(\frac{r}{R_f})^i + D_i(\frac{r}{R_f})^{-i}\right][E_i\cos(i\varphi) + F_i\sin(i\varphi)] \tag{4.41}$$

where A, B, C_i, D_i, E_i and F_i are the constant coefficients to be solved. With the boundary condition Eqn. 4.17 at position $r/R_f = 0$, we can get $B = 0$, and $D_i = 0$. With the symmetrical boundary conditions Eqn. 4.14 and Eqn. 4.15 when $\varphi = 0$ or $\varphi = \pi/6$, it is obtained that $F_i = 0$, and $i = 6k$, where $k = 1, 2, 3....$

Combining the above boundary conditions with Eqn. 4.10, we get

$$\theta_f = A_f - \frac{\lambda_l}{2\lambda_f}Nu_l(\frac{r}{R_f})^2 + \sum_{i=1}^{\infty}\left[C_{fi}(\frac{r}{R_f})^{6i}\cos(6i\varphi)\right] \tag{4.42}$$

By solving the homogeneous linear differential equation, the solution for the gas gap and cladding can be obtained.

$$\theta_g = A_g + B_g\ln\frac{r}{R_{ci}} + \sum_{i=1}^{\infty}\left[C_{gi}(\frac{r}{R_{ci}})^{6i} + D_{gi}(\frac{r}{R_{ci}})^{-6i}\right]\cos(6i\varphi) \tag{4.43}$$

$$\theta_c = A_c + B_c \ln \frac{r}{R_{co}} + \sum_{i=1}^{\infty} \left[C_{ci} (\frac{r}{R_{co}})^{6i} + D_{ci} (\frac{r}{R_{co}})^{-6i} \right] \cos(6i\varphi) \tag{4.44}$$

For the liquid sodium coolant zone, Eqn. 4.40 is a non-homogeneous second order differential equation. Firstly, we start from solving the homogeneous part.

$$\theta(\gamma, \varphi) = R(\gamma)\Phi(\varphi) \tag{4.45}$$

where $\gamma = \frac{r}{R_{co}}$. $R(\gamma)$ represents a function of γ, and $\Phi(\varphi)$ represents a function of φ.

Then we can get the characteristic equation.

$$R''(\gamma)\Phi(\varphi) + \frac{1}{\gamma} R'(\gamma)\Phi(\varphi) + \frac{1}{\gamma^2} R(\gamma)\Phi''(\varphi) - \frac{R_{co} u_\varphi}{\alpha\gamma} R(\gamma)\Phi'(\varphi) = 0 \tag{4.46}$$

Rearranging the equation to

$$\frac{\gamma^2 R''(\gamma) + \gamma R'(\gamma)}{R(\gamma)} = -\frac{\Phi''(\varphi) - \frac{R_{co} u_\varphi \gamma}{\alpha} \Phi'(\varphi)}{\Phi(\varphi)} = \lambda_m \tag{4.47}$$

where λ_m is the character value.

Then we get a second order Cauchy-Euler equation [Kreyszig (2006)]:

$$\gamma^2 R''(\gamma) + \gamma R'(\gamma) - \lambda_m R(\gamma) = 0 \tag{4.48}$$

Assuming the tail solution

$$t = \ln(\gamma) \tag{4.49}$$

$$R(\gamma) = \Psi(\ln(\gamma)) = \Psi(t) \tag{4.50}$$

Differentiating

$$\frac{dR(\gamma)}{d\gamma} = \frac{1}{\gamma} \frac{d\Psi(t)}{dt} \tag{4.51}$$

$$\frac{d^2 R(\gamma)}{d\gamma^2} = \frac{1}{\gamma^2} \left(\frac{d^2\Psi(t)}{dt^2} - \frac{d\Psi(t)}{dt} \right) \tag{4.52}$$

Substituting into the equation, then the rearranging gives

$$\frac{d^2\Psi(t)}{dt^2} - \lambda_m \Psi(t) = 0 \tag{4.53}$$

The characteristic equation

$$\kappa^2 = \lambda_m \tag{4.54}$$

If λ_m is a positive value, then

$$R(\gamma) = c_1 \gamma^{\sqrt{\lambda_m}} + c_2 \gamma^{-\sqrt{\lambda_m}} \tag{4.55}$$

If $\lambda_m = 0$, then

$$R(\gamma) = c_3 + c_4 \ln(\gamma) \tag{4.56}$$

In the similar way, we can get

$$\Phi''(\varphi) - \frac{R_{co}u_{\varphi}\gamma}{\alpha}\Phi'(\varphi) - \lambda_m\Phi(\varphi) = 0 \tag{4.57}$$

The characteristic equation is

$$\kappa^2 - \frac{R_{co}u_{\varphi}\gamma}{\alpha}\kappa - \lambda_m = 0 \tag{4.58}$$

If $\lambda = 0$, then

$$\kappa = \frac{R_{co}u_{\varphi}\gamma}{\alpha} \tag{4.59}$$

or

$$\kappa = 0 \tag{4.60}$$

Then one of the solutions is

$$\Phi(\varphi) = e^{\frac{R_{co}u_{\varphi}\gamma}{\alpha}\varphi} \tag{4.61}$$

So, one of the solutions for the homogeneous part is

$$\theta = [c_3 + c_4\ln(\gamma)]\, e^{\frac{R_{co}u_{\varphi}\gamma}{\alpha}\varphi} \tag{4.62}$$

For the non-homogeneous part, one of the solutions is

$$\theta = \frac{4R_{co}(\frac{C_f}{8})^{\frac{1}{2}(m+1)}u_a^m Nu}{D_e\nu^m Re_{co}^m}\left[\frac{(\gamma-1)^{m+2}}{(m+2)^2} + \frac{(\gamma-1)^{m+1}}{(m+1)^2(m+2)} - \frac{1}{(m+1)(m+2)}\int_1^{\gamma}\frac{(\gamma-1)^m}{\gamma}d(\gamma)\right] \tag{4.63}$$

Then, the complete solution for the liquid sodium fluid zone is

$$\begin{aligned}\theta_l = {} & A_l + B_l\ln(\gamma)e^{\frac{R_{co}u_{\varphi}\gamma}{\alpha}\varphi} + C_l e^{\frac{R_{co}u_{\varphi}\gamma}{\alpha}\varphi} \\ & + \frac{4R_{co}(\frac{C_f}{8})^{\frac{1}{2}(m+1)}u_a^m Nu}{D_e\nu^m Re_{co}^m}\left[\frac{(\gamma-1)^{m+2}}{(m+2)^2} + \frac{(\gamma-1)^{m+1}}{(m+1)^2(m+2)} - \frac{1}{(m+1)(m+2)}\int_1^{\gamma}\frac{(\gamma-1)^m}{\gamma}d(\gamma)\right] \\ & + Nu\sum_{i=1}^{\infty}\left[C_{li}(\frac{r}{R_{co}})^{6i} + D_{li}(\frac{r}{R_{co}})^{-6i}\right]\cos(6i\varphi)\end{aligned} \tag{4.64}$$

Determined by the boundary condition equation 4.16.

$$A_c = 1 \tag{4.65}$$

From equations 4.64, 4.65 and 4.44, we can get

$$A_l = 1 \tag{4.66}$$

$$C_l = 0 \tag{4.67}$$

Determined by the boundary condition equations 4.16-4.23

$$A_f - \frac{\lambda_l}{2\lambda_f}Nu = A_g \tag{4.68}$$

$$-\lambda_l Nu = \lambda_g B_g \tag{4.69}$$

$$A_g = 1 + B_c \ln \frac{R_{ci}}{R_{co}} \tag{4.70}$$

$$\lambda_g B_g = \lambda_c B_c \tag{4.71}$$

$$\lambda_c B_c = \lambda_l B_l \tag{4.72}$$

and the coefficients

$$C_{fi} = C_{gi}(\frac{R_f}{R_{ci}})^{6i} + D_{gi}(\frac{R_f}{R_{ci}})^{-6i} \tag{4.73}$$

$$\frac{\lambda_f}{\lambda_g} 6iC_{fi} = 6iC_{gi}(\frac{R_f}{R_{ci}})^{6i-1} - 6iD_{gi}(\frac{R_f}{R_{ci}})^{-6i-1} \tag{4.74}$$

$$C_{gi} + D_{gi} = C_{ci}(\frac{R_{ci}}{R_{co}})^{6i} + D_{ci}(\frac{R_{ci}}{R_{co}})^{-6i} \tag{4.75}$$

$$\frac{\lambda_g}{\lambda_c}(6iC_{gi} - 6iD_{gi}) = 6iC_{ci}(\frac{R_{ci}}{R_{co}})^{6i-1} - 6iD_{ci}(\frac{R_{ci}}{R_{co}})^{-6i-1} \tag{4.76}$$

$$C_{ci} + D_{ci} = Nu(C_{li} + D_{li}) \tag{4.77}$$

$$\frac{\lambda_c}{\lambda_l}(6iC_{ci} - 6iD_{ci}) = Nu(6iC_{li} - 6iD_{li}) \tag{4.78}$$

Then, by solving the equation 4.68-4.72, we can get

$$A_f = 1 - \frac{\lambda_l}{\lambda_c} Nu \ln \frac{R_{ci}}{R_{co}} + \frac{\lambda_l}{2\lambda_f} Nu \tag{4.79}$$

$$A_g = 1 - \frac{\lambda_l}{\lambda_c} Nu \ln \frac{R_{ci}}{R_{co}} \tag{4.80}$$

$$B_g = -\frac{\lambda_l}{\lambda_g} Nu \tag{4.81}$$

$$B_c = -\frac{\lambda_l}{\lambda_c} Nu \tag{4.82}$$

$$B_l = -Nu \tag{4.83}$$

The solution for the serial coefficients

$$C_{gi} = \frac{1}{2}(\frac{R_f}{R_{ci}})^{-6i}(1 + \frac{\lambda_f R_f}{\lambda_g R_{ci}})C_{fi} \tag{4.84}$$

$$D_{gi} = \frac{1}{2}(\frac{R_f}{R_{ci}})^{6i}(1 - \frac{\lambda_f R_f}{\lambda_g R_{ci}})C_{fi} \tag{4.85}$$

$$C_{ci} = \frac{1}{4}(\frac{R_{ci}}{R_{co}})^{-6i}\left[(1 + \frac{\lambda_g R_{ci}}{\lambda_c R_{co}})(1 + \frac{\lambda_f R_f}{\lambda_g R_{ci}})(\frac{R_f}{R_{ci}})^{-6i} + (1 - \frac{\lambda_g R_{ci}}{\lambda_c R_{co}})(1 - \frac{\lambda_f R_f}{\lambda_g R_{ci}})(R_{ci})^{6i}\right] C_{fi} \tag{4.86}$$

$$D_{ci} = \frac{1}{4}(\frac{R_{ci}}{R_{co}})^{6i}\left[(1-\frac{\lambda_g R_{ci}}{\lambda_c R_{co}})(1+\frac{\lambda_f R_f}{\lambda_g R_{ci}})(\frac{R_f}{R_{ci}})^{-6i}+(1+\frac{\lambda_g R_{ci}}{\lambda_c R_{co}})(1-\frac{\lambda_f R_f}{\lambda_g R_{ci}})(R_{ci})^{6i}\right]C_{fi} \tag{4.87}$$

$$C_{li} = \frac{1}{2Nu}\left[(1+\frac{\lambda_c}{\lambda_l})C_{ci}+(1-\frac{\lambda_c}{\lambda_l})D_{ci}\right] \tag{4.88}$$

$$D_{li} = \frac{1}{2Nu}\left[(1-\frac{\lambda_c}{\lambda_l})C_{ci}+(1+\frac{\lambda_c}{\lambda_l})D_{ci}\right] \tag{4.89}$$

Then, substituting the coefficients into the equations.

$$\theta_f = 1-\frac{\lambda_l}{\lambda_c}Nu\ln\frac{R_{ci}}{R_{co}}+\frac{\lambda_l}{2\lambda_f}Nu-\frac{\lambda_l}{2\lambda_f}Nu(\frac{r}{R_f})^2+\sum_{i=1}^{\infty}\left[C_{fi}(\frac{r}{R_f})^{6i}\cos(6i\varphi)\right] \tag{4.90}$$

$$\theta_g = 1-\frac{\lambda_l}{\lambda_c}Nu\ln\frac{R_{ci}}{R_{co}}-\frac{\lambda_l}{\lambda_g}Nu\ln\frac{r}{R_{ci}}+\sum_{i=1}^{\infty}\left[C_{gi}(\frac{r}{R_{ci}})^{6i}+D_{gi}(\frac{r}{R_{ci}})^{-6i}\right]\cos(6i\varphi) \tag{4.91}$$

$$\theta_c = 1-\frac{\lambda_l}{\lambda_c}Nu\ln\frac{r}{R_{co}}+\sum_{i=1}^{\infty}\left[C_{ci}(\frac{r}{R_{co}})^{6i}+D_{ci}(\frac{r}{R_{co}})^{-6i}\right]\cos(6i\varphi) \tag{4.92}$$

$$\begin{aligned}\theta_l &= 1-NuB_l\ln(\gamma)e^{\frac{R_{co}u_\varphi\gamma}{\alpha}\varphi}\\ &+\frac{4R_{co}(\frac{C_f}{8})^{\frac{1}{2}(m+1)}u_a^m Nu}{D_e\nu^m Re_{co}^m}\left[\frac{(\gamma-1)^{m+2}}{(m+2)^2}+\frac{(\gamma-1)^{m+1}}{(m+1)^2(m+2)}-\frac{1}{(m+1)(m+2)}\int_1^{\gamma}\frac{(\gamma-1)^m}{\gamma}d(\gamma)\right]\\ &+Nu\sum_{i=1}^{\infty}\left[C_{li}\gamma^{6i}+D_{li}\gamma^{-6i}\right]\cos(6i\varphi)\end{aligned} \tag{4.93}$$

Then the only unknown coefficients are C_{li} and D_{li}. The above equation can be substituted into the boundary condition equation 4.24, to simplify the equation, a special condition $u_\varphi = 0$ is used, then we get:
if $\gamma = \frac{P/D}{\cos\varphi}$, and $0 \le \varphi \le \pi/6$, then

$$\begin{aligned}&-\frac{Nu}{\gamma}+\frac{4R_{co}(\frac{C_f}{8})^{\frac{1}{2}(m+1)}u_a^m Nu}{D_e\nu^m Re_{co}^m}\left[\frac{(\gamma-1)^{m+1}}{m+2}+\frac{(\gamma-1)^m}{(m+1)(m+2)}-\frac{(\gamma-1)^m}{(m+1)(m+2)\gamma}\right]\\ &+Nu\sum_{i=1}^{\infty}\left[6iC_{li}\gamma^{6i-1}-6iD_{li}\gamma^{-6i-1}\right]\cos(6i\varphi) = -\frac{\sin(\varphi)}{P/D}Nu\sum_{i=1}^{\infty}6i\left[C_{li}\gamma^{6i}+D_{li}\gamma^{-6i}\right]\sin(6i\varphi)\end{aligned} \tag{4.94}$$

To get the two serial coefficients, in approximation of a finite serial, $i = 1, 2, 3, ..I$, then chose $2I$ points with the value $\varphi = \varphi_1, \varphi_2, \varphi_3, ...\varphi_{2I}$, finally, we can get an equation group, and the two serial coefficients can be obtained by solving the equation group.

4.1.5. Practical results for engineering

Based on the solution of governing equations, several practical results for engineering interest can be obtained.

The center temperature of the fuel:

$$\theta_{fc} = 1 - \frac{\lambda_l}{\lambda_c} Nu \ln \frac{R_{ci}}{R_{co}} + \frac{\lambda_l}{2\lambda_f} Nu \tag{4.95}$$

The outer cladding surface temperature:

$$\theta_{wall} = 1 + \sum_{i=1}^{\infty} [C_{ci} + D_{ci}] \cos(6i\varphi) \tag{4.96}$$

The circumferential heat flux distribution:

$$q(\varphi) = \lambda_l \left(\frac{\partial T_l}{\partial r} \right)_{r=R_{co}} \tag{4.97}$$

The dimensionless form is

$$\frac{q(\varphi)}{q_{av}} = -\frac{1}{Nu} \left(\frac{\partial \theta_l}{\partial \gamma} \right)_{\gamma=1} \tag{4.98}$$

Then

$$\frac{q(\varphi)}{q_{av}} = B_l e^{\frac{R_{co} u_\varphi}{\alpha} \varphi} - \sum_{i=1}^{\infty} 6i \left[C_{li} - D_{li} \right] \cos(6i\varphi) \tag{4.99}$$

or in another form

$$\frac{q(\varphi)}{q_{av}} = B_l e^{\frac{R_{co} u_\varphi}{\alpha} \varphi} - \frac{\lambda_c}{\lambda_l} \sum_{i=1}^{\infty} 6i \left[C_{ci} - D_{ci} \right] \cos(6i\varphi) \tag{4.100}$$

where B_l is defined as, if $u_\varphi = 0$, then

$$B_l = 1 \tag{4.101}$$

else $u_\varphi \neq 0$, then

$$B_l = \frac{\frac{R_{co} u_\varphi}{\alpha}}{e^{\frac{\pi R_{co} u_\varphi}{6\alpha}} - 1} \tag{4.102}$$

The average heat transfer coefficient is

$$htc_{av} = \frac{q_{av}}{T_{co,av} - T_b} \tag{4.103}$$

where $T_{co,av}$ is the average outer wall surface temperature of the cladding.

The dimensionless heat transfer coefficient distribution shape function is given by:

$$\frac{htc(\varphi)}{htc_{av}} = \frac{q(\varphi)}{T_w(\varphi) - T_b} \frac{1}{htc_{av}} = \frac{q(\varphi)}{T_w(\varphi) - T_b} \frac{T_{co,av} - T_b}{q_{av}} = \frac{q(\varphi)/q_{av}}{\theta_{wall}} \tag{4.104}$$

Substituting the equations 4.95 and 4.99 into Eqn. 4.102, then we can get

$$\frac{htc(\varphi)}{htc_{av}} = \frac{B_l e^{\frac{R_{co} u_\varphi}{\alpha} \varphi} - \frac{\lambda_c}{\lambda_l} \sum_{i=1}^{\infty} 6i \left[C_{ci} - D_{ci} \right] \cos(6i\varphi)}{1 + \sum_{i=1}^{\infty} \left[C_{ci} + D_{ci} \right] \cos(6i\varphi)} \tag{4.105}$$

Here, to simplify the equation, the special solution of the coefficients of Eqn. 4.94 with the value $I = 1$, $\varphi = 0$ and $\varphi = \frac{\pi}{12}$ are implemented. We can get

$$\frac{C_{c1} - D_{c1}}{C_{c1} + D_{c1}} = \frac{D}{P} \sin(\frac{\pi}{12}) \tag{4.106}$$

Finally, the simplified equation is

$$\frac{htc(\varphi)}{htc_{av}} = B_l e^{\frac{R_{co} u_\varphi}{\alpha} \varphi} - 6 \sin(\frac{\pi}{12}) \frac{D\lambda_c}{P\lambda_l} \cos(6\varphi) \tag{4.107}$$

If ϵ is used instead of $\frac{R_{co} u_{\varphi 0}}{\alpha}$, by substituting it into Eqn. 4.107, the first term on the right hand side can be written as

$$B_l e^{\frac{R_{co} u_\varphi}{\alpha} \varphi} = \frac{\epsilon e^\epsilon}{e^{\frac{\pi}{6}\epsilon} - 1} e^{\left(\frac{P/D - 1}{\frac{P/D}{\cos\varphi} - 1} \right) \varphi} \tag{4.108}$$

In the special case of bare rods, in which the transverse flow velocity $u_\varphi = 0$, then we can get $B_l = \frac{6}{\pi}$, and the normalized local heat transfer coefficient equation

$$\frac{htc(\varphi)}{htc_{av}} = 1 - 6 \sin(\frac{\pi}{12}) \frac{D\lambda_c}{P\lambda_l} \cos(6\varphi) \tag{4.109}$$

Compared with the previous research work carried by Nijsing and Eifler (1969) and Yang et al. (2013). The new correlation proposed in present study is specified on the liquid sodium cooled triangular arrayed fuel assembly. The new equation is more simple and practical for engineering without any user given coefficients, compared with Eqn. 1.6 and Eqn. 1.7. The most distinguished point in the present study is that the sweeping flow correlation Eqn. 3.16 is substituted in the derivation. But the first term of Eqn. 4.107 which is dominating the sweeping flow is not physically reasonable. The special solution with 0 sweeping flow velocity is given as Eqn. 4.109. Since experimental results are not available from the open literature, two numerical experiments (for both bare rod and wire wrapped rod) with CFD are carried out to validate the new correlation.

4.2. CFD analysis

To investigate the local heat transfer phenomena of a triangular arrayed rod bundle, the computational fluid dynamics method is used in the present study. With the CFD tools, it is possible to visualize the temperature distribution in the rod and coolant, and give the heat flux distribution curve around the rod surface. In the present study, the open source code OpenFOAM is used to simulate the conjugated heat transfer of fuel rod and coolant. As mentioned in the previous sections, the local heat transfer is dominated by both, the geometry of sub-channel and the sweeping flow induced by the wire. Two different CFD models are carried out for a bare rod bundle and a wire wrapped rod bundle.

4.2.1. CFD model for a bare rod bundle

In the present study, a CFD model is created for a hypothetical bare rod bundle to study the geometry effect of the sub-channel. The wire spacers are not included in the bare rod bundle. The local heat transfer of bare rod bundle is mainly dominated by the triangular array pattern. The geometry parameters of the bare rod bundle are illustrated as Table 4.1. For a bare rod bundle with a infinite number of rods, it is possible to simulate a finite fuel-coolant element with the symmetrical boundaries.

Table 4.1.: Geometric parameters of the bare rod bundle

P/D ratio	D_r [mm]	P [mm]
1.11	9.7	10.8

Table 4.2.: Thermal properties of the fuel rod and coolant

Material	ρ $[kg/m^3]$	λ $[W/m/K]$	C_p $[J/kg/K]$	μ $[Pa \cdot s]$
Fuel	10980	3.2	310	-
Cladding	7933	19	460	-
Liquid sodium	849.4	70.6	1270	2.69e-4

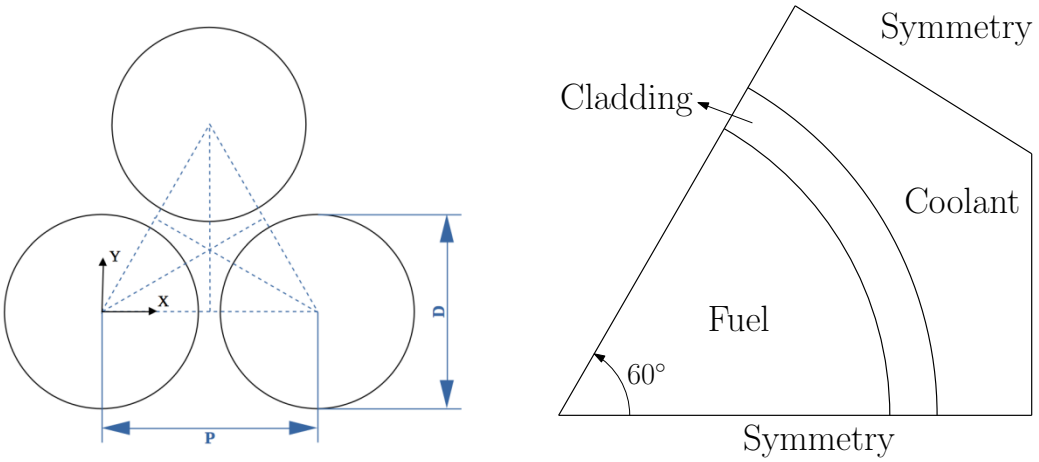

Figure 4.2.: A finite fuel element with a symmetry boundary

The thermal properties of the fuel and coolant are given as Table 4.2.

As shown in Fig. 4.2, the left figure shows three triangular arrayed rods from a bare rod bundle. The dashed lines are the connections between rod centers, and the rod center to the middle point of the connections. Each of the dashed lines aligns on a symmetry boundary. Taking the advantage of the symmetry boundaries, one finite fuel element, as shown in the right figure, is selected as the simulation domain. This domain includes 60 degrees of fuel and cladding zone, and coolant zone. In the solid region, only the heat conduction equation is solved. For the flow region of coolant, the turbulent flow field is simulated. While the heat transfer between the solid region and the liquid region are conjugated. In the solid zone of the fuel, a volume heat source is added to simulate the energy release by the fission reaction. For the coolant region, the periodic inlet outlet boundaries are imposed with an average inlet velocity. With the periodic boundary condition, a short section of simulation domain is enough to get a developed flow. The periodical boundary for energy equation will be introduced in the this section.

To simulate the conjugated heat transfer in the finite fuel element, a 3D structured mesh is generated with the OpenFOAM blockMesh utility. The axial length of the mesh is 10 mm, which should have no influence on the simulation result with periodic inlet outlet boundary conditions. The cross section of the mesh is shown as 4.3.

Fig. 4.3 illustrates the three different regions for fuel, cladding and coolant. This figure also illustrates the structured mesh with the consideration of the wall boundary layer in the fluid region. To analyze the effect of mesh resolution on the simulation result, 5 different meshes are generated for a sensitivity study. The grid numbers of the meshes are given

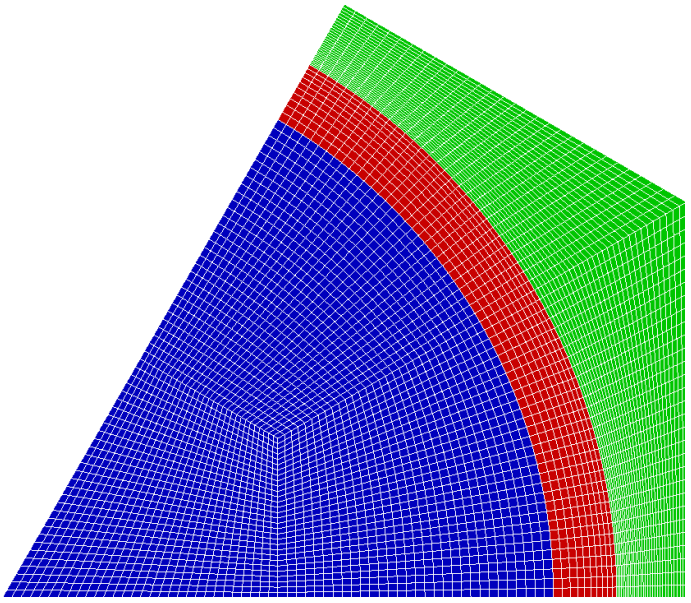

Figure 4.3.: The cross section of mesh and regions

in Table 4.3. The average $y+$ varies from 5.05 to 0.84, and the grid number is up to 0.7 million.

Table 4.3.: Meshes of bare rod bundle for sensitivity study

	mesh1	mesh2	mesh3	mesh4	mesh5
Average yPlus	5.05	3.28	2.22	1.56	0.84
Grid number	38250	88000	181250	306000	736000

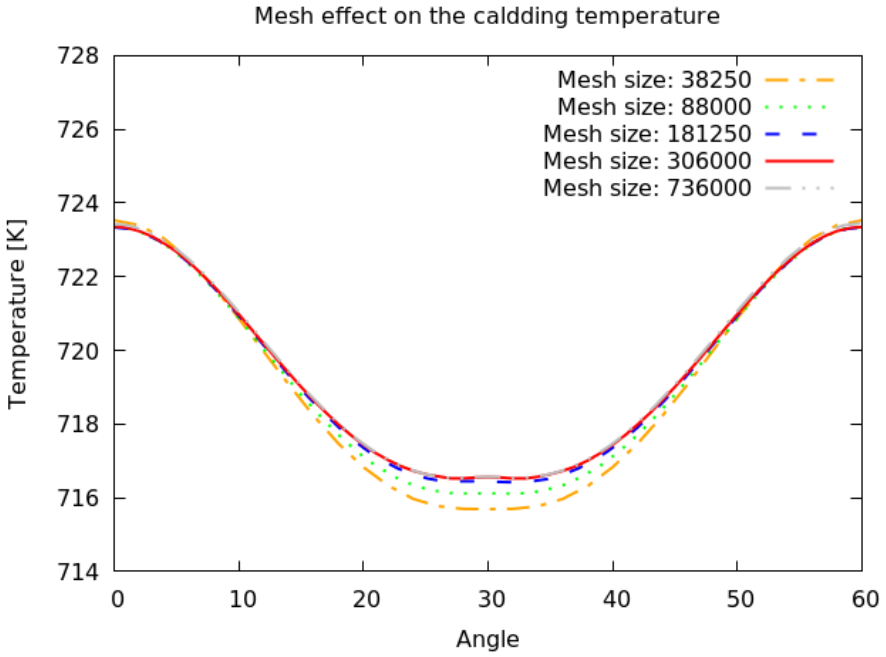

Figure 4.4.: Mesh effect on the cladding temperature

After obtaining the converged results of the steady state simulations with the 5 meshes, the

outer surface temperature of the cladding is investigated. The mesh sensitivity simulation result is given as Fig. 4.4. The cladding temperatures obtained with different meshes are compared. The cladding temperature almost doesn't change anymore when the mesh size is up to about 0.3 million. Finally, the result of Mesh4 is selected for further study.

To simulate the developed flow, a periodical boundary is used for the momentum equation. A simple model is implemented to the energy equation for periodical boundary conditions. If the linear power density of the rod bundle is constant, then the fluid is heated uniformly in the flow direction. The enthalpy is divided into mean enthalpy and variant enthalpy. The mean enthalpy of the fluid should be a linear distribution along the axial direction.

$$h = h_m + h' \tag{4.110}$$

where the mean enthalpy of the fluid is h_m, and it is a linear function of z. h' is the variant enthalpy.

The energy equation used in OpenFOAM [Jasak et al. (2007)] is given as following.

$$\nabla \cdot (\rho \vec{u} h) + \nabla \cdot (\rho \vec{u} \cdot \frac{1}{2}|\vec{u}|^2) = \nabla^2(\alpha_{eff} h) + \rho \vec{u} \cdot \vec{g} \tag{4.111}$$

where α_{eff} is the effective thermal diffusivity.

By substituting the definition of h into the energy equation, we get

$$\nabla \cdot (\rho \vec{u} h_m) + \nabla \cdot (\rho \vec{u} h') + \nabla \cdot (\rho \vec{u} \cdot \frac{1}{2}|\vec{u}|^2) = \nabla^2(\alpha_{eff} h_m) + \nabla^2(\alpha_{eff} h') + \rho \vec{u} \cdot \vec{g} \tag{4.112}$$

The first term on the left hand side can be derived into

$$\nabla \cdot (\rho \vec{u} h_m) = h_m \nabla \cdot (\rho \vec{u}) + \rho \vec{u} \cdot \nabla h_m \tag{4.113}$$

With the mass conservation equation for incompressible fluid, the first term on the right hand side is 0. h_m is a function $h_m(z)$, then

$$\rho \vec{u} \cdot \nabla h_m = \rho u_z \frac{dh_m}{dz} \tag{4.114}$$

Then

$$\rho u_z \frac{dh_m}{dz} = u_z \frac{q'}{A u_m} \tag{4.115}$$

where q' is the linear power density of the rod bundle, and A is the flow cross section area. u_m is the mean flow velocity in the flow channel.

Since h_m is a linear function, the first term on the right hand side of the energy equation is

$$\nabla^2(\alpha_{eff} h_m) = 0 \tag{4.116}$$

So the final form of the energy equation is

$$\nabla \cdot (\rho \vec{u} h') + \nabla \cdot (\rho \vec{u} \cdot \frac{1}{2}|\vec{u}|^2) + u_z \frac{q'}{A u_m} = \nabla^2(\alpha_{eff} h') + \rho \vec{u} \cdot \vec{g} \tag{4.117}$$

With the extra term as a function of linear power, local axial velocity, and mean velocity in the equation, it is possible to use the cyclic boundary condition for the energy equation. The principle idea of the cyclic boundary is that the extra term of the energy equation works like a heat sink. It removes the energy from the coolant. On one hand side, the

heat is released from the volume heat source term in fuel zone, and the heat is transferred into the liquid sodium coolant region. On the other hand side, the heat is removed out from the coolant region by the extra term. Then the temperature of the coolant doesn't change in the axial flow direction.

The periodical boundary condition for heat transfer is a good solution for a single pipe problem, such as the heat transfer inside one single heat exchanger tube. In the CFD model for the bare rod, the periodical boundary for heat transfer can be applied.

4.2.2. CFD model for a wire wrapped rod bundle

In the present study, a 19 wire wrapped rod bundle is simulated by CFD. The geometry parameters of the wire wrapped rod bundle are shown as Table 4.4. The geometry information is from the engineering design of the ASTRID reactor, and it is provided by the SESAME project partner.

Table 4.4.: Geometric parameters of rod bundle

P/D ratio	D_w [mm]	D_r [mm]	P [mm]	H [mm]
1.11	1.0	9.7	10.8	180

With the CAD geometry model of the 19-rod bundle, a multi-regional mesh was generated. In the present study, the mesh generation tool of OpenFOAM snappyHexMesh is used to create the hex dominated mesh for complex geometries.

To simulate the conjugated heat transfer between rod and coolant, the simulation domain is split into two regions. The space occupied by the coolant is the fluid zone, while the rods and wire spacers are solid zone. In the CFD simulation, the two regions are simulated separately, but the thermal interfaces are coupled. The temperature and heat flux on the wall surface of rods are equal to the wall boundary of the coolant.

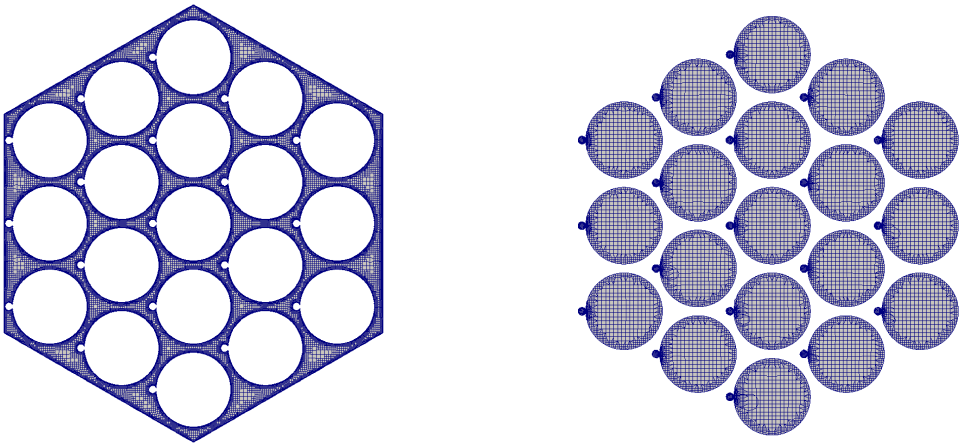

Figure 4.5.: Cross section of the 3D mesh

In the solid region, only the heat conduction equation is solved, so the mesh is relatively coarse. In the fluid region, a finer mesh is used for solving the equation group for pressure, momentum, energy, turbulence. On the wall interface, the mesh in the solid zone is refined to keep the ratio of its mesh size to the size in the coolant region not too big. The cross section of the generated mesh regions for fuel and coolant are shown as Fig. 4.5.

The CFD simulation is carried out with the OpenFOAM solver chtMultiRegionSimpleFoam, which is a solver for steady state simulations. Both of the liquid and solid regions

are solved in the same solver. The energy equations are coupled at the wall interface between the two regions. In the fluid region, the estimated Re number is about 10^7, and the $k-\omega$ sst model is used for turbulent simulation. Since the additional wall boundary layers are added to the fluid region, the average $y+$ is about 13.

In this simulation. The heat generated by the fission reaction is simulated by an internal volume heat source in the solid zone. The internal volume heat source of rod is 5.393×10^8 W/m^3. The inlet velocity of liquid sodium in fluid region is 7.53 m/s, and the inlet temperature is 728 K. The thermal properties of sodium coolant and fuel rod are given in Table 4.2.

For the wire wrapped rod bundle case, the periodical boundary can not be applied. The flow area is divided into sub-channels, but the internal sub-channel is heated by three rods, while the wall sub-channel is heated by two rods. The hydraulic diameter of the internal channel is smaller than the wall channel. The heating power for the internal channel is much higher than the wall channel, so the energy released to the coolant is accumulated. The energy removal rate is the same for different sub-channels, but the heating rate is different. The temperature field can not reach a "heat balance" and no converged result can be obtained.

To get a developed flow field, the length of the CFD model is equal to two pitches of wire. The normal inlet outlet boundary condition is implemented. The inlet effect length is estimated to be 20 times of the hydraulic diameter of the sub-channel, so it is much smaller than half of one wire pitch. The result from the middle part of the CFD region would be used for analysis. In the present CFD model, a constant velocity is given at the inlet boundary and a constant pressure at the outlet boundary.

The steady state solution is converged after about 2000 iterations. To check the energy balance, the mean temperature on the outlet panel is the integration of temperature weighted by the axial velocity, and divided by the integration of axial velocity over the outlet panel area. The velocity weighted mean temperature can be calculated with equation

$$T_m = \frac{\int_A T u_z ds}{\int_A u_z ds} \tag{4.118}$$

where A is the flow cross section area.

The energy balance error can be estimated by the equation

$$\epsilon = \frac{|QV_{rod} - \rho C_p u_a (T_{m,out} - T_{in})|}{QV_{rod}} \tag{4.119}$$

where Q is the volume heat flux, and V_{rod} is the volume of rods. u_a is the axial mean velocity. $T_{m,out}$ is the mean outlet temperature, and T_{in} is the inlet temperature.

By comparing the energy taken by the fluid and the total power of the rod bundles, the calculated error of the energy balance is less than 1%.

4.2.3. Conjugated heat transfer simulation results

The steady state simulations of conjugated heat transfer of the bare rod bundle and the wire wrapped rod bundle are carried out. The simulation results of the two case with and without wires are analyzed.

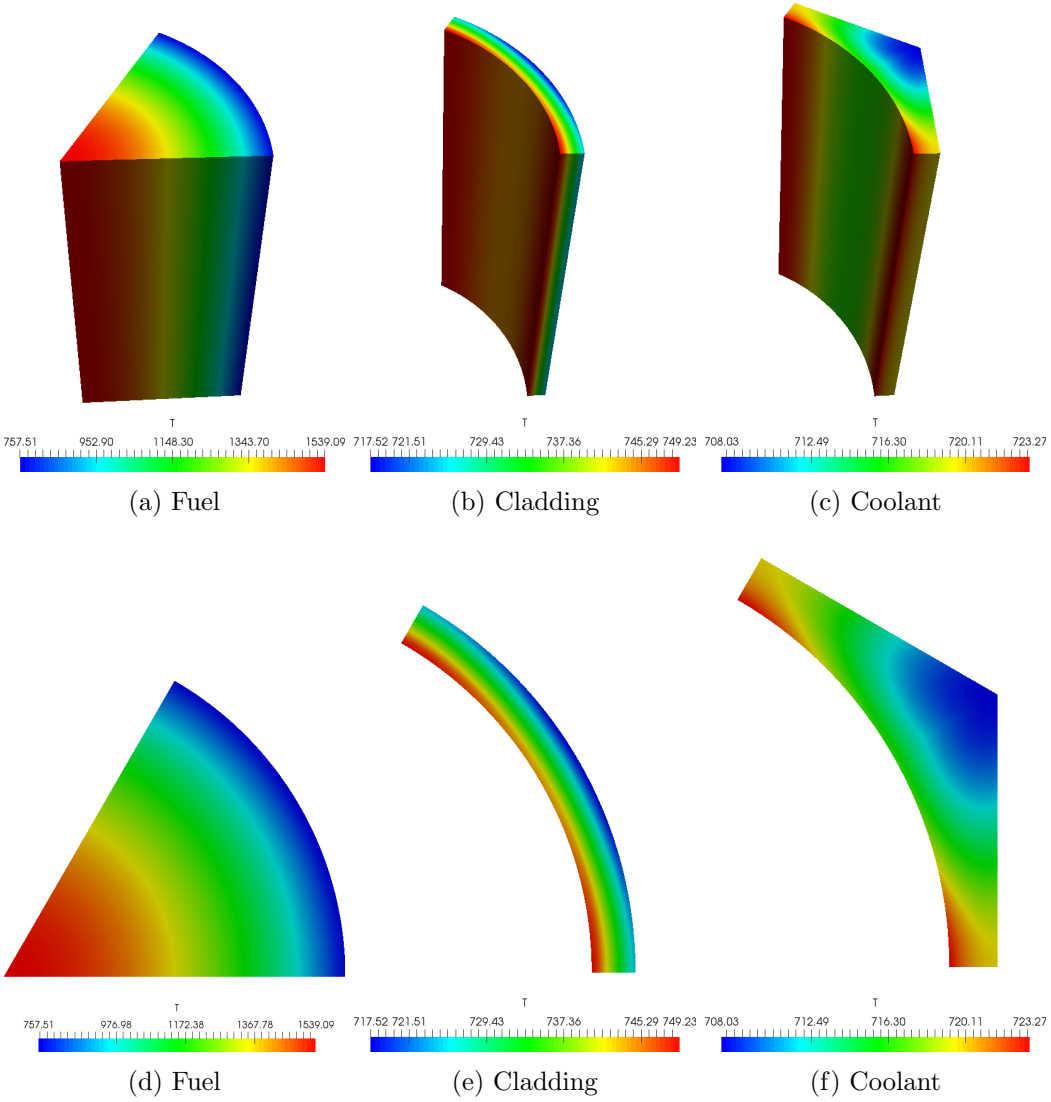

(a) Fuel (b) Cladding (c) Coolant

(d) Fuel (e) Cladding (f) Coolant

Figure 4.6.: Temperature field of the bare rod bundle

Simulation result of bare rod bundle

With the simulation of the conjugated multiple regions heat transfer of a bare rod bundle, the temperature field and the wall heat flux distribution are obtained.

Since the periodic inlet outlet boundary is used for the heat transfer simulation, the variant temperature (corresponding to the variant enthalpy) field of the cross section doesn't change in the axial flow direction. Although the variant temperature is not the physical temperature, it can be used to calculate the heat transfer coefficient and also the Nusselt number. As shown in Fig. 4.6, the variant temperature fields of fuel, cladding and coolant are given. The heat is generated in the fuel with a uniform volume heat source, and is transferred though the cladding to the coolant. The position with the highest temperature is in the center of the fuel. The temperature gradient is large in the radial direction. In the region of cladding, the middle part of the section has a lower temperature, especially at the outer surface of the cladding. In the coolant region, the flow field close to the gap has a higher temperature, while the temperature is lower in the near sub-channel central area.

In the present study, we focus on the temperature difference between the outer surface of the cladding and the bulk temperature of the coolant. The mass flow weighted temperature

of coolant over the cross section is 713.9 K. The outer surface temperature of cladding varying with angle is shown as Fig. 4.7. The outer surface of cladding facing to the sub-channel center has a lower temperature than the part facing to the gap. With the coolant bulk temperature and the cladding surface temperature, the normalized heat transfer coefficient varying with angle is obtained. The definition of the normalized heat transfer coefficient is given as the following equation.

$$htc^*(\theta) = \frac{htc(\theta)}{htc_{av}} \tag{4.120}$$

where the htc_{av} is the average heat transfer coefficient.

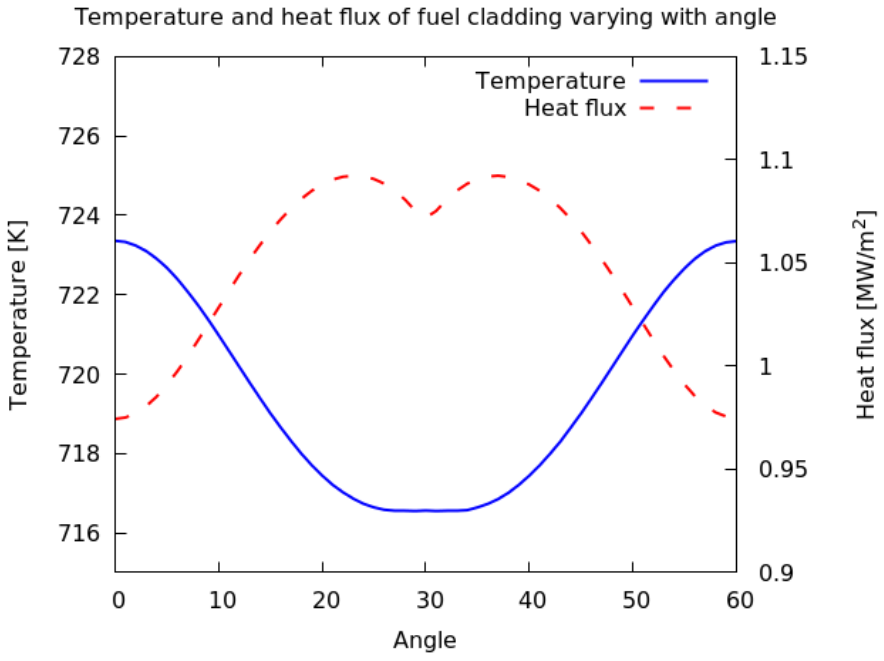

Figure 4.7.: Circumferential temperature and heat flux distribution of cladding

In Fig. 4.7, the distribution of temperature and heat flux are given. The distribution shape of the heat flux is in contrast to the temperature. In the middle part at around 30 degrees, the heat flux is lower, while the temperature is higher. For the heat flux distribution, there is a small dip in the middle. This is because of the circumferential heat conduction of the cladding material.

Simulation result of wire wrapped rod bundle

With the steady state simulation of the wire wrapped 19-rod bundle, the converged result of the conjugated heat transfer is obtained. As shown in Fig. 4.8, the temperature of the sodium coolant increases in the axial direction, as heated by the rods. The central channel has a higher temperature than the wall channels. In the temperature field of rods, the temperature of center line of each rod is much higher than the rod surface that is cooled by the sodium coolant. It is similar to a one dimensional heat conduction for a cylinder with internal heat source. The heat conductivity of fuel is relatively small, so the temperature gradient is very high in its radial direction. First, the temperature field of the coolant zone is studied. The temperature fields of the cross sections of the coolant zone at different elevations in the axial direction are extracted.

Figure 4.9 shows the temperature fields of the cross sections of the coolant zone. Here, the wire position angle is used to represent the elevation of the cross sections. In the

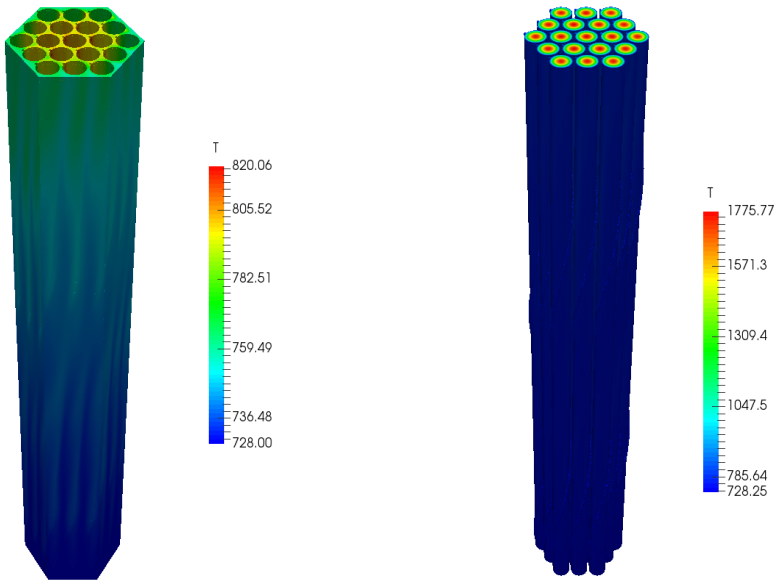

(a) Coolant (b) Rods

Figure 4.8.: Temperature distribution of coolant and rods [Unit: K]

temperature fields, the positions of the hot spots are investigated. In the flow direction, the wire rotates in anti-clock wise direction from to top to down view, the small coolant region close to the down-wind side of the wire spacer has a higher temperature. The temperature at up-wind side of the wire spacer is relatively lower. The regions at the positions of the narrow gaps between the rods have a higher temperature. This is because of the wall effect from the two near wall surfaces of the two neighbour rods. The high temperature spot usually appears behind the wire or exactly on the gap. The near rod surface local region facing toward the center of sub-channel is relatively colder, but the temperature at the local region in the gap between two rods is relatively higher. This phenomena is very similar to the bare rod bundle case. This is induced by the triangular arrangement of the rods. The present study is going to figure out if the rods arrangement pattern is the dominate factor of the local heat transfer, compared with the wire effect.

Fig. 4.10 shows the turbulent thermal diffusivity field. The high turbulent thermal diffusivity zone is in the wall channels. It is because of a bigger hydraulic diameter. The bigger hydraulic diameter results a lower flow resistance which leads to a higher local velocity in the wall channels. The Re number is also relatively higher in the wall channels. The movement of the high turbulent thermal diffusivity regions is influenced by the positions of the wires. The wires positions rotate in the outer wall channels ring. They rotate in the anti-clockwise direction from the top-to-down view of the flow passage. The high turbulent thermal diffusivity regions follows the rotation of the wires in the outer wall channels ring.

4.3. Assessment of the new model

To validate the proposed model given as Eqn. 4.109, the CFD simulation results of the bare rod bundle and the wire wrapped rod bundle are compared with the proposed correlation. For the bare rod bundle case, only 60 degree distribution is given, because of the circumferential periodical boundary condition. For the wire wrapped rod bundle, the 360 degree local heat transfer distribution is given. The present study focus on the local heat transfer coefficient distribution. As mentioned before, two important geometry factors are involved: (1) The triangular arrayed pattern of the rods; (2) The helical wire

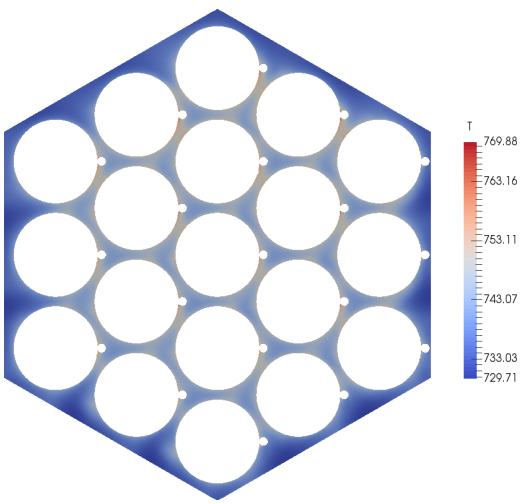

(a) $\varphi = 90°$

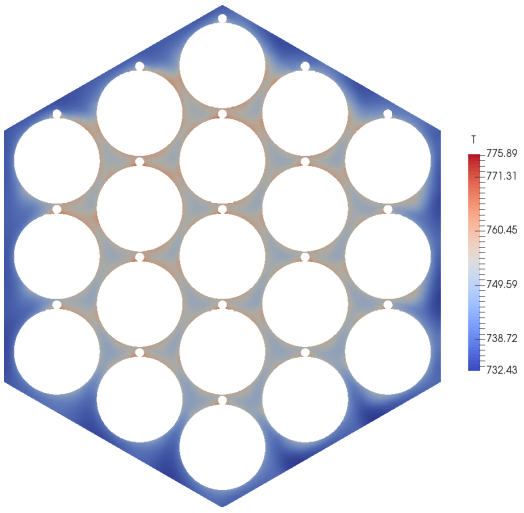

(b) $\varphi = 180°$

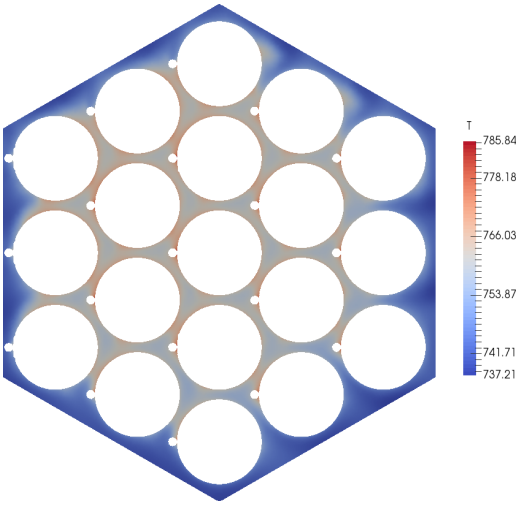

(c) $\varphi = 270°$

Figure 4.9.: Temperature distribution of coolant at different wire position angle [Unit: K]

spacers wrapped on the rod. While, the new proposed model Eqn. 4.109 is a simplified special version for the bare rod bundle. If both the CFD simulation results for rod bundle with and without wires agree with the new proposed correlation. It means the triangular arrangement shape is the dominant factor. Because the benchmark test data can not be found from the open literature, this new proposed model is only compared with the "numerical test" data.

In Fig. 4.11, the dimensionless normalized heat transfer coefficient of the bare rod is compared to the proposed model. The angle rotates from one gap to another gap between two rod. The positions at the bare rod surface facing to the gaps are 0 degree and 60 degree. At the position of 30 degree angle, this area is facing to the center of the sub-channel.

The normalized heat transfer coefficient varies with the circumferential position. The CFD result of the bare rod gives a cosine like distribution shape. The distribution shape is very similar to the proposed correlation, but the amplitude is bigger than the proposed model. But this comparison proves the non-uniform distribution of local heat transfer coefficient. The rod surface area facing to the sub-channel center has a higher local heat transfer coefficient.

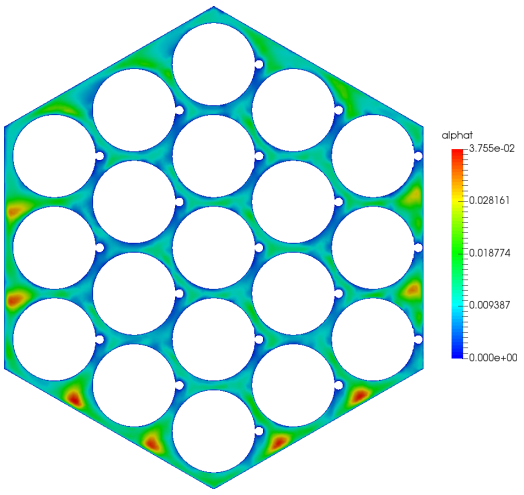

(a) $\varphi = 90°$

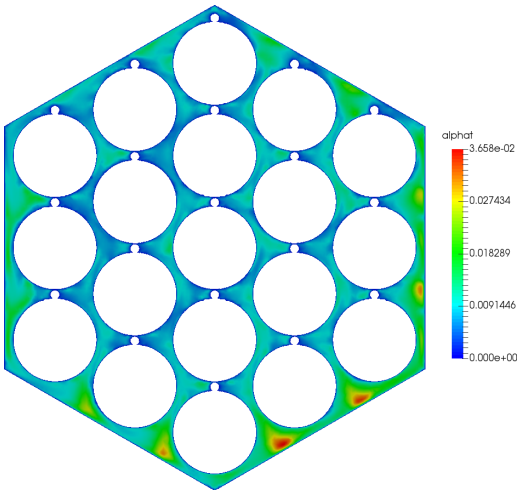

(b) $\varphi = 180°$

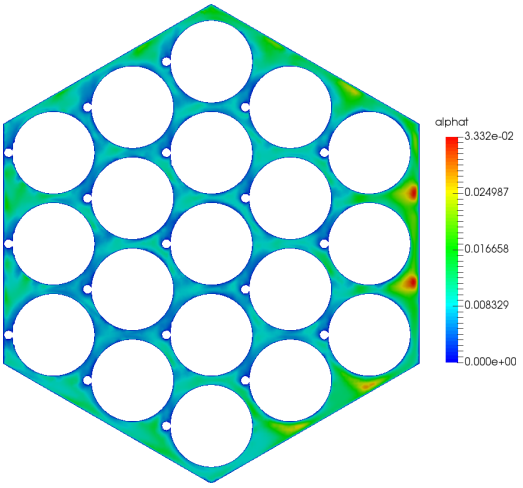

(c) $\varphi = 270°$

Figure 4.10.: Turbulent thermal diffussivity distribution of coolant zone at different wire position angle [Unit: m^2/s]

From the middle section of the CFD model for the wire wrapped rod bundle, the cladding surface temperature and heat flux are retrieved to calculate the local heat transfer coefficient. The bulk temperature is the mass flow rate weighted temperature of the coolant. In Fig. 4.12, the normalized heat transfer coefficient obtained from the CFD result is compared with the proposed model. The comparison shows that the proposed model is in good agreement with the CFD result, except the two contact points between the wire spacer and the rod surfaces. The contact points results two hot spots and low heat flux, then the calculated heat transfer coefficients at the two contact points are much lower. Although the heat transfer is effected by the wire spacer, but the distribution shape is also a cosine like shape. This result proves that the triangular arrangement shape is the main dominate factor for the local heat transfer.

The cosine like local heat transfer distribution model is compared with the simulation results of the bare rod bundle and the wire wrapped rod bundle. The proposed model gives a detailed heat transfer distribution around the fuel rod. The assessment shows that the new proposed model can be used to estimate the local heat transfer of both bare rod bundle and wire wrapped rod bundle.

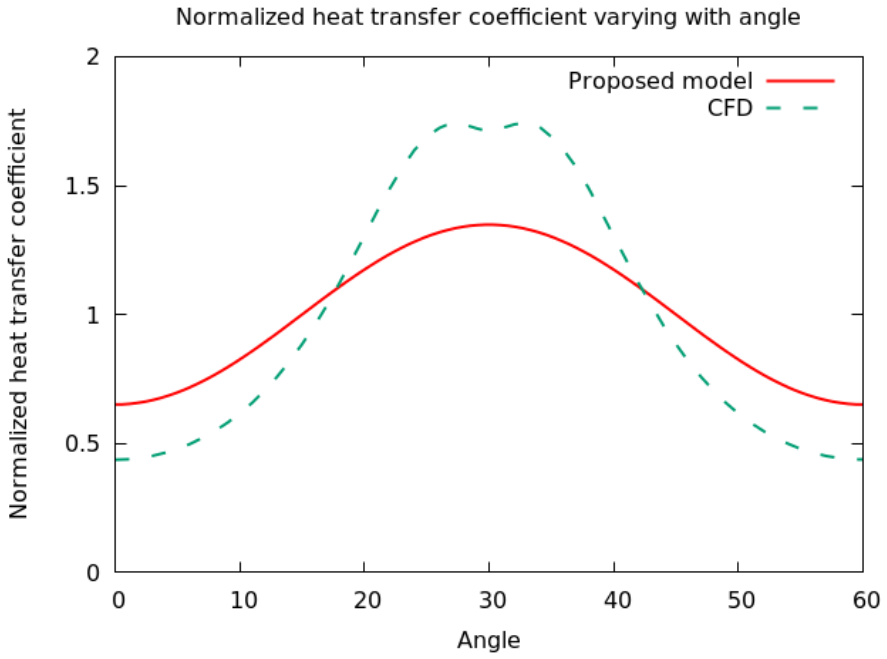

Figure 4.11.: Normalized local heat transfer coefficient of the bare rod

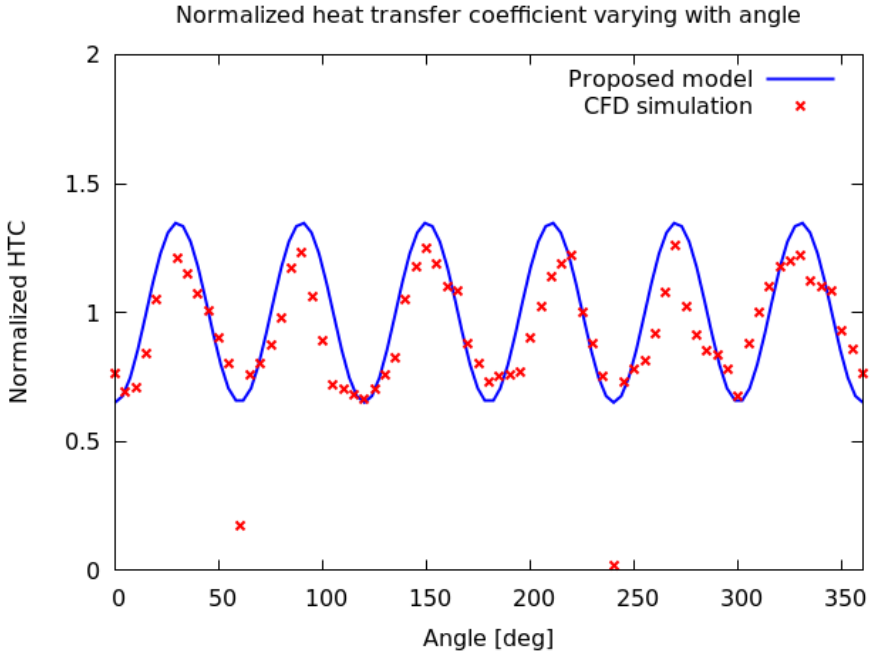

Figure 4.12.: Circumferential heat transfer of the wire wrapped rod

5. Sub-channel analysis

In the present study, $MATRA\_X0$(Multichannel Analyzer for steady states and Transients in Rod Arrays) which is designed for water cooled reactors is used. In this code, the basic concept of the sub-channel analysis, in which the flow area of fuel rod bundle is divided into sub-channels by the gaps between rods or rod to wall is applied. The boundary of the sub-channels is the fuel rod surface, the wall of the assembly and the gaps.

Since $MATRA\_X0$ is only available for water cooled reactors, code improvements are carried out in the present study for liquid metal cooled reactors. The modifications of the code are mainly for the coolant of liquid sodium. Most of the models are obtained from the open literature, these models are already verified in previous studies. The only new model that implemented into MATRA is the local heat transfer model for post-processing.

5.1. Main modifications of code MATRA

5.1.1. Thermal properties of liquid sodium

In recent several decades, the thermal properties of liquid metals which are used as the coolant of some 4th generation reactors are intensively measured by many labs. The thermal properties of sodium are mainly referenced in the open literature by Sobolev (2011) and Fink and Leibowitz (1995). The thermal property library of MATRA is modified from water to liquid sodium with the correlations from open literature. The main thermal properties of liquid sodium are illustrated in Table 5.1.

Table 5.1.: Thermal properties of liquid sodium

Property	Sodium	Unit
Density	$\rho = 1016 - 0.238T$	kg/m^3
Heat conductivity	$\lambda = 104 + 0.047T$	$W/m/K$
Specific heat	$C_p = 1.6582 - 8.479 \times 10^{-4}T + 4.4541 \times 10^{-7}T^2 - 2992.6T^{-2}$	$kJ/kg/K$
Dynamic viscosity	$\ln \mu = 556.835T^{-1} - 0.3958 \ln T - 6.4406$	$Pa \cdot s$
Melting point	$T_m = 371$	K

In the present study, sodium is considered as an incompressible fluid. The enthalpy of sodium is assumed to be a function of temperature, when the temperature is higher than

the melting point. The enthalpy can be calculated as the accumulation of specific heat capacity over the temperature. The enthalpy of liquid sodium is shown as equation 5.1.

$$h(T) = h(T_m) + \int_{T_m}^{T} C_p(T)\mathrm{d}T \tag{5.1}$$

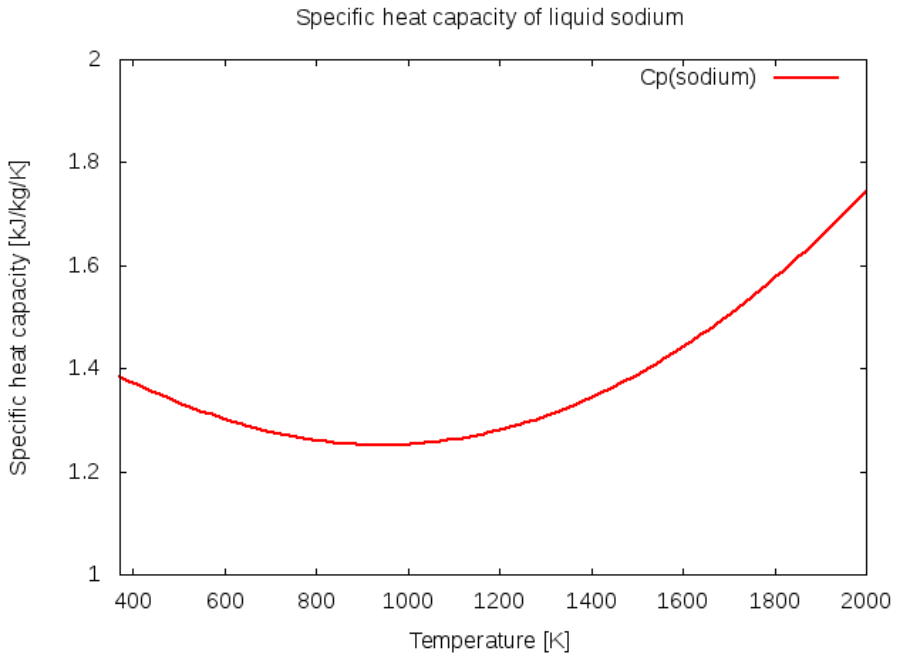

Figure 5.1.: Specific heat of liquid sodium

The specific heat capacity of liquid state sodium is shown in figure 5.1, and the temperature range is 371 K to 2000 K. The enthalpy is solved by the energy equation. The enthalpy is a function of temperature, and we also need the inverse function to get the temperature with an enthalpy input. In the present study, a searching function is created to find the temperature for a given enthalpy input. After the implementation of the thermal property package for sodium, the application of the other physical models related to the flow and heat transfer of liquid sodium are also required.

5.1.2. Pressure drop model

In the design of nuclear reactors, the pressure drop of the core is up to 80% of the whole primary system [Grosjean and Li (2015)]. For liquid metal cooled reactor, the wire spacers are often used to support the fuel pins. The effect from the tight triangular arrangement and the wire spacers on the flow resistance should be considered. As mentioned in previous chapter, several optional correlations are proposed by Novendstern (1972), Rehme (1973) and Cheng and Todreas (1986).

In the code of MATRA, the Rehme model from Rehme (1973) is selected for liquid sodium coolant. In this model, a geometry factor is defined as equation

$$F = \left(\frac{u_{eff}}{u_b}\right)^2 = \left(\frac{P}{D}\right)^{0.5} + \left[7.6\frac{d_m}{H}\left(\frac{P}{D}\right)^2\right]^{2.16} \tag{5.2}$$

where u_{eff} is the effective velocity, which is taking into account of the swirling flow. d_m is the mean diameter of the wire wrap. With the geometry factor, a modified Reynolds number is obtained:

$$Re' = Re\sqrt{F} = \frac{D_e}{\nu}u_b\sqrt{F} \tag{5.3}$$

Then the modified friction factor is correlated as a function of the modified Reynolds number:

$$f' = \frac{64}{Re'} + \frac{0.0816}{Re'^{0.133}} \tag{5.4}$$

The correlation has proved high accuracy with the experiment validations for the wire wrap rod bundle.

5.1.3. Single phase heat transfer model

For a liquid metal cooled reactor, the coolant is assumed as a single phase fluid. So, only the single phase heat transfer correlation is used to calculate the fuel rod to coolant heat transfer. In the sub-channel code of MATRA, the default heat transfer model is the classical Dittus-Boelter correlation [Bergman et al. (2011)], as equation:

$$Nu = 0.023 Re^{0.8} Pr^{0.4} \tag{5.5}$$

The Dittus-Boelter correlation is widely used in the single phase heat transfer of water. For the heat transfer of liquid metal, the Sleicher correlation proposed by Sleicher et al. (1973) was recommended by Cheng et al. (2004). The Sleicher model is shown as following equation.

$$Nu = 0.0167 Pe^{0.85} Pr^{0.08} + 6.3 \tag{5.6}$$

Besides the Sleicher model, two other correlations are also selected for comparison. The first is OECD-NEA model (2007) which is shown as following equation.

$$Nu = 0.022 Pe^{0.8} + 5.75 \tag{5.7}$$

Another correlation is from Seban and Shimazaki (1949), as following equation.

$$Nu = 0.025 Pe^{0.8} + 5.0 \tag{5.8}$$

The Nusselt number predicted with different correlations varying with the Pelect number is shown in figure 5.2.

The different correlations give similar Nusselt numbers. The difference is no more than 20%. The effect of heat transfer models on cladding temperature will be compared in the present study. Compared with the Dittus-Boelter correlation for water, the three correlations for liquid metal have a constant value on the right hand side, this is because of the high thermal conductivity of the liquid metal.

5.1.4. Turbulent mixing model

In the sub-channel approach, the inter-channel mixing can be divided into two parts: first is the diversion flow caused by the resistance distribution, and the second part is the turbulent mixing which is caused by the eddy motion of fluid across the gap. Within the turbulent mixing, the inter-channel net mass flux is 0. In the present study, the diversion flow is mainly caused by the wire spacers, which is called as sweeping flow in the previous chapters. Normally, the sweeping flow is calculated by the flow resistance distribution in the sub-channel code. Here, we only discuss the turbulent mixing model. In MATRA, the turbulent mixing effect is taken into account in the momentum equation and the energy equation. The general form of the turbulent mixing flow rate is expressed by the equation from Stewart et al. (1977):

$$\omega' = \beta S_{ij} G_{ij} \tag{5.9}$$

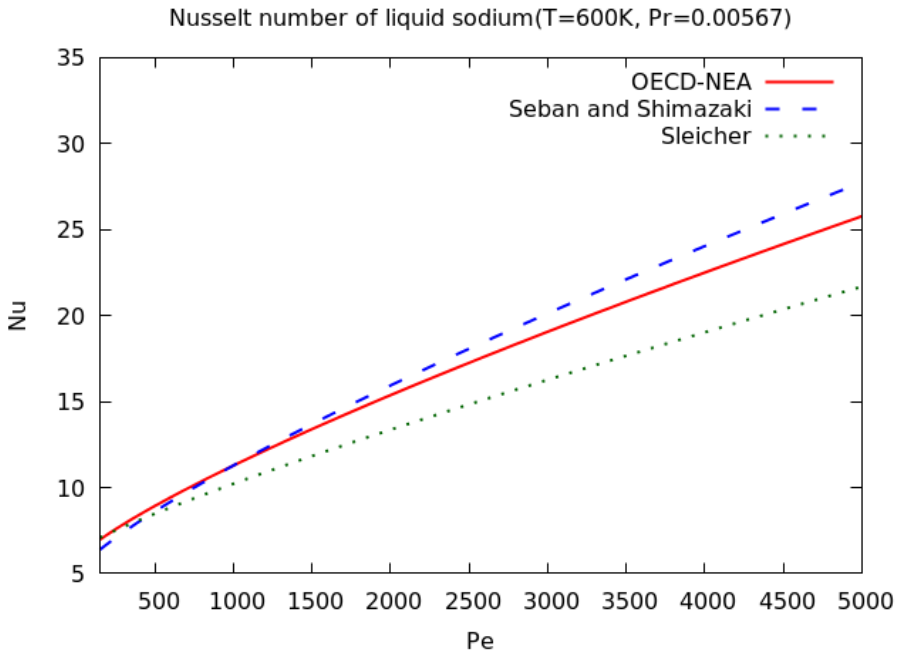

Figure 5.2.: Nusselt number of liquid sodium varying with Pe number

where S_{ij} is the width of the gap between two sub-channels, and G_{ij} is the mean mass flow rate of sub-channel i and j.

The turbulent mixing coefficient β is very important in the turbulent mixing model. Cheng and Tak (2006) proposed a correlation based on CFD simulation results of an LBE cooled fuel assembly.

$$\beta = 0.2c \cdot Re^{-0.125} \tag{5.10}$$

The coefficient c depends mainly on the sub-channel geometry, and also increases slightly with increasing Reynolds number [Cheng and Tak (2006)]. This model is used to calculate the turbulent mixing coefficient in the present study.

5.1.5. Local heat transfer model

In the present study, the new proposed local heat transfer correlation Eqn. 4.109 is implemented into the MATRA code for the detailed rod circumferential heat transfer output. This improvement provides the output of the local heat transfer coefficient distribution and the local cladding outer surface temperature distribution.

5.2. Applications of MATRA code

After the modification of the MATRA code, a benchmark test is selected to validate the code. Then the code MATRA is applied to simulate both ASTRID and new ASTRID fuel assembly designs.

5.2.1. ORNL 19-rod benchmark test

A sodium cooled 19 rod bundle experiment was performed by Oak Ridge National Laboratory as introduced in the literature from Fontana et al. (1974). The fuel rods are simulated by electric heaters, that have the same configuration as in a real SFR, including spacers, volume heat source. The experiment was carried out in the fuel failure mock up sodium loop. The test section is shown as Figure 5.3.

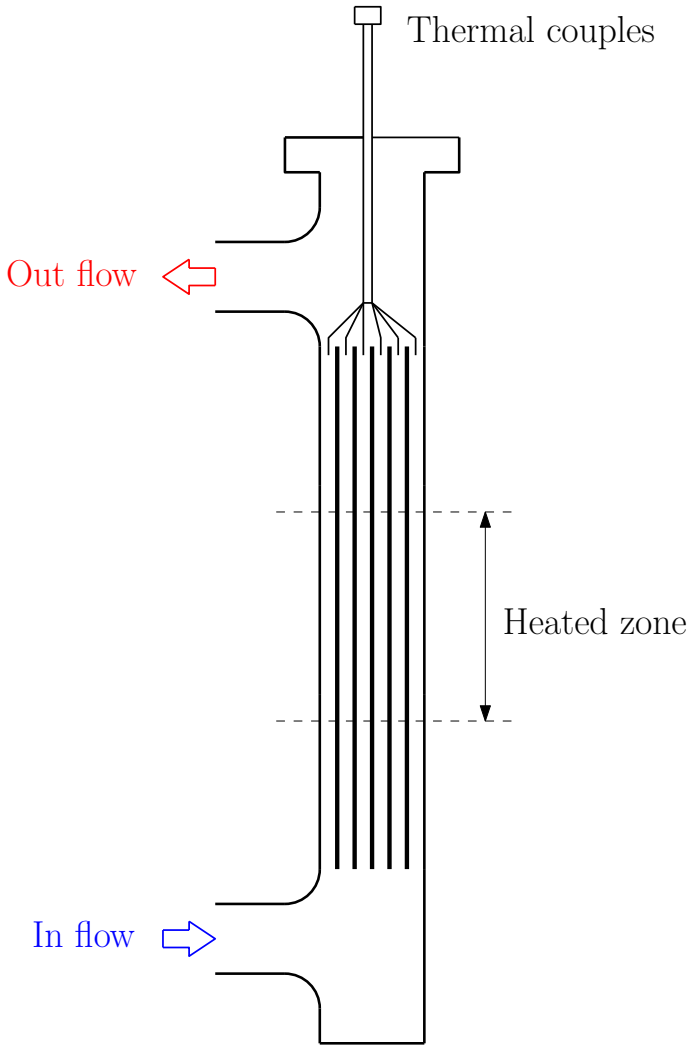

Figure 5.3.: ORNL FFM test section for rod bundle 2A [Fontana et al. (1974)]

Rod bundle 2A of ORNL 19-rod test is simulated in the present study to validate the modified MATRA code. The heated length of the rod bundle is 53.34 *cm*, while the total length is 101.6 *cm*. The detailed geometry data and operating conditions are illustrated in Table 5.2 and Table 5.4.

The geometry data shows that the heating length is about 1.5 times of the helical wire pitch. Comparing with geometry data of ASTRID used in previous chapters, the diameter of rod bundle 2A is much smaller. The P/D ratio of rod bundle 2A is relatively bigger.

A series of test runs were carried out for the ORNL 19-rod experiment. The test case run 103 with high mass flow and power is selected as a benchmark case for validation of the modified MATRIA code in the present study.

The boundary condition of the benchmark test is given as Table 5.4. The system operates under the atmospheric pressure. The inlet temperature and mass flow rate are given. The mass flow rate is transformed into mass flux for the MATRA input. The rod power is transformed into the wall heat flux. The boundary conditions are given into the MATRA input deck.

The experimental result of run 103 is shown as Table 5.5. The channel ID refers to the numbering scheme in Fig. 5.4. The sub-channels measured in the benchmark test are selected typical channels, including interior channel, wall channel and corner channel.

Table 5.2.: Geometry of rod bundle 2A [Fontana et al. (1974)]

Geometry data	Value	Unit
Rod diameter	5.842	mm
P/D ratio	1.243	-
Wire diameter	1.422	mm
Wire wrap pitch	304.8	mm
Total length	1016.0	mm
Heating length	533.4	mm

Table 5.3.: Experimental condition of test case run 103 by Fontana et al. (1974)

Run ID	Inlet temperature	Flow rate	Power	Heater
run 103	315.56 °C	3.41 $\times 10^{-3} m^3/s$	19.69 $kW/m/rod$	all

The normalized exit temperature profiles of the sub-channels are given. The definition of normalized temperature is:

$$T^* = \frac{T_{out,sub} - T_{in}}{T_{out,ave} - T_{in}} \tag{5.11}$$

where $T_{out,sub}$ is the outlet temperature of one sub-channel, and T_{in} is the inlet temperature. $T_{out,ave}$ is the mass flow rate weighted average outlet temperature of the 19-rod bundle.

In the MATRA code, the numbering of sub-channels and rods is very important. The information of the neighbour channels has to be given to each sub-channel. The numbering schematic of the input deck used in the present study for rod bundle 2A is shown in figure 5.4. The numbering is divided into two parts: the numbering of the rods and the numbering of the sub-channels. The numbers are defined by the user, and the neighbouring relationships must be specified. For example, the users need to input the surrounding sub-channels IDs for each fuel rod. Each of the sub-channel also requires its neighbouring sub-channel IDs. In the numbering scheme, the central rod is numbered 1, and the outer ring rods are numbered sequentially in clockwise direction. The sub-channels are also numbered ring by ring in clockwise direction. After numbering the wall channels, the corner channels are numbered at last.

In the nodalization, the rods and sub-channels are divided into 70 control volumes in the axial direction. The geometry information of the wire spacers is also given as the input of MATRA code. The MATRA code works like a 2D code, one dimension is the axial position, and another dimension is the numbering of the sub-channel connections.

Both the experimental result and simulation result follow the same numbering scheme shown as figure 5.4. The exit temperature of different types of sub-channels are compared with the experimental data. The simulation reports the mass flow rate weighted average outlet temperature to be 366.09 °C. The calculated normalized temperatures are shown in figure 5.5.

As shown in figure 5.5, the simulation result roughly agrees with the experimental result. The calculation result of wall channel 32 and its adjacent channel 18 is higher than the test data. While, the calculated temperatures of the central channels 1 and 4 are relatively lower than the experimental results. The calculated interior region temperature is relatively lower than the experimental data, but the calculated outer region temperature is relatively higher than the experimental data. The explanation of the difference is that the MATRA

Table 5.4.: Operating condition of rod bundle 2A simulation [Fontana et al. (1974)]

Operation data	Value	Unit
System pressure	10132.0	Pa
Inlet temperature	315.56	°C
Inlet mass flux	6072.31	$kg/m^2/s$
Average rod heat flux	1073.1	kW/m^2
Axial power distribution	Uniform	-
Radial power distribution	Uniform	-

Table 5.5.: Experimental result of test case run 103 by Fontana et al. (1974)

Channel ID	Exit temperature [°C]	Temperature rise [°C]	Normalized temperature
4	378.83	63.27	1.269
17	374.39	58.83	1.180
18	360.39	44.83	0.899
32	357.50	41.94	0.840
41	360.72	45,16	0.906
1	378.89	63.33	1.271
9	368.94	53.38	1.071
38	356.61	41.05	0.824

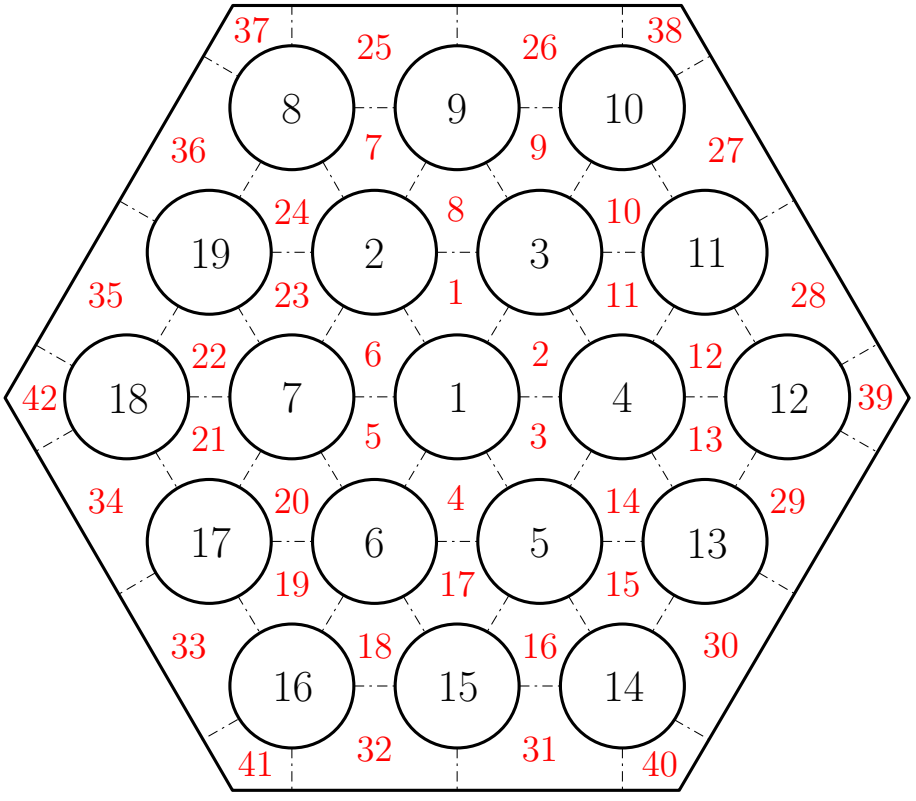

Figure 5.4.: Numbering schematic for rod bundle 2A

code overestimate the inter-channel mixing, then the exit temperature distribution is more flat. Further investigation of the discrepancy is suggested as a future work.

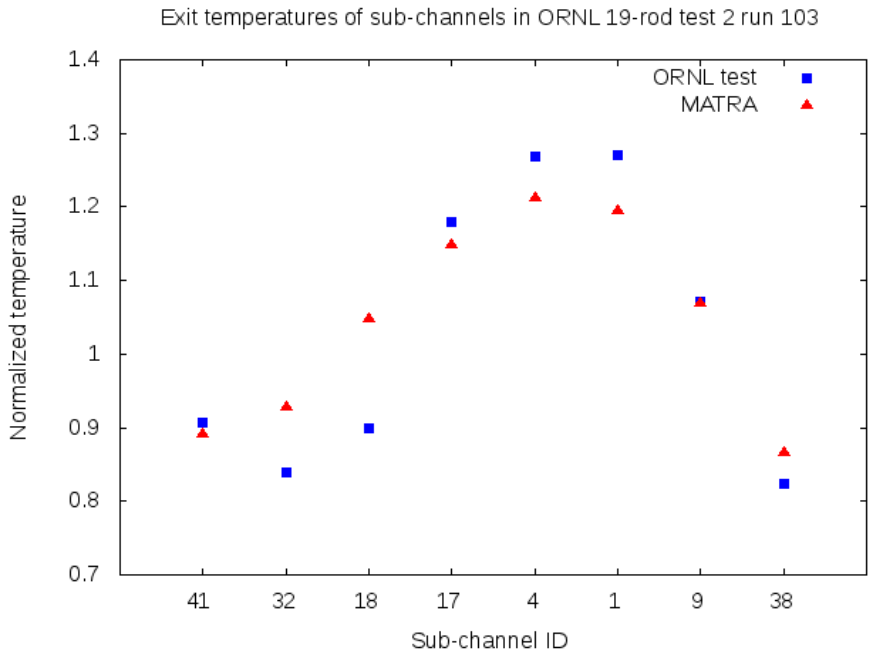

Figure 5.5.: Exit temperatures of ORNL 19-rod test 2 run 103

With the code of MATRA, it is also possible to calculate the diversion cross flow over the gap between adjacent channels. As illustrated in figure 5.6, the cross flow rate is calculated by MATRA for ORNL 19-rod test 2 run 103 case. The gap (1, 2) is a typical gap between central channels. The effect from the wall is very small here. Gap (18, 32) is a typical gap between wall channel and central channel, and gap (32, 41) is a gap between wall channel and corner channel.

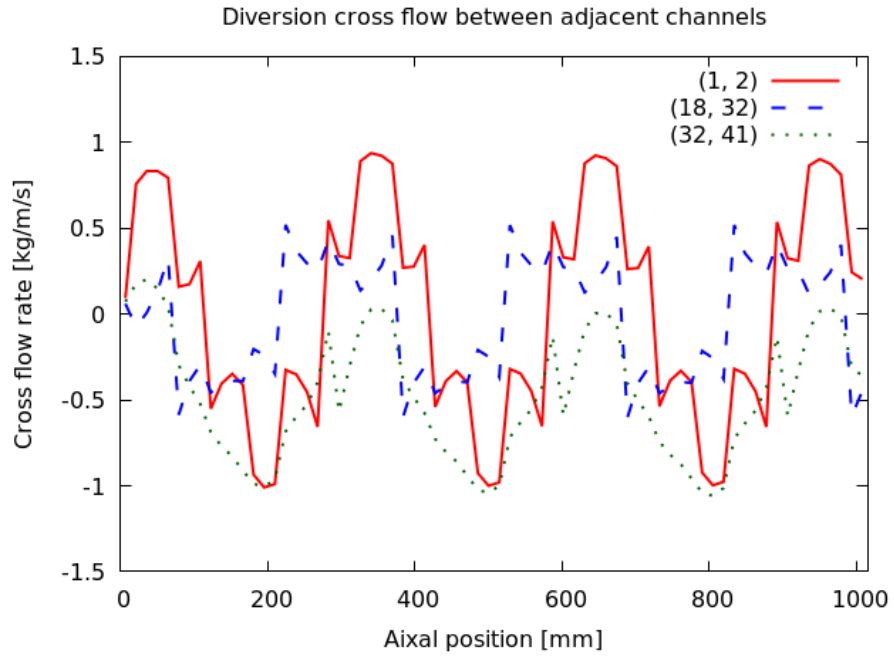

Figure 5.6.: Diversion cross flow between adjacent channels

Fig. 5.6 shows a periodical distribution for gap between central channels. The cross

flow over the gap between central channel and wall channel is also a cosine like shape, but the amplitude is smaller. For the gap between wall channel and corner channel, the cross flow direction doesn't change, it is the same to the wire rotation direction. In the present study, the proposed sweeping flow model in chapter 3 is not implemented into the MATRA code, this is because of the fundamental numerical scheme and code structure of MATRA. In MATRA, the pressure calculation is coupled with the momentum calculation, and the diversion flow is determined by the distribution of the cross flow resistance factor induced by the wire spacers. The sweeping flow correlation proposed in present study is a deterministic function of geometry parameters. The improvement of MATRA code with the new proposed sweeping flow model is a future work.

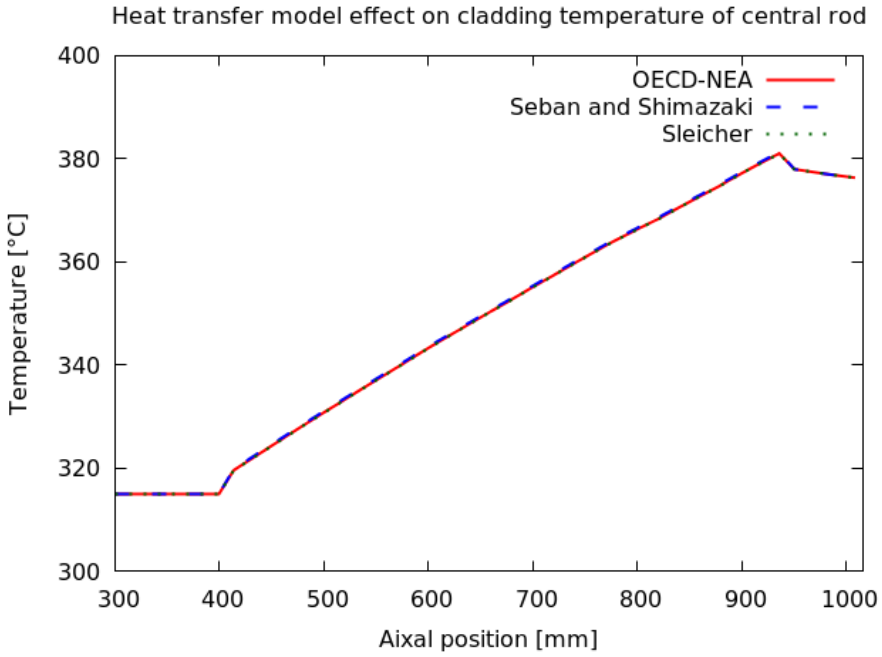

Figure 5.7.: Heat transfer model effect on cladding temperature of central rod

As shown in Fig. 5.7, the sensitivity of heat transfer model's effect on the cladding temperature is studied. Three different heat transfer correlations are select to simulate the ORNL 19-rod test 2 run 103 case. The result shows that the effect of heat transfer model on the cladding temperature is very small. This is because of the small cladding to coolant temperature difference. Although the discrepancy of the heat transfer coefficient can be up to 20 %, the effect on the cladding temperature difference is less than 0.6 $°C$. Compared with the cladding temperature rise in the axial direction, the temperature difference with the 3 different heat transfer correlations is very small. The Sleicher et al. (1973) which was recommended by Cheng et al. (2004) is selected as the heat transfer model for further applications.

5.2.2. Sub-channel analysis of ASTRID fuel assembly

After finishing the validation of the modified MATRA code for the sodium cooled bundle, a preliminary analysis was carried out for the ASTRID fuel assembly. The fuel assembly of ATSTRID core is studied with two different approaches, the first approach is modeling of a 1/12 fuel assembly with a symmetrical assumption, and the second one is a model for a complete fuel assembly.

The geometry data of the ASTRID fuel assembly is shown as Table 5.6. In the design

of ASTRID, the number of fuel pins in one fuel assembly is 217. The geometry data is exactly the same as the base case of rod bundle in previous chapters.

Table 5.6.: Geometry of the ASTRID fuel assembly

Geometry data	Value	Unit
Rod diameter	9.7	mm
P/D ratio	1.113	-
Wire diameter	1.0	mm
Wire wrap pitch	180.0	mm
Total length	2136.0	mm
Heating length	850.0	mm
Rod number	217	-
Cladding thickness	0.5	mm
Wrapper tube inner distance	161.5	mm

It is assumed that the temperature distribution of the hexagonal fuel assembly is symmetrical as its geometry. Only 1/12 fuel assembly is simulated with MATRA. The operation condition is given as Table 5.7.

Table 5.7.: Operating condition of ASTRID fuel assembly simulation

Operation data	Value	Unit
System pressure	10132.0	Pa
Inlet temperature	385.0	°C
Inlet mass flux	6470.98	$kg/m^2/s$
Average rod heat flux	596.30	kW/m^2
Axial power distribution	Uniform	-
Radial power distribution	Uniform	-

Within the first numerical approach, the sub-channel numbering scheme is illustrated in figure 5.8. Only 1/12 fuel assembly is simulated, the numbering is from the center ring to the outer rings. The wire spacers are not included in this model, because of the symmetrical assumption.

In the present study, only the heated part of the fuel assembly is simulated. The length is about 850 mm and the sub-channel model is divided into 100 control volumes in the axial direction. The exit temperatures of several typical sub-channels are illustrated in figure 5.9. It is easy to see, the sub-channels close to the center has a higher temperature than the outer wall channel or the corner channels. The mass flux in the wall channel is bigger than the central channel, while the mass flux of the corner channel is less than the central channel. It is because of the hydraulic diameter effect on the flow resistance.

The cladding temperature is shown as Fig. 5.10. The cladding temperature increases in the axial direction. The closer to the center, the higher the cladding temperature. So, the central channel temperature is higher than the wall channel and the corner channel. In this simulation, the Rheme model is used to calculate the pressure drop, and the Sleicher model is used for the heat transfer, and the Cheng model is used for the turbulent mixing.

The second numerical approach is the simulation of a complete fuel assembly instead of a portion of it with symmetrical boundaries. The physical models used in the this simulation is identical to the first one. The only additional model used in the complete fuel assembly

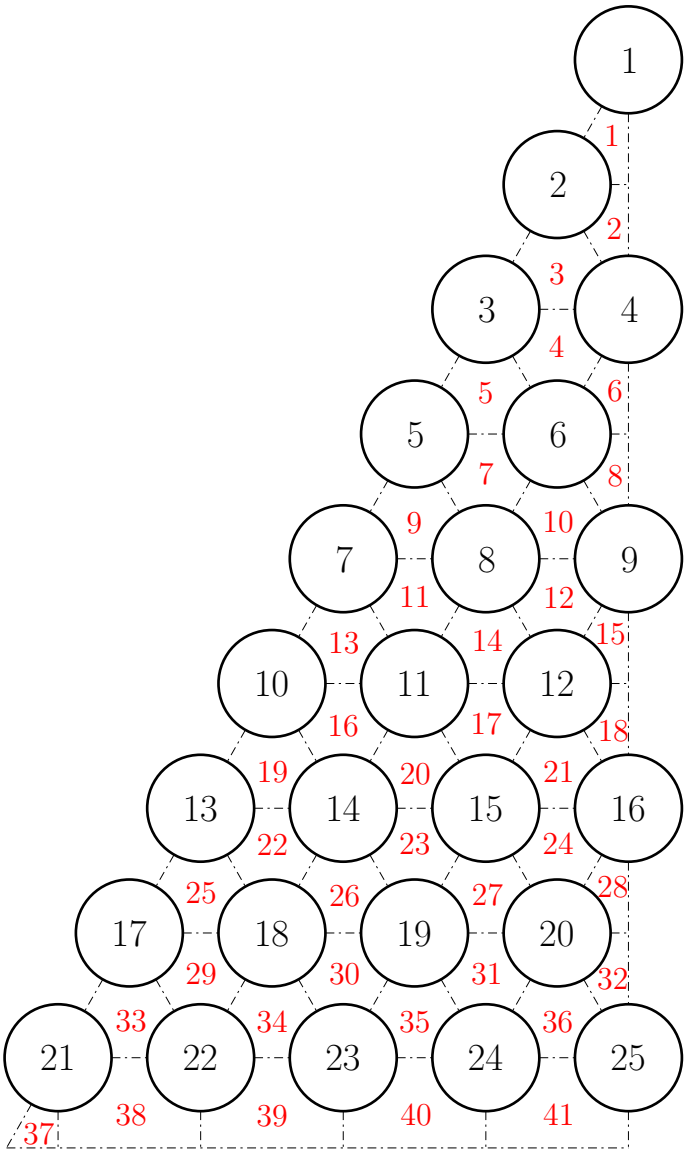

Figure 5.8.: Numbering schematic for 1/12 ASTRID fuel assembly

simulation is the wire spacer model. A new subroutine is created for automatic input deck generation. The inputs of the new subroutine mainly includes:

1. The number of rings
2. Rod pitch and diameter
3. Wire pitch
4. Wire position at inlet

The output of the new subroutine is a complete input deck of MATRA. The input deck generated with the new subroutine includes the following information:

1. Neighbour channel ID list for each channel
2. Contacted channel ID list for each rod
3. Geometry information
4. Angle between wire and each gap
5. Wire wrap inventory

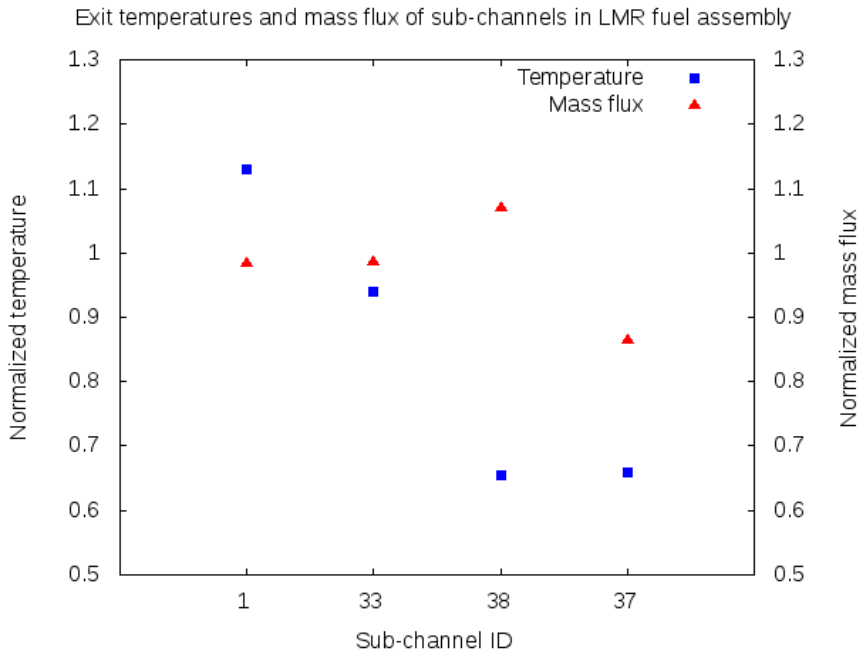

Figure 5.9.: Exit temperatures and mass flux of sub-channels in ASTRID fuel assembly

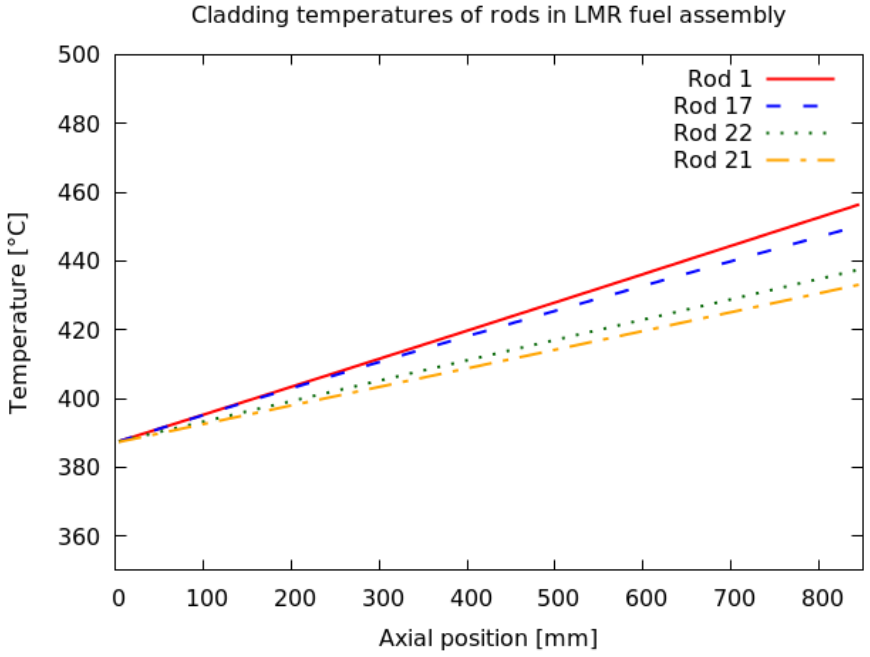

Figure 5.10.: Cladding temperatures of rods in ASTRID fuel assembly

The MATRA input deck for the 217-pin fuel assembly is used for the sub-channel analysis with the above user input.

The definition of the wire position at the inlet panel is given as the two angles which are shown in Fig. 5.11. As each gap is connected with two rods, and each rod is wrapped with a wire spacer. At the inlet cross section of the fuel assembly, the relative angles between the two wire centers and the gap should be given. All the wire to gap relative angles are also generated automatically with the new subroutine.

The numbering of the complete fuel assembly is shown in Fig. 5.12. The numbering

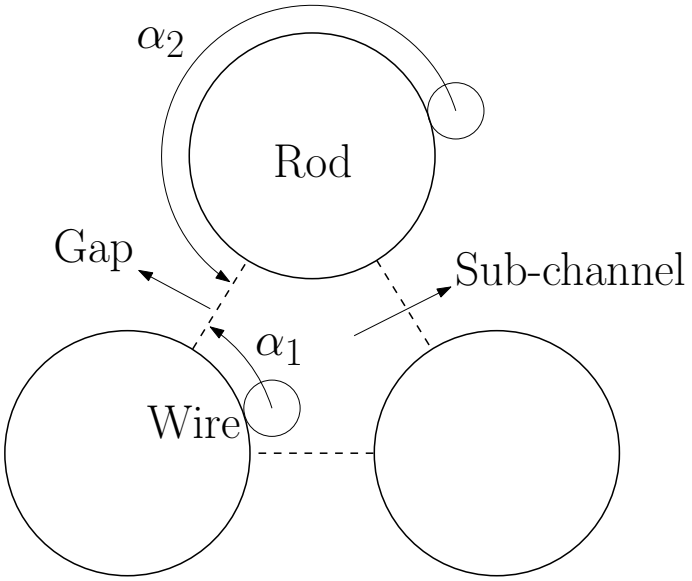

Figure 5.11.: The wire crossing angle at the inlet panel

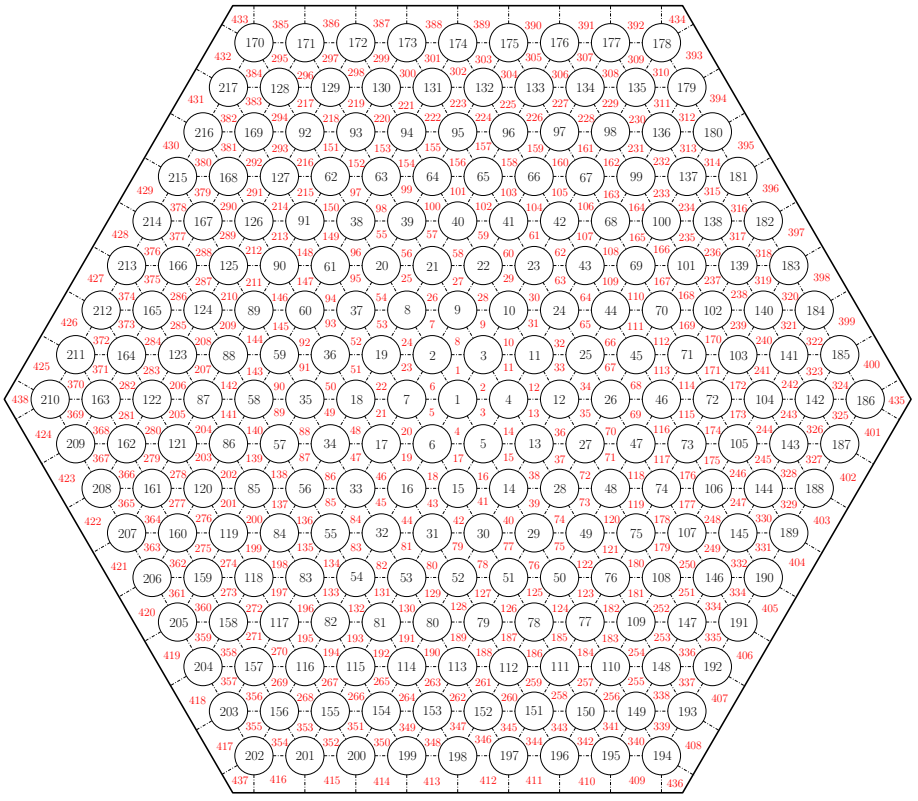

Figure 5.12.: Numbering of a complete fuel assembly of ASTRID

sequence of the rods is from the central rod to the outer rods. It is numbered in the clockwise direction. For the sub-channels, the numbers are also given ring by ring in the clockwise direction. While the central channels are numbered firstly, then are the wall channels, and the corner channels are given their numbers at last. Besides the rods and the sub-channels, the gaps between the rods are also numbered, which are not shown in the figure. The numbering and neighbour searching are processed automatically with the modified code. The neighbouring relationships between sub-channels, rods, and gaps are foundation of the initialization of the linear equation group.

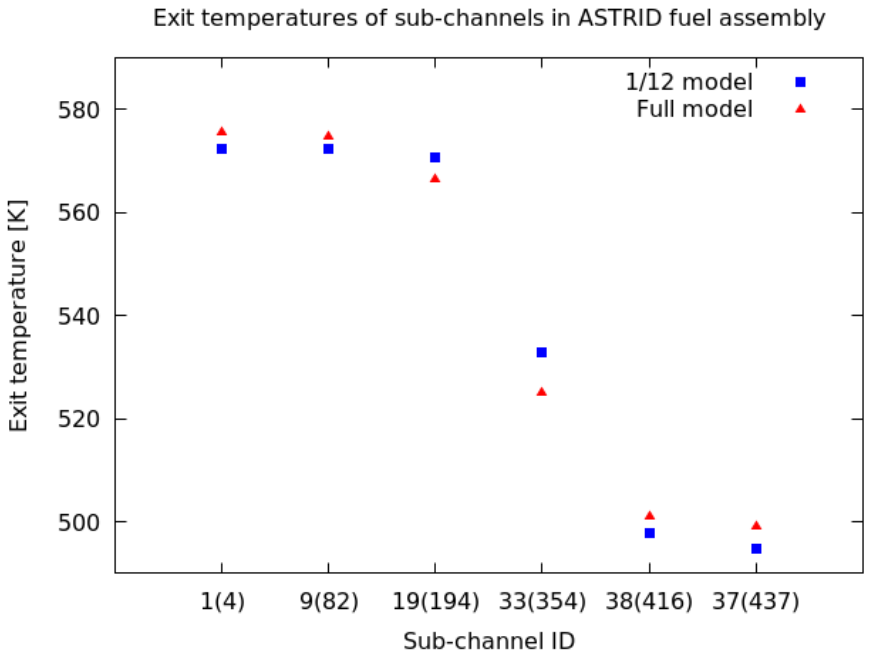

Figure 5.13.: Exit temperatures at sub-channel outlets

In Fig. 5.13, the full model for the ASTRID fuel assembly gives a higher temperature for the channels in the central region and the outer wall region. But the temperature calculated with the full model is lower than the 1/12 model in the middle region between the assembly center and the hex wrapper. The temperature difference is not obvious between the two models. The temperature distribution is also related to the mass flux distribution.

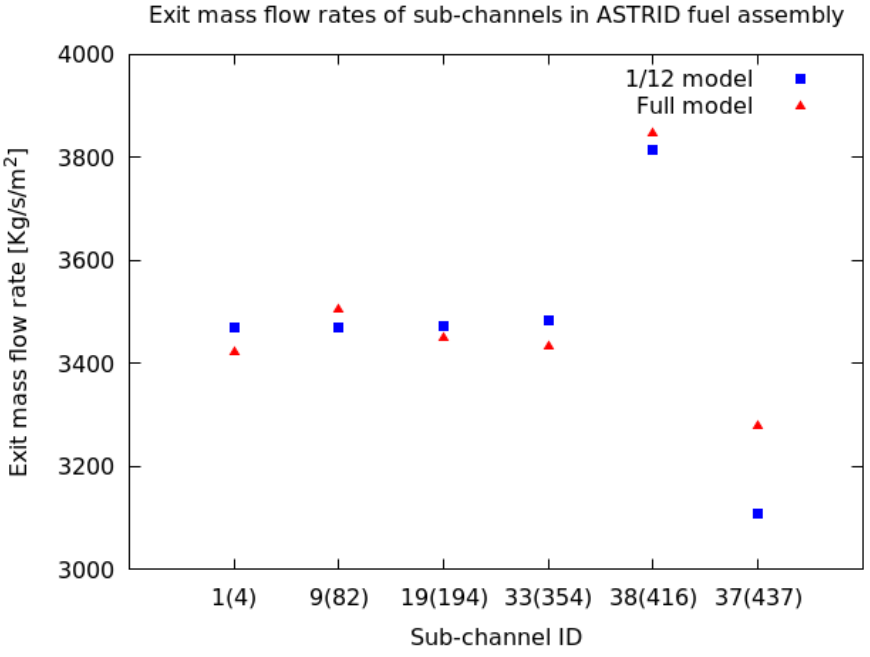

Figure 5.14.: Exit mass flux at sub-channel outlets

As shown in Fig. 5.14. The exit mass flow rate calculated with the full model is also different from the 1/12 model. The channel 38(416) is a wall channel, which has a bigger

flow area. The channel 37(437) is a corner channel, which has a minimum flow area. This is mainly caused by the hydraulic diameter of the sub-channel. The hydraulic diameter of wall channel is bigger, then it results a smaller flow resistance. The mass flow rate of the wall channel and the corner channel calculated with the full model is bigger than the 1/12 model, it is because of the effect of the wire spacers on the inter-channel momentum exchange.

The cladding temperature and the coolant temperature show almost a linear distribution. The temperature difference between the cladding surface and the coolant is very small. This is because of the high thermal conductivity and heat transfer coefficient of the liquid sodium.

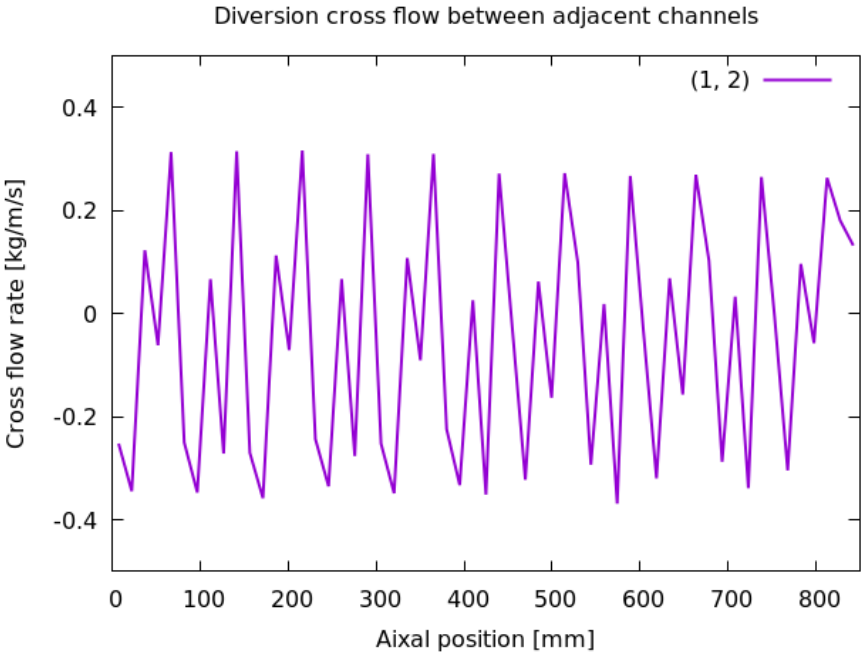

Figure 5.15.: Diversion cross flow between sub-channel 1 and 2

Shown as Fig. 5.15, the diversion cross flow between two sub-channels is a periodical distribution, which is similar to the sweeping flow model proposed in the present study. Because of the limitation of the MATRA code, the node refinement in the axial direction of the complete fuel assembly has an upper limit. So the curve of the cross flow rate is not smooth.

5.2.3. Fuel assembly sensitive study for New ASTRID core

Limited by the function of the modified MATRA code, it is not possible to simulate a complete SFR core including the inter-wrap flow. An alternative solution proposed in the present study is to carry out a sensitivity analysis of the fuel assembly for the entire core of the New ASTRID. Several fuel assemblies at the typical core locations are selected for this analysis.

The geometry of core and fuel assembly

The New ASTRID is a smaller scale reactor for integral validation. The thermal power of New ASTRID is about 400 $MWth$. In comparison, the thermal power of ASTRID is about 600 $MWth$. A big modification is the geometry of the rod bundle, the pin diameter of the New ASTRID is smaller, while the P/D ratio is bigger than the old ASTRID design.

For the New ASTRID, the number of fuel pins is increased from 217 to 271. The geometry data of the New ASTRID sub-assembly is given as Table 5.8.

Table 5.8.: Geometry of the New ASTRID fuel assembly [Gerschenfeld (2018)]

Geometry data	Value	Unit
Height	4	m
External inter-flat distance	17.3	cm
Hexcan thickness	4.6	mm
Lower FP plenum height	90	cm
Core height	160	cm
Upper FP plenum height	19	cm
Sodium plenum height	28	cm
Convergent region height	12	cm
Upper neutron shield diameter	10	cm
Number of pin rings	9	
Number of pins	271	
Pin diameter	8.5	mm
Pin pitch	9.8	mm
P/D	1.15	
Cladding thickness	0.565	mm
Wire wrapper diameter	1.2	mm
Wire wrapper pitch	18	cm

In the present study, the control rod sub-assembly is assumed as an empty hex-can. The 6 rings of reflector sub-assemblies are not considered. The simulated fuel assemblies are only located in the inner core region. With the geometry of the new ASTRID core, the MATRA input deck is generated. Then the boundary condition is imposed.

Boundary conditions of fuel assembly

In the present study, the nominal state of New ASTRID is studied. The boundary conditions of nominal state are given as below [Gerschenfeld (2018)]. The boundary conditions include inlet temperature, outlet temperature, mass flow rate, core power distribution.

The core inlet outlet temperatures:

$$T_{in} = 400\,^{\circ}\mathrm{C} \tag{5.12}$$

$$T_{out} = 550\,^{\circ}\mathrm{C} \tag{5.13}$$

The core mass flow rate:

$$Q_{core} = 2100\,kg/s \tag{5.14}$$

Over the 5 rings of fuel assemblies, the flow rate is considered uniform for the 82 sub-assemblies. The power distribution is assumed as a chopped cosine function.

$$Q = 24.24\,kg/s \tag{5.15}$$

$$P_{neut} \propto \cos\frac{\pi}{3}\frac{z - H_{mean}}{\Delta H_{core}/2}\cos\frac{\pi}{3}\frac{\sqrt{x^2+y^2}}{R_{core}} \tag{5.16}$$

where $R_{core} = 1\,m$.

The total flow area of the cross section of the fuel assembly is 0.008876 m^2, and the inlet mass flux at the nominal condition is 2731.077 $kg/s/m^2$. The total thermal power is 400 MW, and the average wall heat flux of the fuel rod is 421.30 kW/m^2. These are data with a transformed format for MATRA input.

$$\int_0^{\frac{\pi}{3}} \cos^2\theta d\theta = \left(\frac{\theta}{2} + \frac{\sin 2\theta}{4}\right)\Big|_0^{\frac{\pi}{3}} = \frac{\pi}{6} \tag{5.17}$$

The maximum wall heat flux of the rod surface is 804.62 kW/m^2. In the MATRA code, the non-uniform power distribution is inputted by the local to maximum power ratio. The power distribution in the fuel assembly is not symmetrical, except the central fuel assembly of the core. The power ratio of each rod at a specified position is retrieved from the chopped cosine like core power distribution shape.

Numbering scheme of fuel assembly

The numbering scheme of a complete fuel assembly model for the New ASTRID is shown in Fig. 5.16. Some calculated geometric parameters given to the input deck are listed

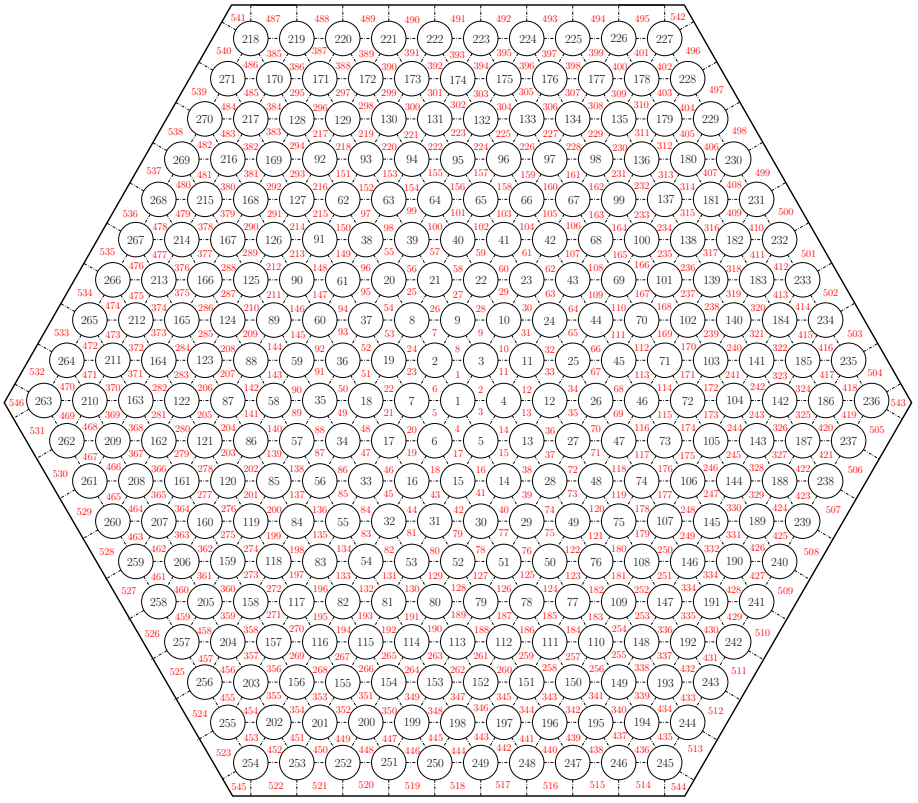

Figure 5.16.: Numbering of a complete fuel assembly of New ASTRID

as Table 5.9. It includes the flow area, wetted perimeter, heated perimeter for different sub-channel types.

The distance between the centroids of the neighboring sub-channels, for example inner channel to inner channel, is calculated by the distance between the geometry centers of the two nearby sub-channels. The information of the channel distance is given as Table 5.10.

Besides that, the wire position angle at the inlet panel, the power ratio distribution and the axial node numbers are also given as input of MATRA. In the axial direction of the fuel assembly model, the sub-channel is divided into 57 nodes.

Table 5.9.: Geometric parameters of sub-channels for the New ASTRID

Geometry data [mm]	Inner channel	Wall channel	Corner channel
Flow area	13.215	26.018	8.327
Wetted perimeter	13.352	23.152	10.860
Heated perimeter	13.352	13.352	4.451

Table 5.10.: The centroid distance between neighbouring sub-channels

	Centroid distance
Inner-inner	5.658
Inner-wall	6.492
Wall-corner	6.492
Wall-wall	9.8

Calculation matrix for sensitivity study

To analyze the thermal-hydraulics of the reactor core of New ASTRID, several typical fuel assemblies are selected for the sensitivity study. The reactor inner core has 5 rings, including 82 fuel assemblies and 9 control rod fuel assemblies. The power distribution and mass flow rate are given in the boundary conditions. As shown in Fig. 5.17, 5 different fuel assemblies are selected for the sensitivity study. F01 is the central fuel assembly, FA04 is one of the fuel assemblies on the edge of the core, and FA05 is the fuel assembly at the corner of the core. F02 and F03 are in the middle between FA01 and FA04. The internal power distribution of the fuel assembly depends on its position in the core, which follows Eqn. 5.16. The power distribution of FA01 is symmetrical, the power of other fuel assemblies are non-symmetrical. The fuel assembly more closer to the center of the core, the higher the power it is. In one fuel assembly, the fuel rods which are more closer to the core center, have a higher power. The boundary conditions of the selected fuel assemblies are given as Table 5.11.

Table 5.11.: The position and power of the fuel assemblies

ID of FA	Distance to core center [cm]	Power ratio	flow rate [kg/s]
FA01	0.0	100%	24.24
FA02	31.0	94.8%	24.24
FA03	62.0	79.7%	24.24
FA04	78.0	68.5%	24.24
FA05	89.5	59.2%	24.24

The power ratio is the ratio of the maximum wall heat flux of one fuel assembly center to the core center. The rod power depends on its location in the core. The power also varies in the axial direction and is described as a chopped cosine function. As Fig. 5.18, the wall heat flux of the central rods of the 5 typical fuel assemblies are given. FA01 is the central fuel assembly, and its central rod reaches a peak wall heat flux of 804.62 kW/m^2. The central rods of the other fuel assemblies also have a cosine like power distribution in the axial direction, while the amplitude depends on the distance to the core center. F04 is a wall fuel assembly, and the FA05 is at the corner of the core. The distance from FA05 to the core center is largest, so the power of FA05 is lowest.

In the sensitivity study of the typical fuel assemblies, two important assumptions are

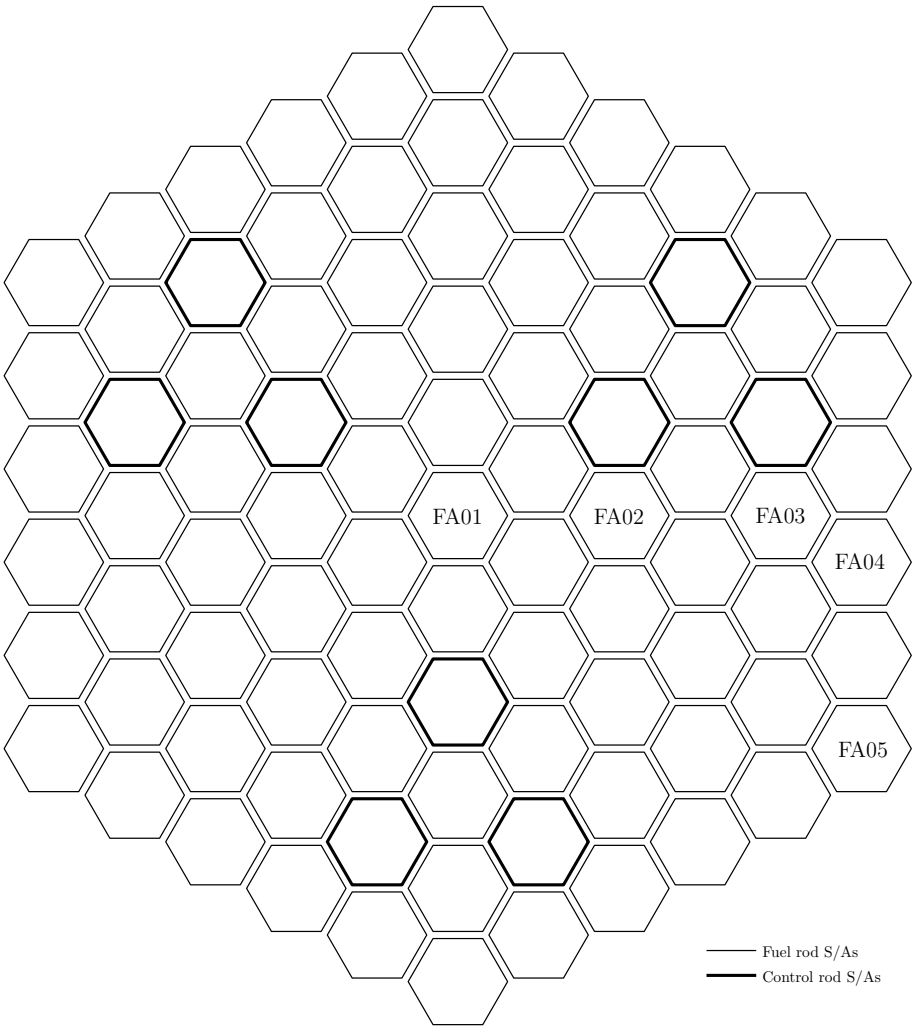

Figure 5.17.: Core geometry of New ASTRID

applied:

1. The inter-wrapper flow is not considered
2. The wall of the wrapper is adiabatic boundary

This is because of the limitation of the function of MATRA code, the inter-wrapper flow can not be simulated. The energy loss through the wrapper is not considered.

Sub-channel approach simulation results

With the code MATRA, the steady state simulations are carried out with the boundary inputs and geometry configuration given in the present study. In the 5 selected fuel assemblies, the main difference is the power distribution. As the central fuel assembly, FA01 has a symmetrical power distribution in radial direction. The other fuel assemblies have non-symmetrical power distribution. A converged result is obtained with the simulation.

As illustrated in Fig. 5.19, the mass flow rate weighted temperature over the cross section of flow passage increases in the axial direction. The inlet temperatures of the fuel assemblies are the same, but the heating power differs from each other. The highest average coolant temperature can be up to 682 °C. The temperature difference between the central fuel assembly outlet and the corner fuel assembly outlet is over 100 °C.

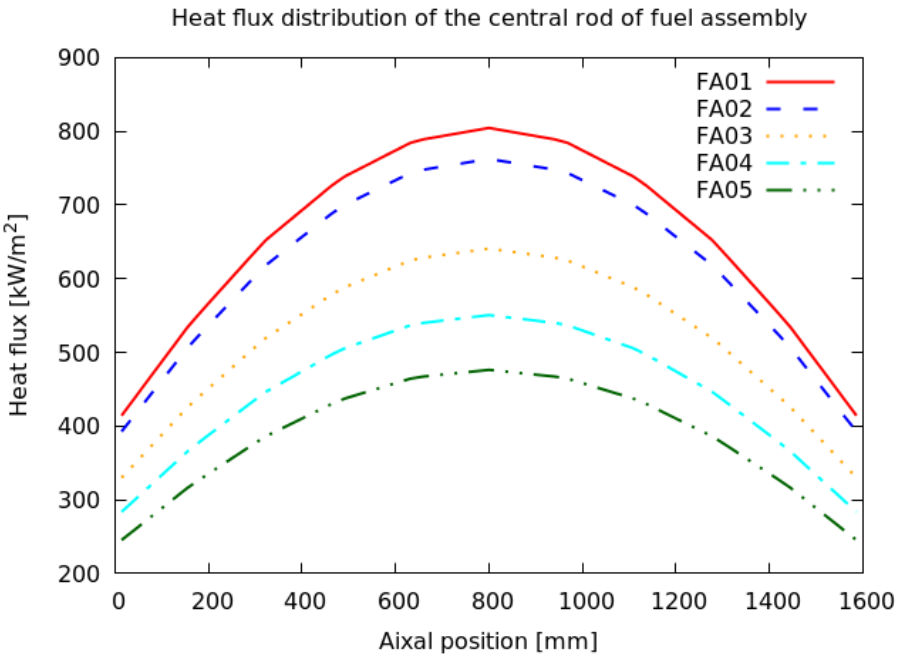

Figure 5.18.: The surface heat flux of the central rod of fuel assembly

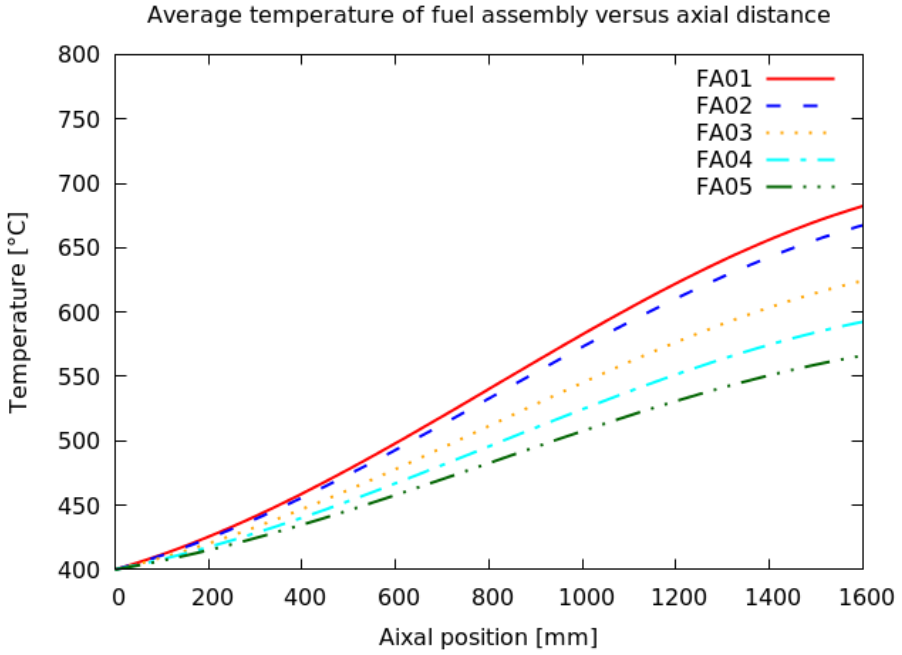

Figure 5.19.: The average coolant temperature of fuel assembly

Fig. 5.20 to Fig. 5.24 give the exit temperatures of the sub-channels of the selected fuel assemblies. Because of the different power of the fuel assembly, the exit temperature is mainly dependent on the power. But the distribution shape varying with the sub-channel position is very similar for each fuel assembly. Sub-channel 1 is a central channel. As the ID increases, it is more close to the outer ring of the fuel assembly. The temperature decreases from the central channel to the outer channel. Sub-channel 509 is a wall channel and 543 is the corner channel. The heating perimeter of the wall channel and corner channel is relatively smaller than the interior channel. On the other hand, the exit temperature is

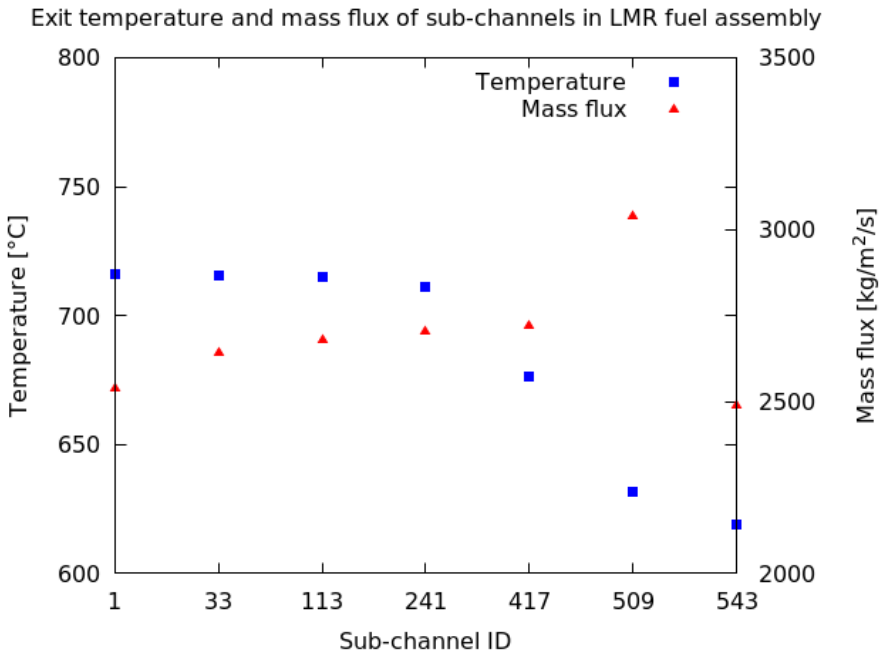

Figure 5.20.: The exit temperature and mass flux of FA01

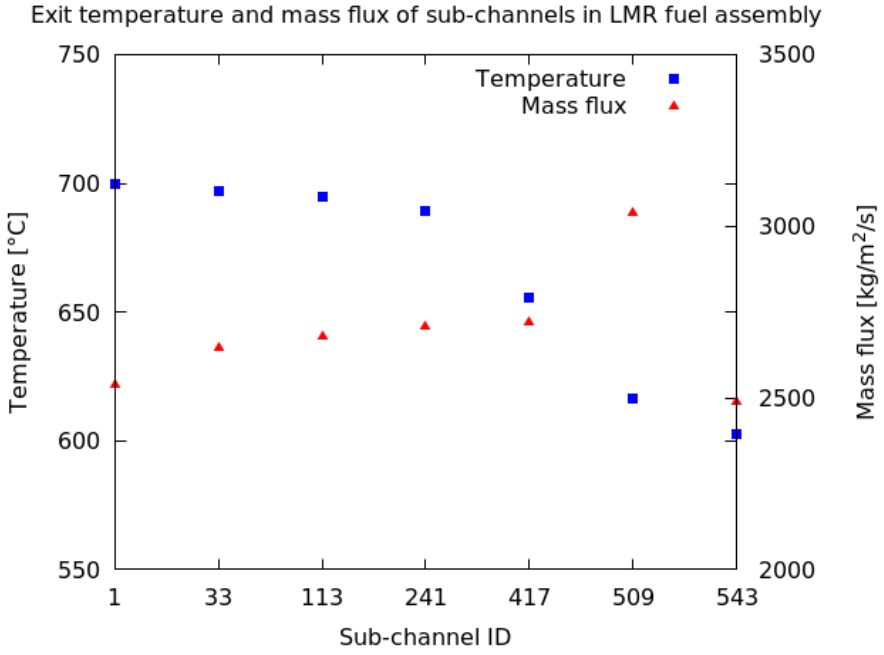

Figure 5.21.: The exit temperature and mass flux of FA02

mainly influenced by the mass flow rate. The mass flux of wall channel is much higher than other channels, and it causes a lower exit temperature. Although the mass flux of the corner channel is low, it is only heated by one fuel rod, so the exit temperature is the lowest. For the corner channel, the heated perimeter is much smaller than the wetted perimeter, because of the adiabatic wall boundary of the hex wrapper. In the 5 fuel assemblies at different locations, the temperature distribution from sub-channel 1 to sub-channel 241 is different from case to case. In FA01, the temperature distribution is more even for the interior channels. For the fuel assembly which is far away from the

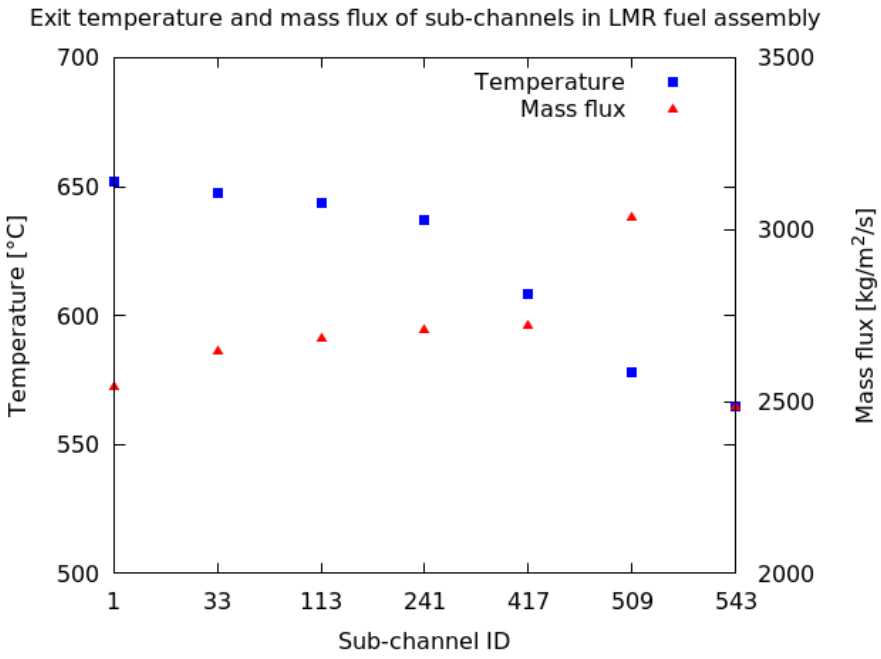

Figure 5.22.: The exit temperature and mass flux of FA03

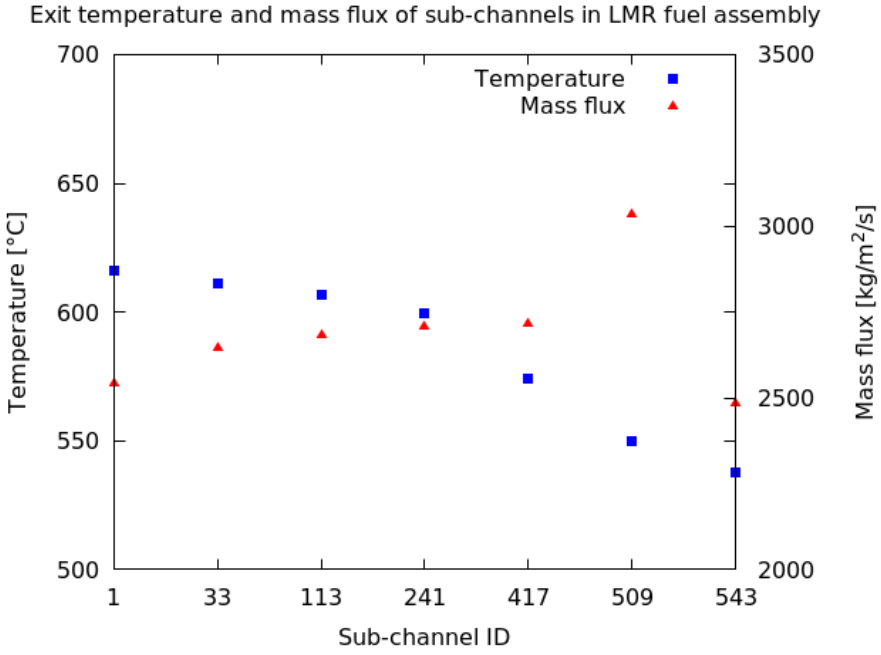

Figure 5.23.: The exit temperature and mass flux of FA04

core center, the temperature distribution is more uneven. The difference of the outlet temperature distribution is caused by the cosine like power distribution of the core. The fuel assembly which is more far away from the core center, the power distribution in radial direction is more uneven. The mass flux distribution of the 5 fuel assemblies are almost identical, this is because of the uniform core inlet mass flux assumption and the same geometry configuration.

As illustrated in Fig. 5.25, the fuel center temperature of the central rod varies in the axial direction. The power of the fuel rod is a cosine distribution, but the bulk temperature

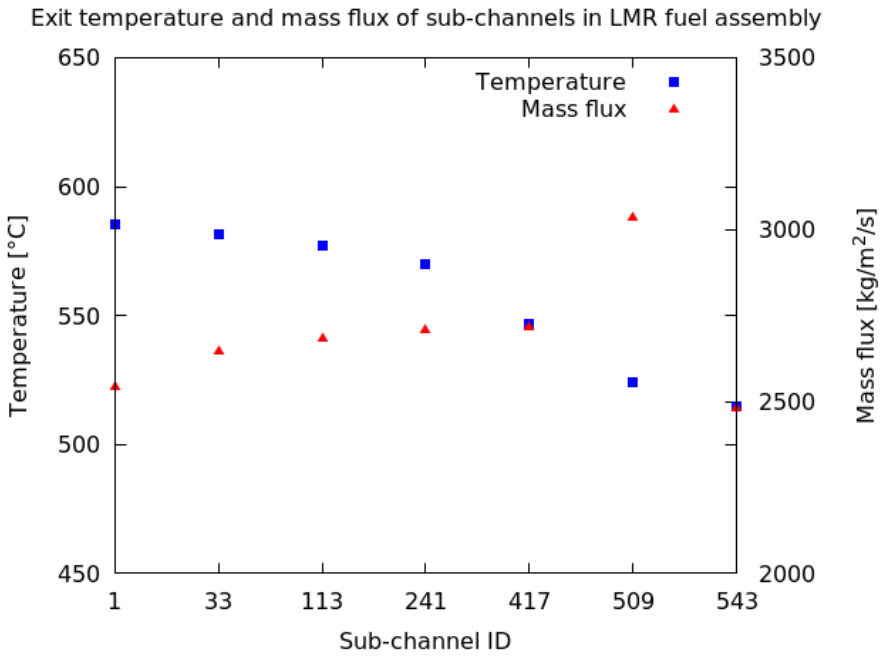

Figure 5.24.: The exit temperature and mass flux of FA05

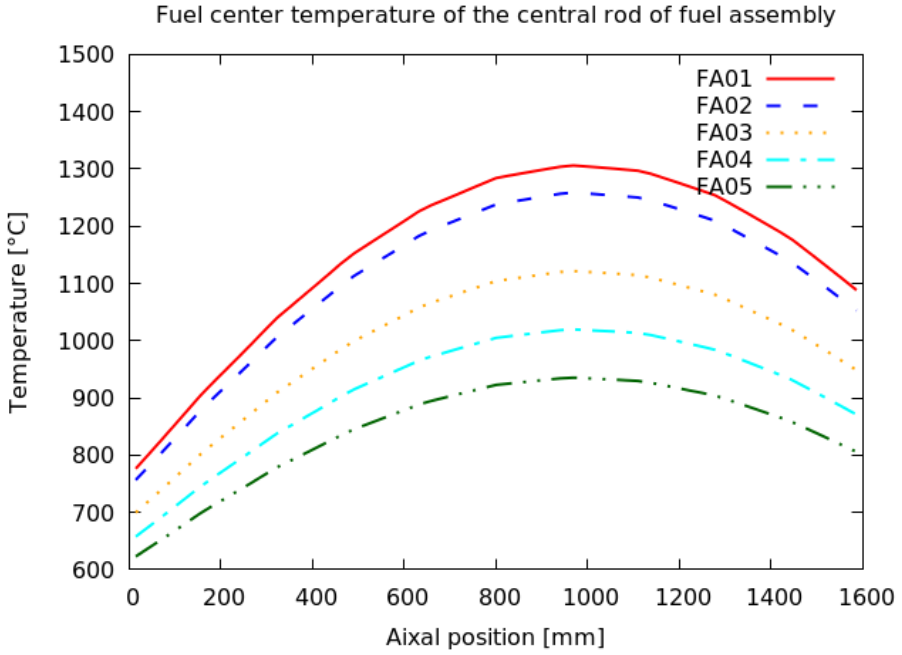

Figure 5.25.: The fuel center temperature of the central rod of fuel assembly

of the coolant rises along the flow channel. So the peak temperature of the fuel is not exactly at the middle position of the fuel rod. The position of the peak temperature is above the middle point. The fuel center temperature at the exit position is higher than the inlet position. The maximum heat flux is at the middle axial position of the core, and the decreasing of the wall heat flux induces a lower cladding temperature. On one hand, the wall heat flux is decreasing, but on the other hand, the bulk coolant temperature is increasing due to the energy accumulation. The higher coolant temperature results in a higher cladding temperature. The distribution shape of the temperature is a combination

of a cosine function and a monotone increasing function.

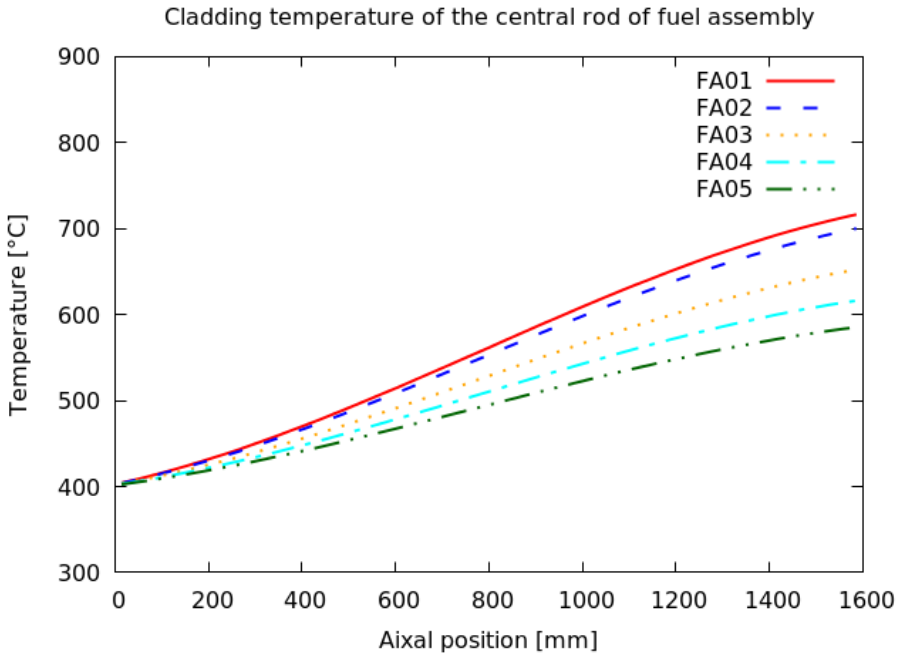

Figure 5.26.: The cladding temperature of the central rod of fuel assembly

In Fig. 5.26 it can be seen that the cladding temperature of the central rod increases along the flow direction. The slope of the temperature curve changes over the axial length. In the middle section, the slope is bigger. This is because of the chopped cosine power distribution in the axial direction. The higher the rod heat flux, the bigger the slope of the curve. The cladding temperature distribution shape is very similar to the average coolant temperature versus the axial distance. The cladding to coolant temperature difference is much smaller than the fuel center to cladding temperature difference.

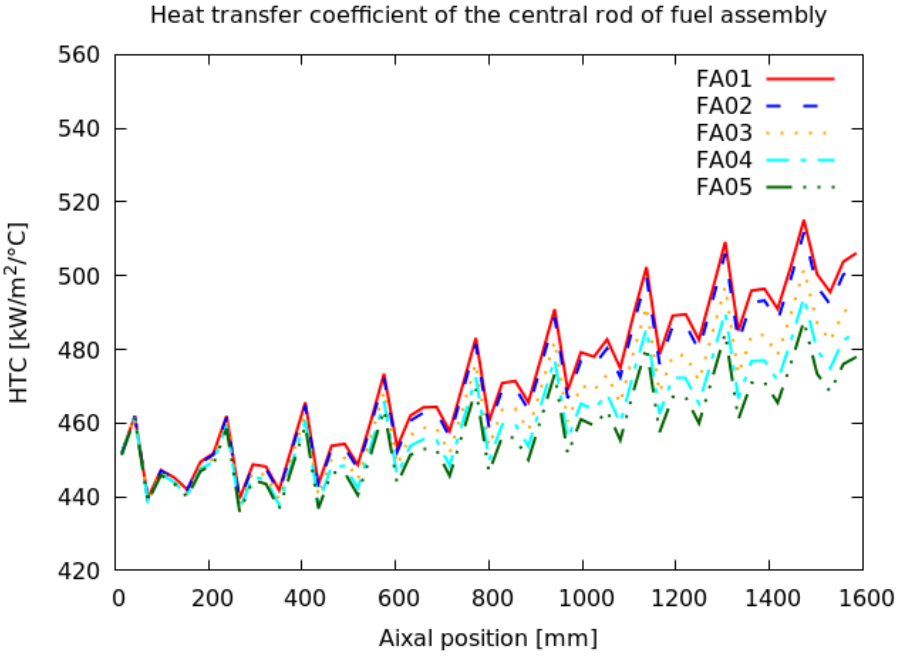

Figure 5.27.: The heat transfer coefficient of the central rod of fuel assembly

Fig. 5.27 shows the heat transfer coefficient of the rod surface. The heat transfer coefficient increases in the axial direction. It is dominated by the thermal properties of the sodium coolant. The heat conductivity increases with the coolant temperature, and the Nusselt number also increases with the Pelect number. The fluctuation of the heat transfer coefficient curve is caused by the wire spacers. The distance between the peak points is the same as the wire pitch of 180 mm. The presence of the wire enhances the heat transfer of sub-channel. This is due to the varying flow area in the sub-channel. The local coolant flow velocity is affected by the existence of the wire spacers.

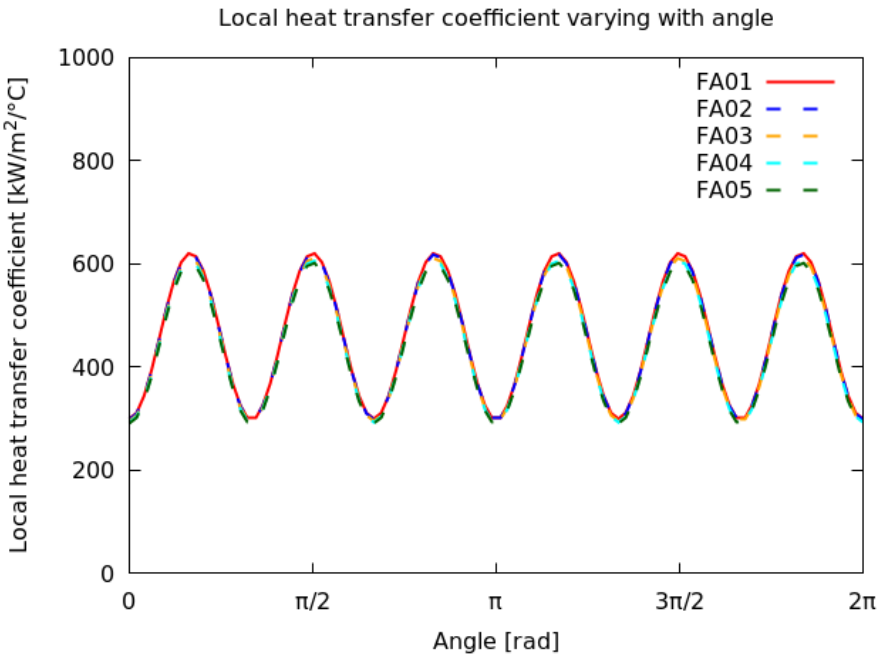

Figure 5.28.: The local heat transfer coefficient at the axial middle position of the central rod

By implementing Eqn. 4.109 into the MATRA code, the circumferential heat transfer coefficient distribution can be obtained. Over the cross section at the middle axial position of the fuel assemblies, the local heat transfer coefficient distribution around the central rods is illustrated in Fig. 5.28. The heat transfer coefficient distribution is cosine like, and the maximum heat transfer coefficient is about twice the minimum value. The number of peak points of the heat transfer coefficient in the circumferential direction of the cladding surface is 6, because the central rod is surrounded by 6 sub-channels and 6 rod-to-rod gaps. This periodical distribution shape is approximated by the proposed correlation. This implementation of the new correlation would not affect the MATRA simulation result. Because the special sub-channel volume is the basic numerical element, in which the averaged heat transfer coefficient is used to calculate the heat transfer.

The local heat transfer coefficient can be used to plot a detailed circumferential cladding to coolant temperature difference. The local cladding temperature is calculated with the coolant bulk temperature and the local heat transfer coefficient. The temperature difference euqals to the local cladding temperature minus the bulk coolant temperature. The local cladding to coolant temperature difference is shown in Fig. 5.29. The detailed circumferential fuel temperature distribution provides the information to engineers to evaluate the non-uniform local phenomena. As shown in this figure, the uneven temperature difference of the cladding surface is about 1.4 °C, this small value should be acceptable for the engineering safety analysis. Because of the high thermal conductivity of liquid

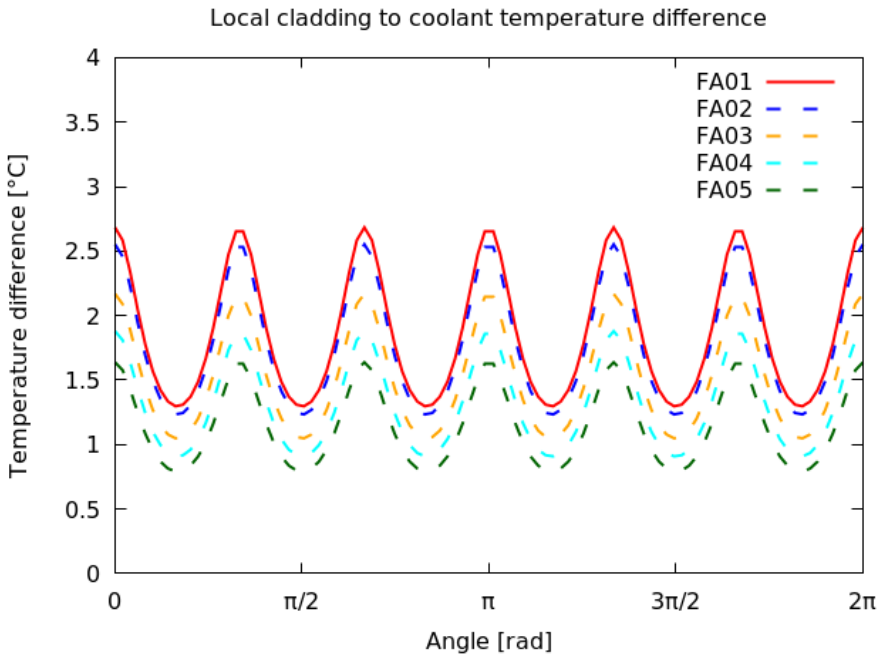

Figure 5.29.: The local cladding to coolant temperature difference at the axial middle position of the central rod

sodium, the non-uniform effect of the circumferential heat transfer results in a relatively small temperature fluctuation in the circumferential direction of the fuel cladding.

6. STH-CFD coupling simulation

Phenix was a small scale prototype fast breeder reactor. Before the closure of the Phenix reactor, a series End Of Life Tests were performed in 2009 [IAEA (2007)]. The main objectives of these tests were to increase knowledge about sodium fast reactors and to improve simulation codes. Two tests were performed, a natural convection test and a dissymmetrical configuration test [Grosjean (2015)]. The first test was studied in the frame of the THINS project, Huber (2017) performed the ATHLET-OpenFOAM coupling simulation of the natural circulation test. The second test is studied in the frame of SESAME project, the present study carries out the ATHLET-OpenFOAM simulation of the Phenix dissymmetric test.

The Phenix reactor has 3 primary pumps, and 2 secondary loops were in service. Each secondary loop includes 2 IHX. Before the start of the Phenix dissymetric test, the Phenix reactor was operated under normal condition. The operating power was 350 $MWth$. The test started from the trip of one secondary pump, its speed reduced from 700 to 100 rpm in about 13 s. The core was shut down automatically after 5 s from the beginning. Then the other secondary pump speed reduced from 700 to 110 rpm in about 60 s. The scram of reactor occurred at 48 s, and the test was ended at 1800 s.

To investigate the phenomena in the Phenix dissymmetric test, a group of simulations are carried out in the present study:

1. ATHLET standalone steady state simulation
2. ATHLET standalone transient simulation
3. ATHLET-OpenFOAM coupling steady state simulation
4. ATHLET-OpenFOAM coupling transient state simulation

In this chapter, the ATHLET model for the reactor system, the OpenFOAM model for hot and cold plenums, the ATHLET standalone simulation result and ATHLET-OpenFOAM coupling result are introduced.

6.1. ATHLET standalone model for Phenix

In the present study, a full Phenix model is created with AHTLET 3.0a. This model includes most important components in the primary system of the Phenix reactor. The main components are primary pumps, diagrid, reactor core, hot pool, intermediate heat

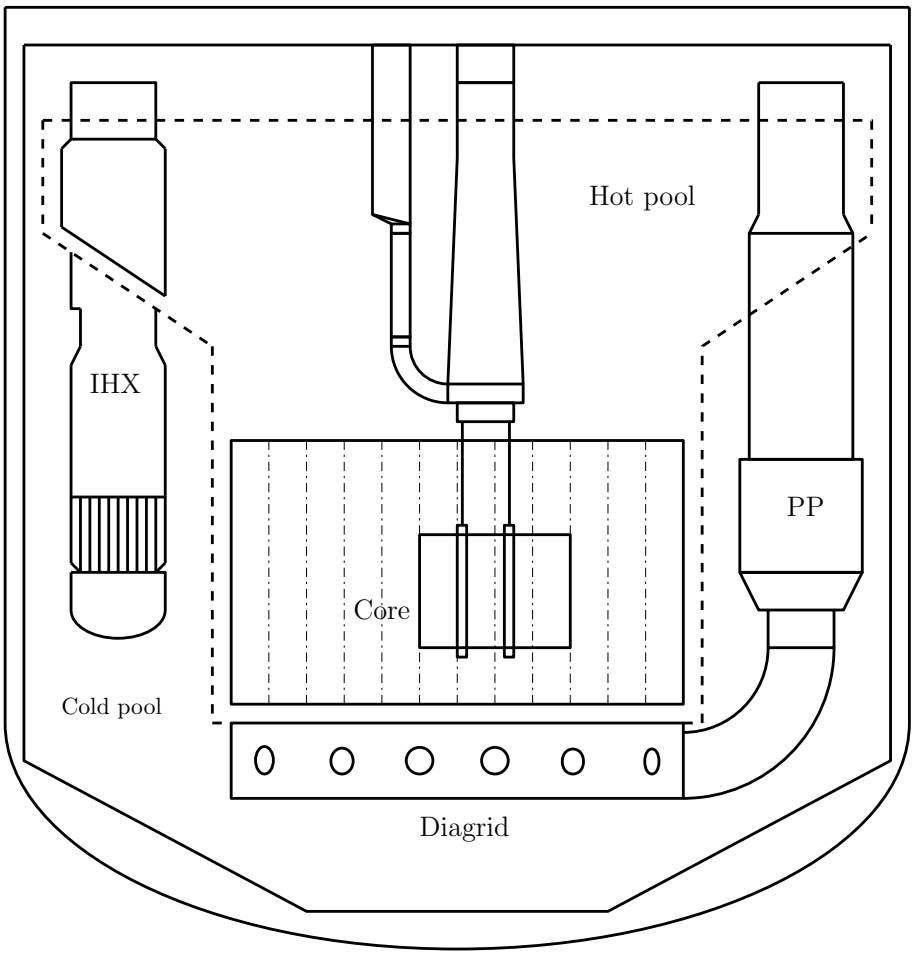

Figure 6.1.: Scheme for Phenix reactor

exchangers, cold pool. The decay heat of the reactor core is simulated by an internal heat source of fuel rods.

The schematic of the primary loop of the Phenix reactor is shown in Fig. 6.1. The in-vessel coolant space is divided into the hot- and cold pool. The two pools are connected by the primary pumps and the primary side of heat exchangers. The cold pool is surrounded by the vessel cooling pool, which is connecting the diagrid and the upper part of cold pool. The coolant is pumped by the primary pump from the cold pool to the diagrid, and most of the coolant flows through the reator core into the hot pool. In the present study, the dissymmetrical configuration test result is used to validate the simulation model.

6.1.1. Description of the STH model

In the STH model, the reactor core is divided into 6 zones, including inner core, outer core, blanket zone, control rod, fuel storage and steel zone. The 3 primary pumps and 4 intermediate heat exchangers are modeled separately. Each of the two heat exchangers are coupled with one secondary loop. In the primary loop, 90% of the coolant flows into the core, and 10% is used for the vessel cooling. The power of the core is simulated by the user given heat source. The pressure of argon layers of the two pools are balanced by a cross connection component.

As shown in Fig. 6.2, the pool type reactor is filled with the working fluid sodium, and the top of the system is covered by argon gas. The sodium coolant from the diagrid goes through the reactor core, and is heated by the fuel rods. The thermal power in 6 different

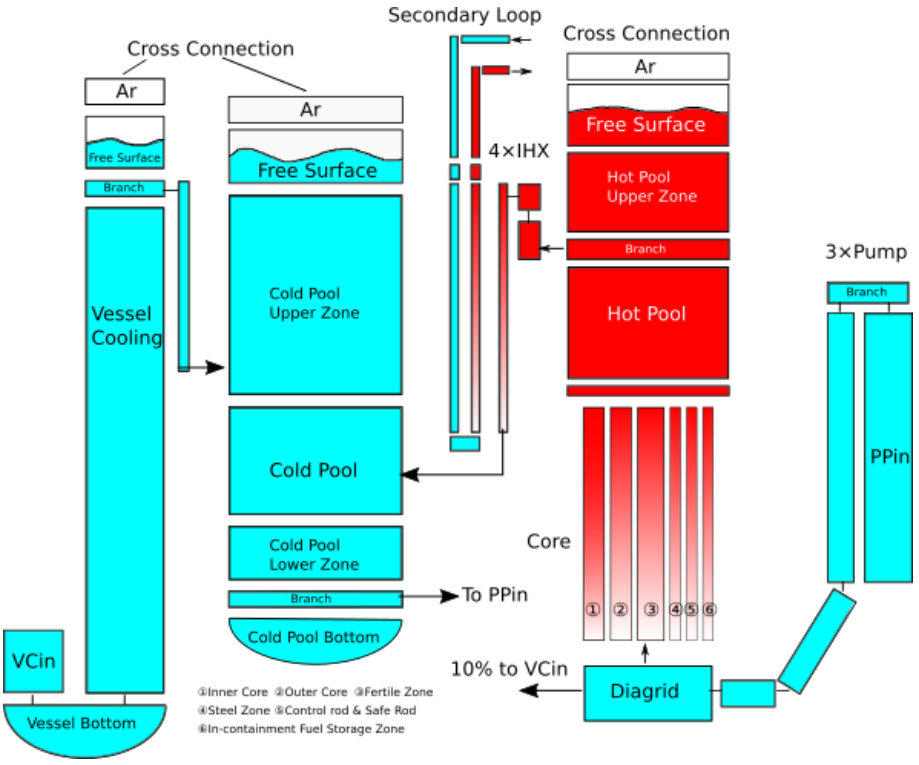

Figure 6.2.: ATHLET model for Phenix

core zones are given as an input. After being heated up by the core, the coolant flows into the hot pool, which is modeled as several big branches and pipes. Then the coolant from the hot pool is split into 4 intermediate heat exchangers. The heat is released through thermal conduction to the secondary side. In the secondary side, the time dependent inlet and outlet boundaries are given as an input for the two secondary loops. Each secondary loop goes into two heat exchangers. After cooling by the 4 heat exchangers, the sodium coolant flows into the cold pool, then it is mixed with the coolant in the bottom region, and flows into the pump inlet skirt. Finally it is pumped back to the diagrid again. About 10% of the coolant from the diagrid flows into the vessel cooling loop, and enters the cold pool from the surface region. The hot pool, cold pool and vessel cooling pool are connected by the argon layer with the cross connections. The argon gas works like a pressurizer to stabilize the system pressure.

The most important components in the primary loop are the primary pumps. The pump model is shown in Fig. 6.3. In this model, 3 primary pumps are used to connect the cold pool and the diagrid. The pump is discretized into 3 parts including the skirt of the pump, the turning section and the outlet pipe of the pump. The pump inlet skirt is simulated as a pipe component, and the turning point is modeled as a branch. Then it is connected to the pump model. The pump outlet is also modeled as a pipe which is connected to the diagrid.

In ATHLET, the differential pressure control model is used on the pump component. The pump speed is given as a constant value of 540 *rpm*. The experimental result gives the pressure difference value of 2.09 *bar*, which works as the driving force of the primary loop.

Another important component of the system is the reactor core. As shown in Fig. 6.4, the core is divided into 6 zones, including inner core, outer core, blanket zone, steel shielding zone, control rod zone, safe rod zone, and in-containment fuel storage zone.

In the ATHLET model, the flow path of the fuel assemblies in each zone are modeled. In

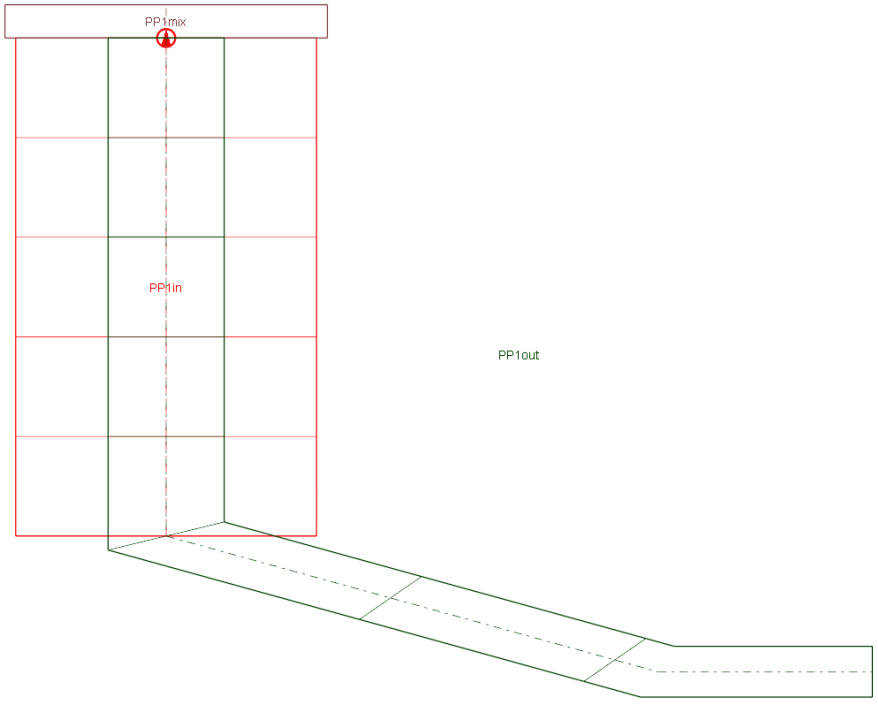

Figure 6.3.: Nodalization of the primary pump

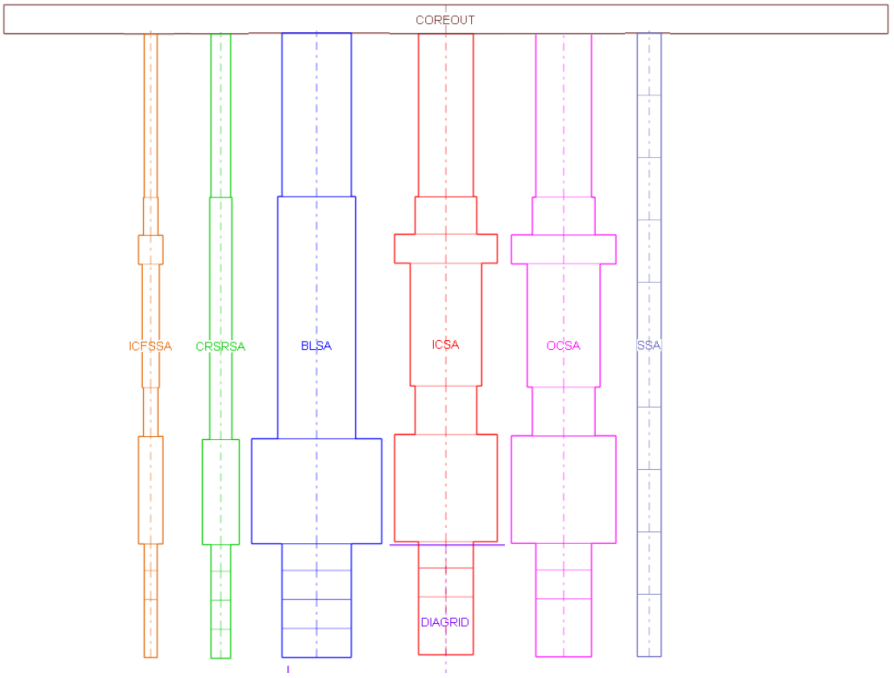

Figure 6.4.: Nodalization of the reactor core

each core zone, only one fuel assembly is modeled, and then the number of fuel assemblies in this zone is used as a multiplication factor. The cross section area of the flow path inside the fuel assembly varies in the flow direction. In the axial direction, the flow path of the fuel assembly can be divided into bottom nozzle, lower expansion plenum, blanket, fission fuel, upper expansion plenum, upper axial blanket, and shielding. The sodium flow path is thermally connected with the fuel rod model. The fuel rod is modeled as several

layers, the inner part of rod is MOX fuel pallet, and the outer part is the cladding material austenitic steel. The internal heat source is given as a user input. The configuration of the core is given as Table 6.1.

Table 6.1.: Configuration of the core

Core zones	Number of SA	Number of rods	Power per rod [W]
Inner core SA	54	11718	15437.79
Outer core SA	56	12152	11775.84
Blanket zone	86	5246	4593.98
Control rods and safety rod	7	1519	537.63
In containment fuel storage SA	3	1302	1305.68
Steel zone	6	1272	3278.7

Another important component is the intermediate heat exchanger. In the Phenix reactor, 4 heat exchangers are working. One secondary loop groups 2 heat exchangers together.

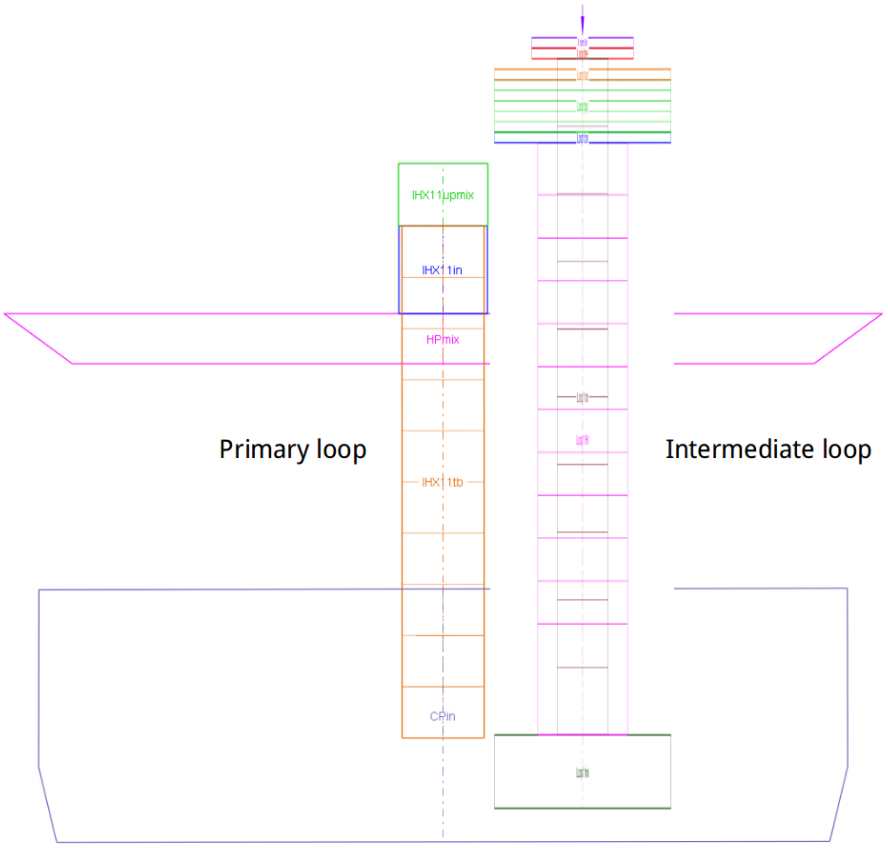

Figure 6.5.: Nodalization of the IHX

As shown in Fig. 6.5, the intermediate heat exchanger can be divided into primary side and secondary side. Both sides are connected by the heat conduction object. The heat of the coolant is released from the primary side to the secondary side by the heat conduction of the IHX tubes. In the flow path of the secondary side, the downward part is simulated as a vertical pipe. The flow direction changes to upward from the mixing branch component. In the upward part, the number of tubes is 2279, the hydraulic diameter of the upward section is 0.012 m and the cross section area is $0.258m^2$.

Except these main components, the hot pool, cold pool and vessel cooling pool are also modeled by pipes and branches. The primary side of the reactor is a closed loop, while the secondary side is an open loop that is used to provide the boundary conditions of the heat exchangers.

6.1.2. Boundary conditions for Phenix dissymmetric test

The simulation can be divided into two phases, the steady state and transient run. The steady state simulation result is compared with the nominal state values of the Phenix reactor. The transient simulation makes use of the steady state result as the initial condition. The boundary conditions for the steady state simulation are illustrated in Table 6.2.

Table 6.2.: Boundary conditions for steady state STH simulation

Parameters	Value	Unit
Total thermal power of core	350	MW
Rotating speed of primary pump	540	rpm
Secondary flow rate	690	kg/s
IHX secondary inlet temperature	320	°C

The Phenix dissymmetric test lasted for 1800 s. The boundary conditions provided for blind calculation are: power evolution, secondary inlet temperature for both circuits, and secondary mass flow rate for both circuits. All the provided data are used as the input data of the time dependent boundary condition.

The Fig. A.1 and Fig. A.2 show the evolution of the thermal power of the reactor core. The core power drops very fast after time 5 s. Fig. A.3 and Fig. A.4 show the mass flow rate in the two secondary circuits. The mass flow rate drops from 700 kg/s to less than 100 kg/s in 60 seconds. Fig. A.5 shows the inlet temperature of the two secondary circuits. Each circuit is connected with two intermediate heat exchangers. All the transient boundary condition curves are attached as appendix in this thesis.

With the time dependent boundary conditions and the initial condition from the steady state calculation, it is possible to start the ATHLET standalone transient simulation.

6.2. CFD model for hot pool and cold pool

To investigate the detailed local 3D flow and heat transfer phenomena in the hot pool and the cold pool of the Phenix reactor, two CFD models are created with OpenFOAM.

6.2.1. Geometry models for CFD

In the present study, the hot pool and the cold pool are isolated from the CAD model of Phenix. The core, heat exchangers and pumps are simulated by the STH code. The CAD models for the separated hot pool and cold pool are used to create the CFD models.

As shown in Fig. 6.6, the inlet patch is divided into 3 rings for inner core, outer core and blanket zone. Different inlet boundaries are given to each ring. The hot pool has 4 outlet panels which are the inlet windows of 4 operating heat exchangers. As Fig. 6.7 indicates, 4 inlet boundaries are placed at the positions above the outlet windows of the heat exchangers. They are inside the heat exchangers. The position of the inlet panel will help to get a reasonable velocity field at the outlet windows of the heat exchangers. The outlet boundaries of the cold pool are placed at the turning position of the pumps. They

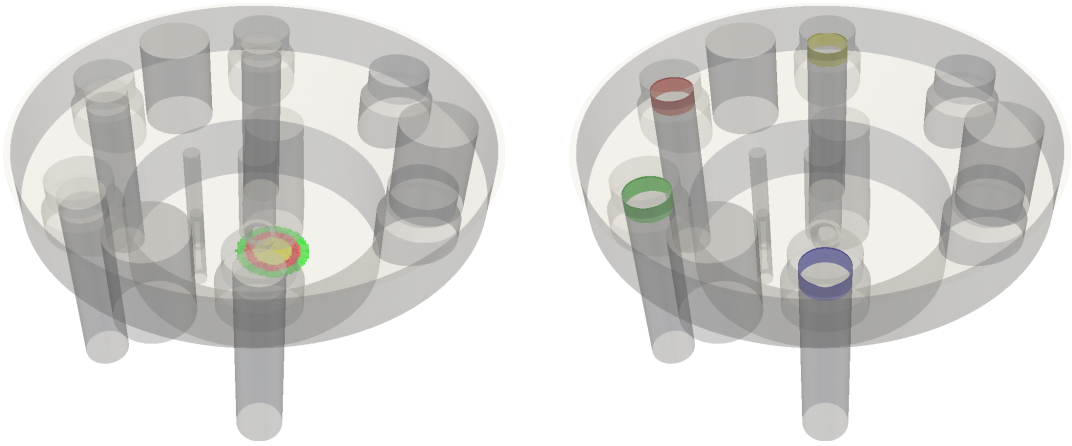

(a) Inlet (b) Outlet

Figure 6.6.: The inlet and outlet boundaries of the hot pool

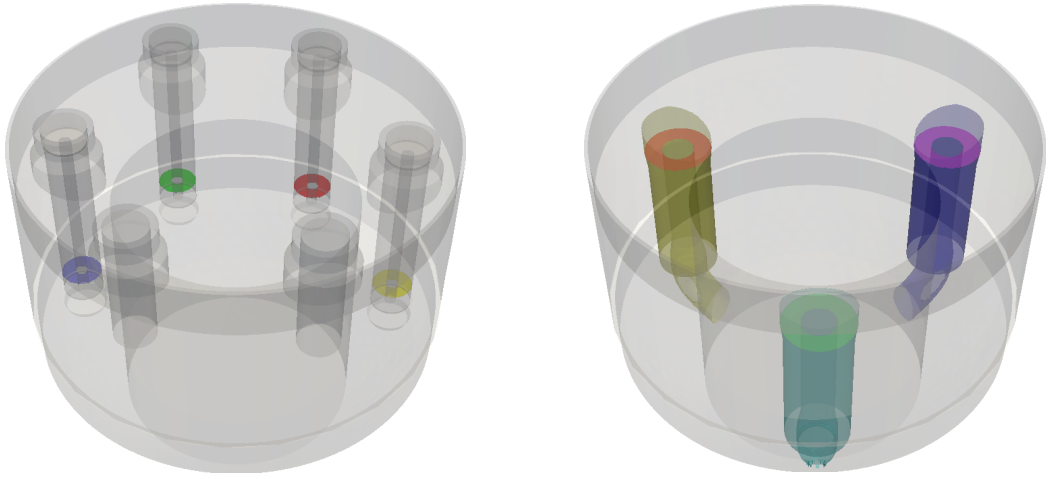

(a) Inlet (b) Outlet

Figure 6.7.: The inlet and outlet boundaries of the cold pool

are inside the pump skirt. This is also considered to cause less impact on the internal flow field of the cold pool, comparing with placing the outlet boundaries at the pump inlet panel.

6.2.2. CFD mesh generation

The CFD mesh is created with OpenFOAM snappyHexMesh, which is the mesh generator of OpenFOAM for complex geometries. The meshes for hot plenum and cold plenum are hex dominated. Because of limited computational resources, for the long term transient case, the grid number is limited to less than 5 million. The meshes are shown in Fig. 6.8 and Fig. 6.9.

The mesh generation procedure is similar to the rod bundle case introduced in the previous chapters. Firstly, the hex mesh are generated inside the geometry, then the mesh is refined at the near surface regions. Secondly, the points are snapped on the geometry surfaces. Finally, the additional layers are added to the wall boundaries.

6.2.3. Boundary conditions

With the meshes generated with the Phenix geometry files, the boundary conditions are imposed to the pre-defined patches of the two models.

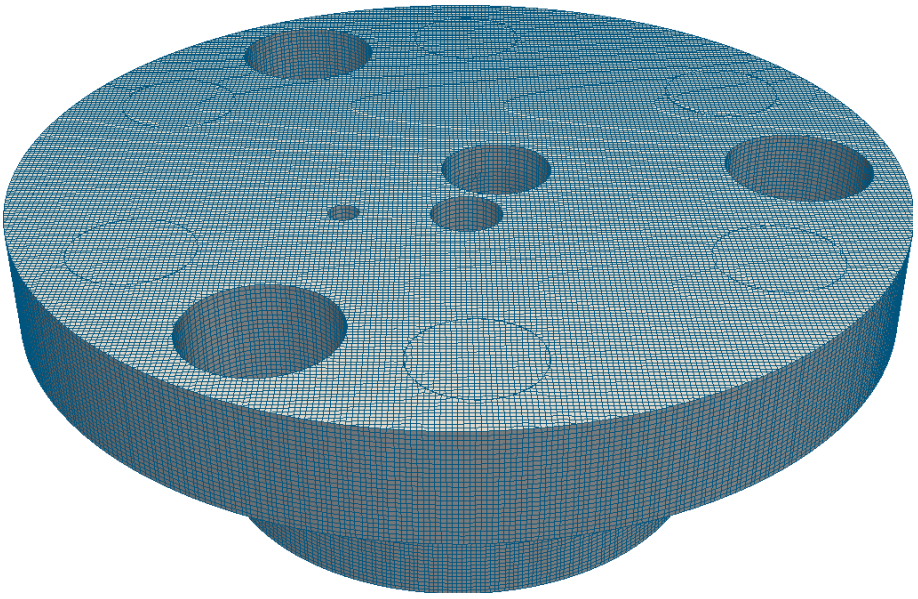

Figure 6.8.: CFD mesh for the hot plenum

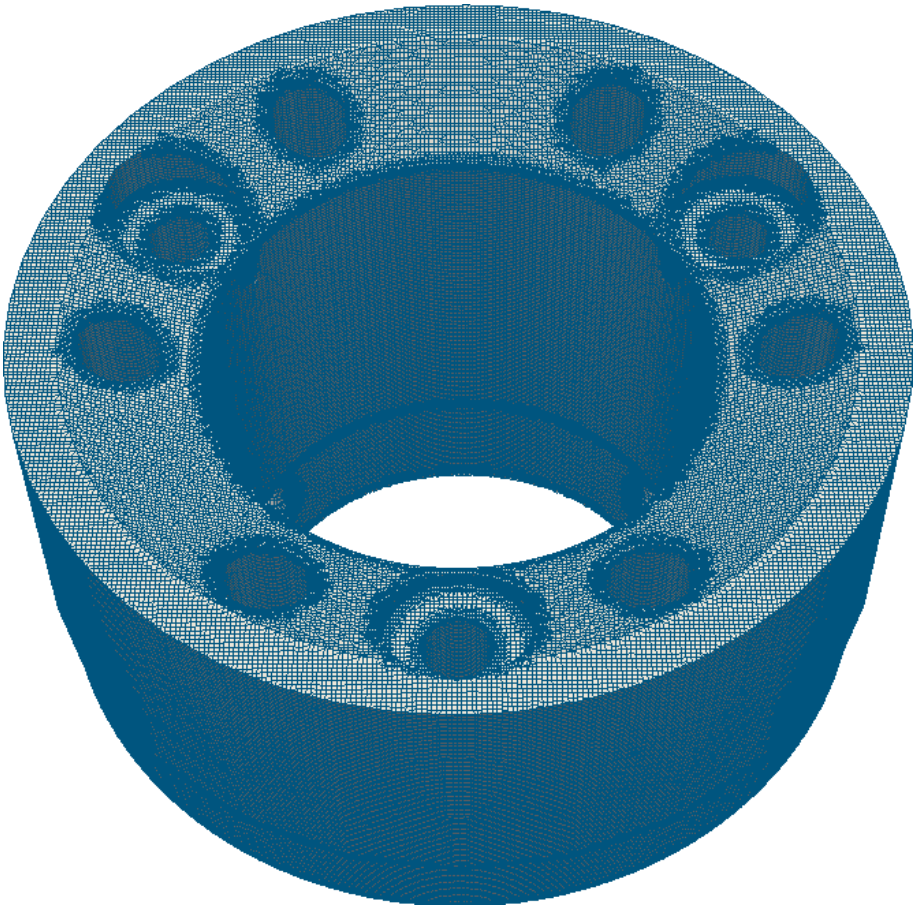

Figure 6.9.: CFD mesh for the cold plenum

For the hot pool, the inlet boundary is defined on the surface area which is exactly on the same position of the core outlet. The STH core outlet mass flow rate and temperature are used as the hot pool inlet boundary for momentum and energy equations. The outlet patch of the hot pool is defined on the surface area which is the same position of the IHX inlet. The IHX inlet pressure calculated from ATHLET is used as the outlet pressure

boundary of the hot plenum.

For the cold pool, the inlet boundary is inside the IHX. The mass flow rate and temperature of the IHX outlet window are used as the inlet boundary of the cold pool. To simulate the IHX outlet flow jet across the window, the inlet boundary of cold pool is moved inside the IHX vessel. This way, it is possible to get the local 3D flow field at the position of IHX outlet window. The CFD steady state simulation boundary condition is obtained from the ATHLET steady state simultion result of the Phenix reactor at nominal condition, which is the operating condition before the test. For the nominal operating condition, the local 3D phenomena have no influence on the core outlet and IHX inlet boundaries.

Table 6.3.: Boundary conditions for CFD steady state simulation

Inlet boundaries	Position	Value	Units
Inlet mass flow rate of hot plenum	Inner core outlet	861.0	kg/s
	Outer core outlet	779.0	kg/s
	Blanket zone outlet	348.0	kg/s
Inlet temperature of hot plenum	Average temperature of core outlet	798.0	K
Inlet mass flow rate of cold pool	IHX outlet	497.0	kg/s
Inlet temperature of cold pool	IHX outlet	657.6	K

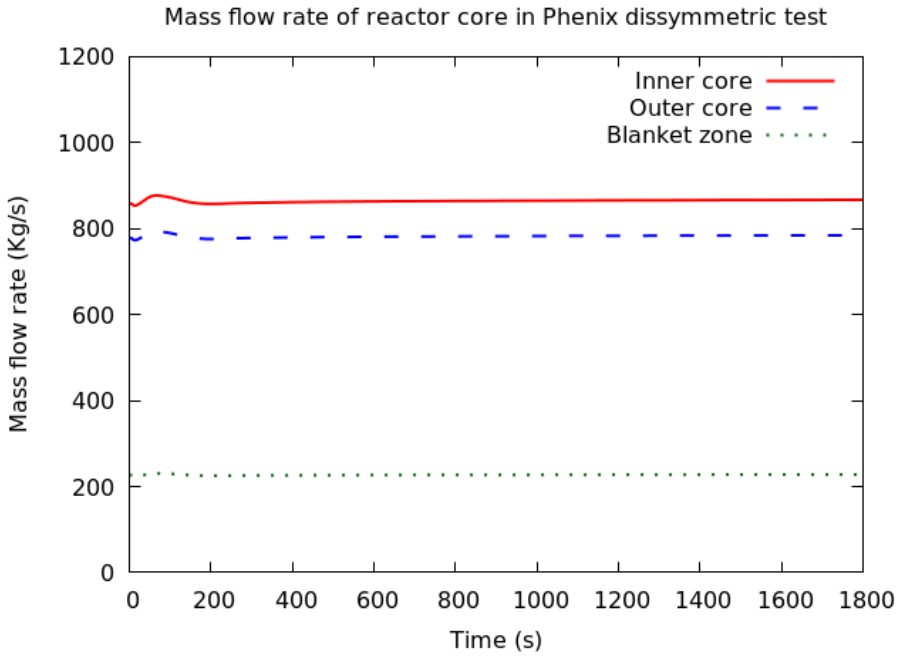

Figure 6.10.: Mass flow rate of core outlet

In the steady state simulation, the constant boundary conditions are given as Table 6.3. In the transient simulation, the time dependent boundary conditions are used with the values from the ATHLET standalone simulation. As shown in Fig. 6.10, the mass flow rates of the core outlet are very stable. This is because of the constant rotating speed of the primary pumps. The varying temperature boundary shown in Fig. 6.11 mainly influences the transient behavior of the hot pool. The core outlet temperature is also affected by the local flow field of the cold pool. So, this boundary condition would be corrected in the coupling simulation scheme.

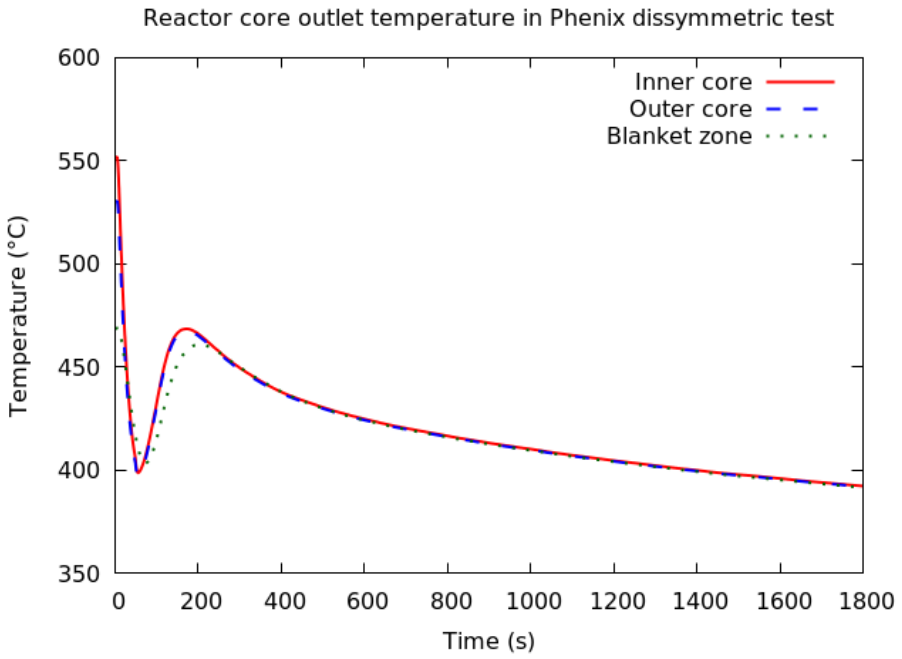

Figure 6.11.: Core outlet temperatures

In the CFD study, the $k-\omega$ sst model is used as the turbulence model. The solver of buoyantSimpleFoam and buoyantPimpleFoam are used to solve the steady state and transient state. In the transient case, the time dependent boundary condition is obtained from ATHLET calculations.

6.3. ATHLET-OpenFOAM coupling scheme

The version of ATHLET used in the present study is ATHLET 3.0a. A coupling scheme following Fig. 6.12 is used in the present study. This scheme is based on a previous version proposed by Huber (2017). The main improvement is that the cold pool is introduced in the simulation data flow.

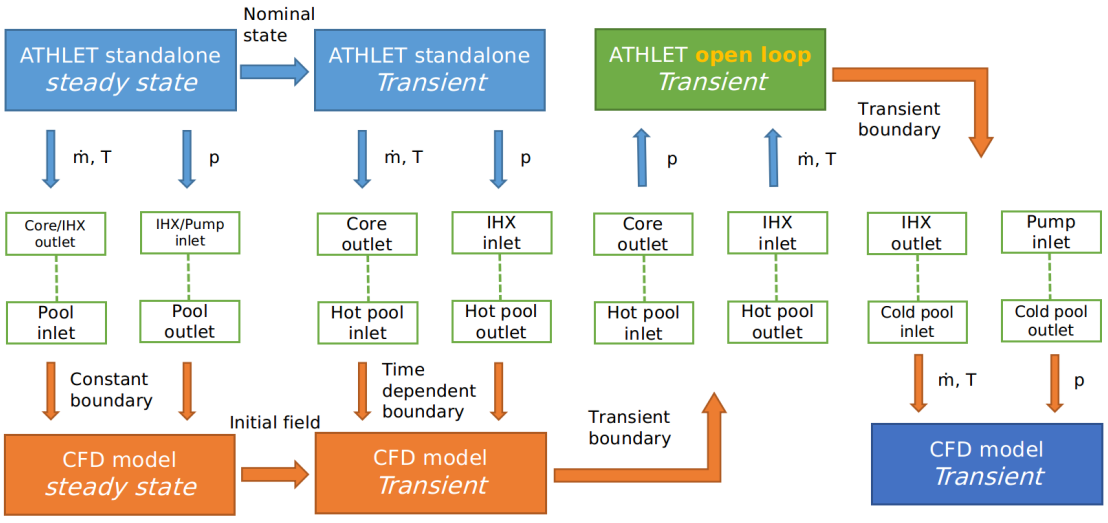

Figure 6.12.: Data flow of ATHLET-OpenFOAM coupling scheme

The coupling starts from the ATHLET standalone simulation. In the standalone simulation, both hot pool and cold pool are included in the closed loop. The ATHLET standalone steady state simulation, results are used as the constant boundary conditions for the CFD steady state simulation. The core outlet mass flow rate and temperature are used as the inlet boundary of the hot pool, while the IHX inlet pressure is used as the outlet boundary of the hot pool. For the cold pool, the IHX outlet mass flow rate and temperature are given as the cold pool inlet boundary, while the primary pump inlet pressure is used as the outlet boundary of the cold pool. After finishing the steady state calculation of CFD and STH, both of the results are taken as the initial filed of the transient simulation. First, the ATHLET standalone transient simulation is carried out with the time dependent user input boundary, including core power, secondary mass flow rate and temperature. Then the transient simulation result is imposed as the time dependent boundary of the CFD model for the hot plenum. The hot pool outlet has the same position as the IHX inlet. The mass flow rate and temperature are provided as the inlet boundary of the open loop ATHLET transient case, while the hot pool inlet pressure is used as the pressure boundary of the STH simulation. The differences between the open loop ATHLET model and the ATHLET standalone model are all the components in the region of hot pool are removed from the ATHLET model for Phenix, and the inlet and the outlet boundaries are added to the two ends of the open loop model. The transient simulation result of the ATHLET open loop case is used as the boundary of the CFD model for the cold pool. Then one complete cycle of the coupling simulation is carried out.

6.4. CFD simulation for local 3D phenomena

6.4.1. CFD steady state simulation results

The steady state simulation is performed before the transient simulation. The simulation result of the steady state case is used as the initial field of the transient case. The key point of the steady state simulation is to get the velocity field in the hot pool and cold pool, while the temperature field is assumed the have an almost uniform distribution in the two pools. For the steady state simulation of the hot pool and cold pool, the results are shown

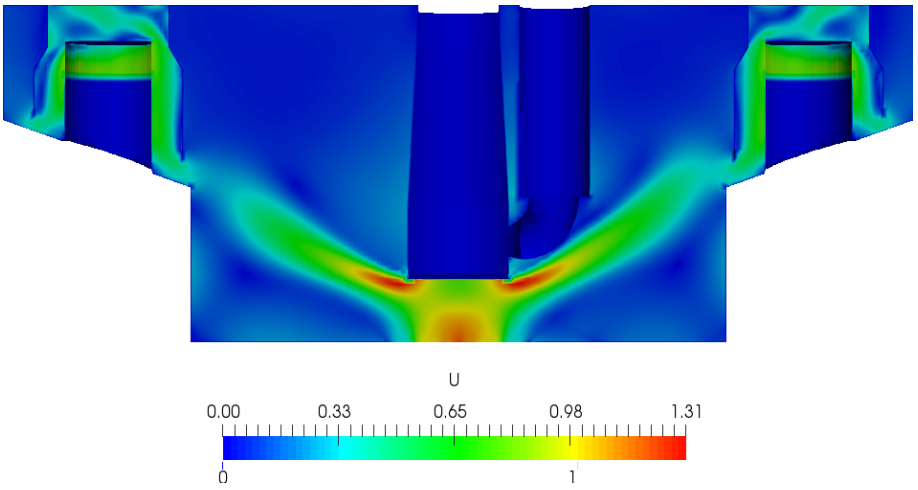

Figure 6.13.: Velocity field of hot pool at steady state

in Fig. 6.13, Fig. 6.14 and Fig. 6.15. The temperature field is assumed to be uniform for either hot pool or cold pool in steady state, the thermal stratification is neglected. In the hot pool, the core outlet flow encounters the handling machine, and spreads upward to the upper part of the hot pool. In the lower plenum, coolant go through the outlet windows of the IHXs, the flow direction is obliquely downward. This flow direction towards to the

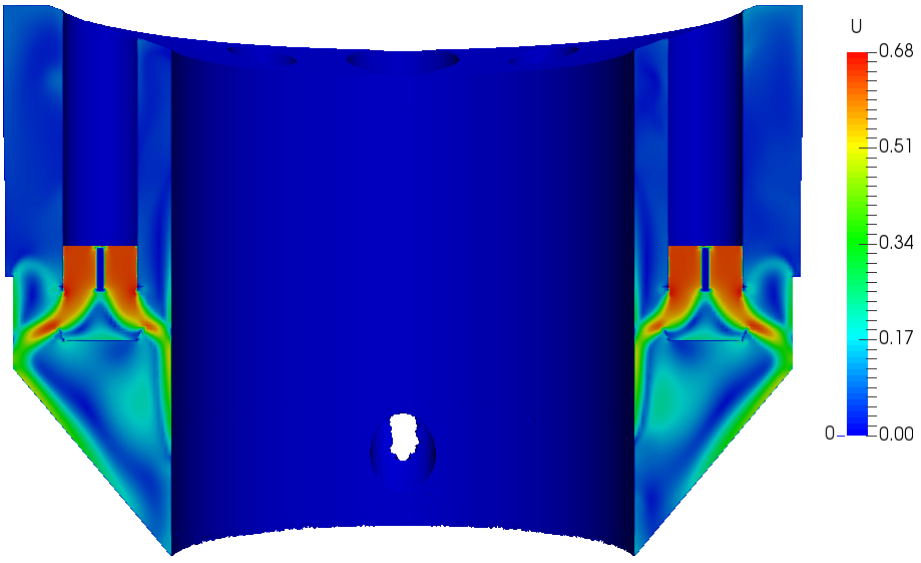

Figure 6.14.: Velocity field of cold pool across the IHX at steady state

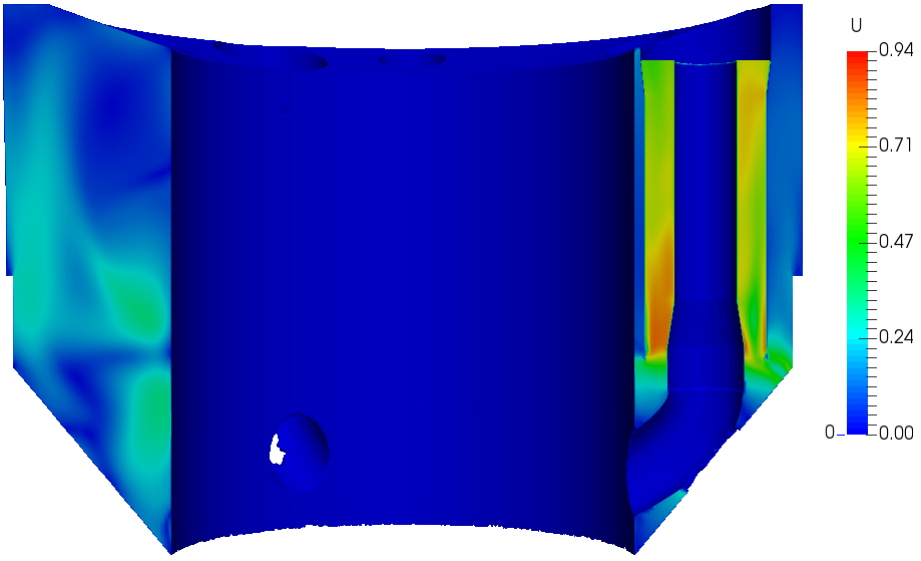

Figure 6.15.: Velocity field of cold pool across one primary pump at steady state

primary pump inlet. The velocity field obtained from the steady state simulation of two pools is used as the initial field of the transient simulation. The cross section of the slice panel in Fig. 6.13 and Fig. 6.14 is the line across IHXM and IHXG which is shown in Fig. B.6. The cross section of Fig. 6.15 is over the slicing line across PP1 in Fig. B.6.

6.4.2. CFD transient simulation results

The transient simulation starts from the steady state simulation results. With time dependent boundary conditions from the ATHLET standalone simulation. The CFD simulation is performed with OpenFOAM.

Fig. 6.16 shows the temperature evolution of the hot pool. The thermal stratification can be observed from $t = 50\ s$. The lower temperature coolant flows from the core outlet into the hot pool. Due to the buoyancy force, the hot sodium coolant flows to the upper zone of the hot pool. The flow field is also affected by the internal structure of the hot pool. The core outlet flow encounters the handling machine, and then the flow direction

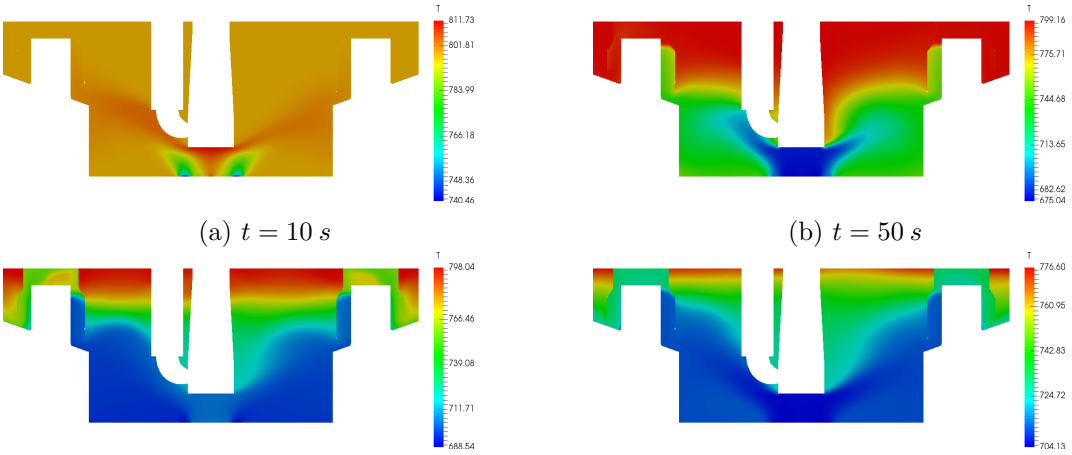

(a) $t = 10\ s$ (b) $t = 50\ s$

(c) $t = 100\ s$ (d) $t = 200\ s$

Figure 6.16.: Temperature field of over the cross section of the hot pool

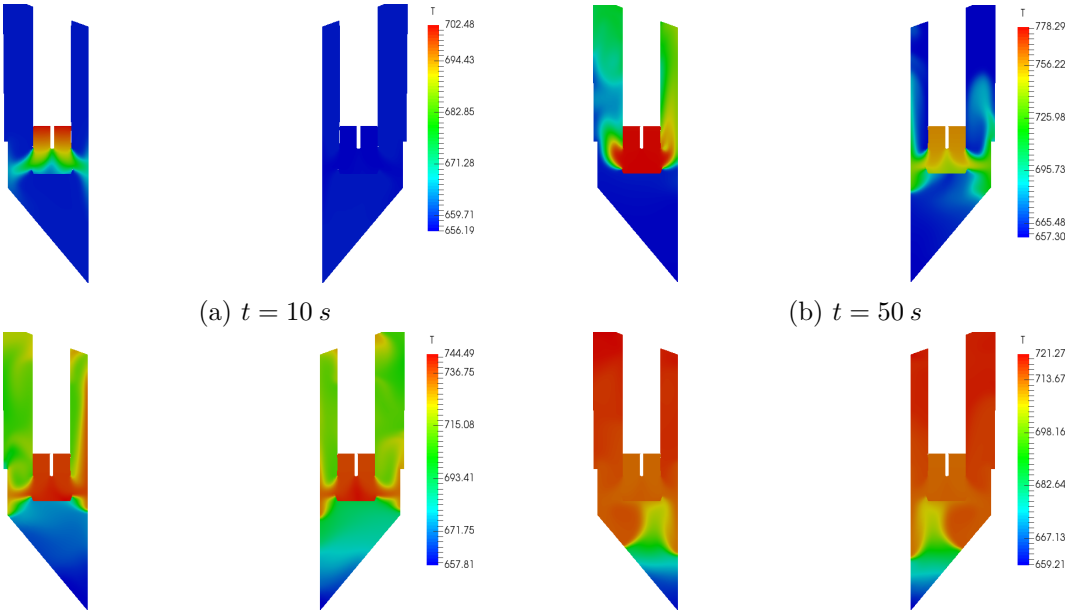

(a) $t = 10\ s$ (b) $t = 50\ s$

(c) $t = 100\ s$ (d) $t = 200\ s$

Figure 6.17.: Temperature field of the cold pool over the cross section of IHX

is changed. The strong 3D effect of the hot pool influences the temperature fluctuation at the IHX inlet windows.

Fig. 6.17 illustrates the temperature field of the cold pool, the cross section is over the two IHX. The flow direction at the outlet window of the IHX is very important. If the flow directs toward the primary pump inlet, it will result a high inlet temperature. The flow direction is downward at $t = 10\ s$, because of the inertia of the moving fluid. It turns to upwards at $t = 50\ s$. This is due to the strong buoyancy force. Form $t = 100\ s$, the flow direction is changed to horizontal. The changes of the flow direction at the IHX outlet window influence the temperature at the inlet of the primary pump. The cross section of Fig. 6.16 and Fig. 6.17 is the line over IHXM and IHXG as shown in Fig. B.6.

Fig. 6.18 shows the temperature distribution of the cold pool. The cross section is over one primary pump. At $t = 10\ s$, the hot sodium coolant enters the pump skirt. At $t = 50\ s$, the temperature inside the pump skirt is lower than the outside. The difference of the temperature is caused by the flow field of the cold pool. The cross section of Fig. 6.18 is

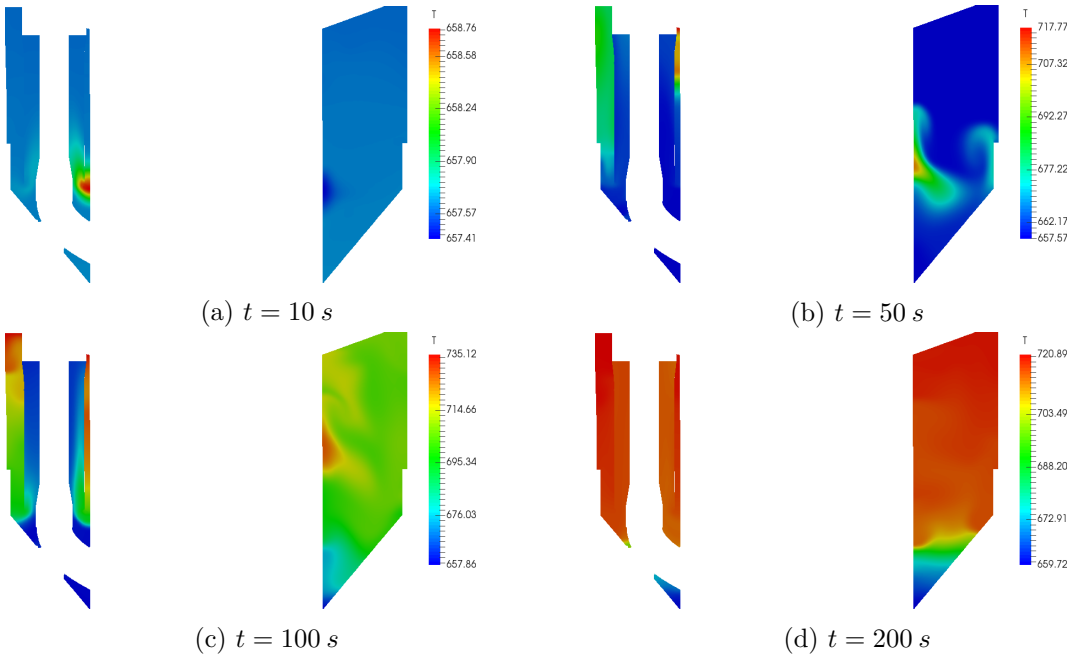

(a) $t = 10\ s$ (b) $t = 50\ s$

(c) $t = 100\ s$ (d) $t = 200\ s$

Figure 6.18.: Temperature field of the cold pool over the cross section of primary pump

the line over PP1 as shown in Fig. B.6.

6.5. Comparison between coupling result and experimental data

With the coupling scheme, an ATHLET-OpenFOAM coupling simulation was carried out for the Phenix dissymmetric test. In the present study, only the short term simulation results are introduced. The first 200 s coupling results are compared with the ATHLET standalone simulation results and experimental data. The identifications of the inter mediate heat exchangers (IHX) and primary pumps (PP) are illustrated in Fig. B.6. IHXM, IHXK, IHXJ and IHXK are 4 heat exchangers on service. The 4 IHX are connected to 2 secondary loops. PP1, PP2 and PP3 are 3 primary pumps.

As two very important parameters in the reactor system, the core inlet and outlet temperatures are analyzed. As illustrated in Fig. 6.19, the temperatures of the diagrid and core outlet given by the coupling calculation are compared with the ATHLET standalone simulation. In the first 100 s, the coupling result is almost the same as the standalone case. The temperature difference between core inlet and outlet decreases very fast due to the core shut down, and the temperature difference becomes stable. The core outlet temperature drops because of the core power drop. After 50 s, the core inlet outlet temperatures start to rise up, and then reduce a little bit. The increase of the core inlet temperature is caused by the secondary cooling ability loss. The main finding is that the temperatures predicted by the coupling calculation is about 35 degrees higher than the result predicted with the ATHLET stand alone model, while the inlet outlet temperature difference is very similar within the two different numerical approaches. The outlet temperature difference is mainly dependent on the core power and the inlet temperature. The core power is the identical for both simulations. While, the difference of the inlet temperatures is mainly caused by the cold pool behavior. In the ATHLET standalone simulation, the cold pool is simulated as several big volumes, connecting the IHX outlets and the primary pump inlets. The big cold pool works like a heat storage tank, and the “hot” fluid from the IHX outlet window are cooled by the heat sink. So, the AHTLET standalone result is relative

lower than the coupling result after 100 s. In the coupling simulation, the "hot" fluid flow through the cold pool, and the fluid sucked by the primary pump is dependent on the internal flow field of the cold pool. The non-uniform temperature field of the cold pool results a higher core inlet temperature. This is the explanation of the discrepancy between the coupling result and the standlone result.

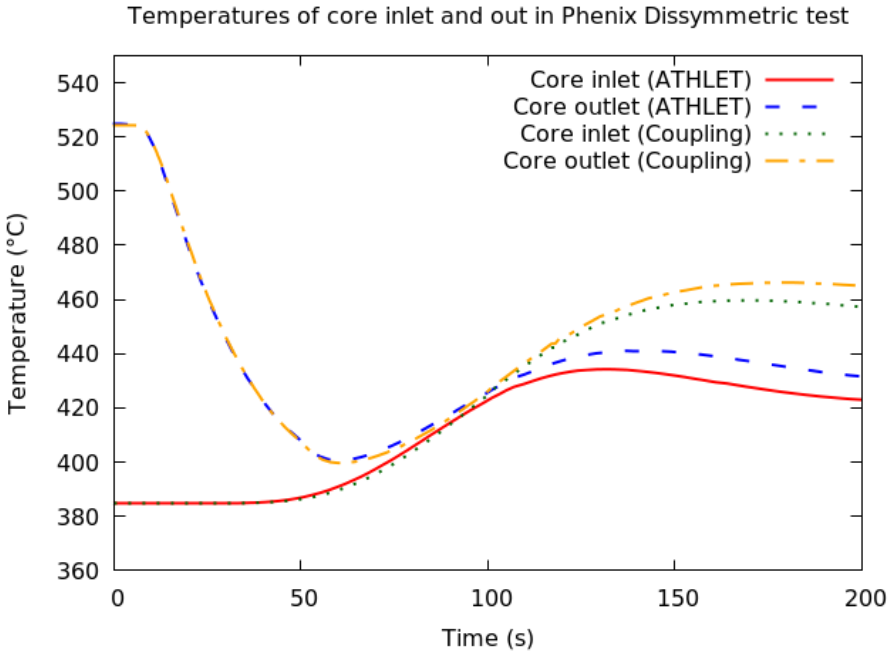

Figure 6.19.: Temperatures of core inlet and outlet

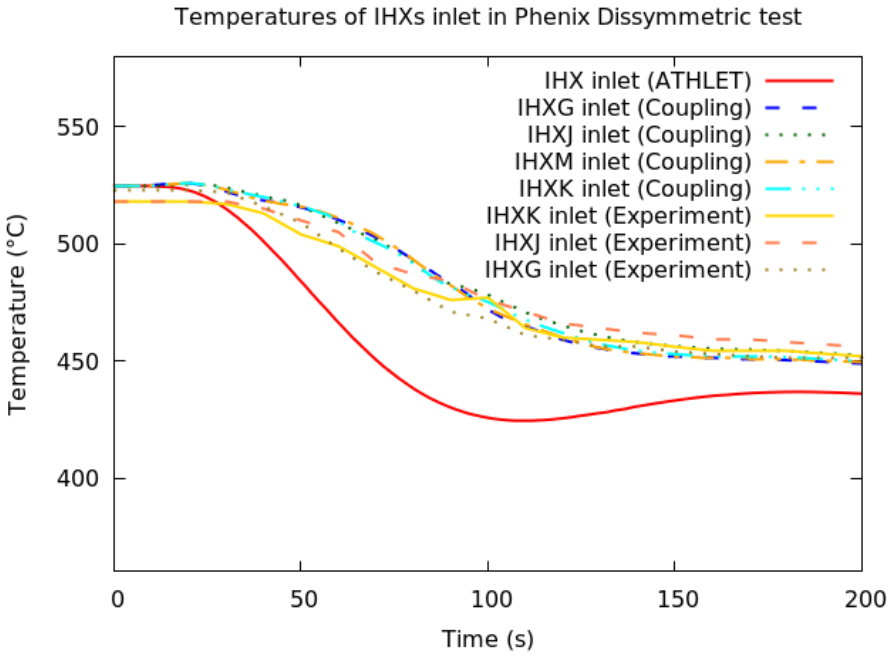

Figure 6.20.: Temperature of IHX inlet

Fig. 6.20 shows the temperature of IHX inlet varying with time. The CFD simulation gives 4 temperature curves for each IHX inlet window. The 3D effect analysis is impossible with

the lumped parameter approach, only one temperature curve was given by the ATHLET standalone simulation. In the first 200 s, the temperature predicted by ATHLET standalone case changes faster than the one predicted by the CFD model. The temperature difference between the ATHLET result and the CFD result is mainly due to the local 3D flow field in the hot pool. In the nodalization of the ATHLET model, a majority part of the big pool is above the IHX inlet position, and the core outlet is connected to the IHX inlet by the branch and pipe for a part of hot pool. It mean the coolant from core outlet flows through a part of hot pool region into the IHX directly. The heat of the upper part hot pool can not be transferred to the lower part. The upper hot pool doesn't works as heat tank to release its energy to average the core outlet flow in the ATHLET standalone case. This results a lower calculated IHX inlet temperature with the ATHLET standalone model. With the coupling scheme, the 3D flow field of hot pool can be resolved, and the result is well agreed with the experimental data.

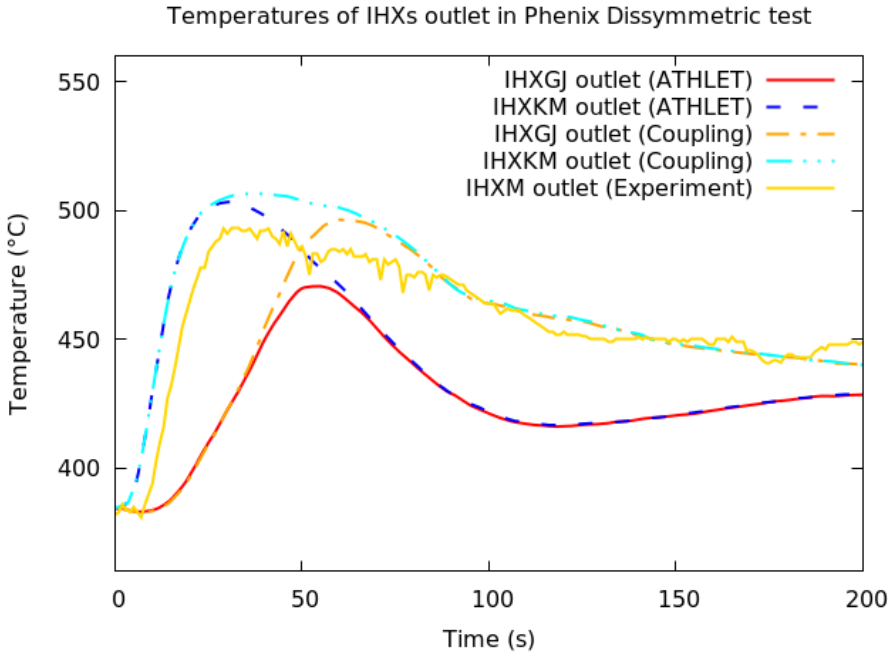

Figure 6.21.: Temperature of IHX outlet

The Fig. 6.21 shows the temperature of IHX outlet varying with time. In this case, only one group of experimental data for IHXM is recorded in the Phenix dissymmetric test. The outlet temperature of the other IHX is missing. It is clearly visible that the outlet temperatures of two IHX from the two secondary circuits are different. The outlet temperature of the IHX from the secondary circuit 1 is higher than the secondary circuit 3, because the boundary conditions of the two secondary circuits are different. The prediction results from the ATHLET standalone simulation and coupling simulation are in good agreement in the first 30 s. Then the results start to differ from each other. At the time point of 100 s, the outlet temperature of IHX predicted by the coupling method is about 50 degrees higher than the result from the ATHLET standalone case. This is caused by the different IHX inlet temperature shown in Fig. 6.20. The difference of the IHX inlet temperature is mainly caused by the pool convection effect of hot plenum. The hot plenum works like a heat storage sink, and the internal 3D flow field affect the IHX inlet temperature. The coupling simulation result of IHXM outlet is well agreed with the experimental result.

The CFD can predict both the velocity field and temperature field in the hot pool with

representation of the internal structures like the handling machine. For the cold pool, the CFD can also give a more detailed simulation result by resolving the pool internal flow field. The cold pool releases the stored heat much faster with the CFD model than the result predicted by the STH model.

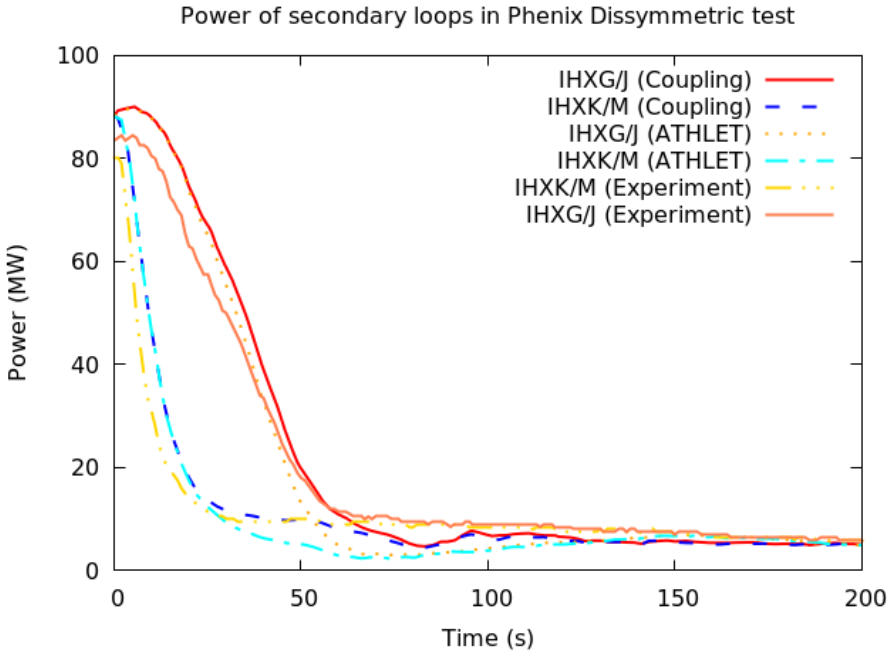

Figure 6.22.: IHX power transferred

Fig. 6.22 shows that the power of the IHX depends on the secondary loop with whom it is connected to. The coupling result is very similar to the ATHLET standalone result. The power of IHX G/J is higher than IHX K/M. It is because of the different boundary conditions of the two secondary loops. For both coupling simulation and ATHLET standalone simulation, the thermal component of IHX is simulated by ATHLET thermal object. The boundary condition on the secondary side of the ATHLET heat exchanger model is given as user input, then the power is only dominated by the IHX inlet temperature which is shown in Fig. 6.20. The lower IHX inlet temperature predicted by the ATHLET standalone simulation results in a lower power after 50 s as shown in the figure.

As shown in the Fig. 6.23, the inlet temperature of the primary pumps calculated by CFD is lower than the result from the ATHLET standalone case. The explanation of the temperature difference is that the cold pool works like a heat sink, although the fluid temperature from the IHX outlet rises, the heat can be absorbed by the huge cold pool. The coupling result shows that the primary pump inlet temperature almost does not change in the first 200 s, while the ATHLET standalone simulation shows a fast rise of temperature.

Generally, the coupling simulation results show to be better consistent with the experimental results. This is because of the coupled CFD simulation of the big pool internal flow field. The local 3D flow field has a big influence on the IHX inlet and primary pump outlet temperatures, which can not be captured by the system thermal hydraulic code. But there are still some discrepancies between the coupling results and the experimental data, further research work on the sensitivity study of the STH model nodalization should be carried out in the future.

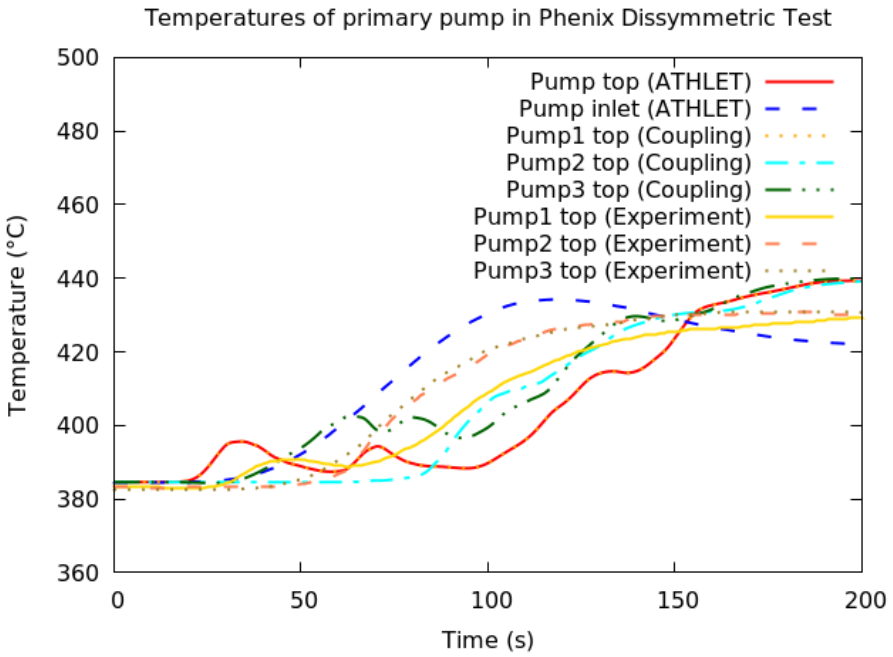

Figure 6.23.: Primary pump inlet temperature

7. Conclusion and Outlook

This study focuses on the thermal hydraulic behavior of the fuel assembly and the system of SFR. For the fuel assembly, two new models for sweeping flow and local heat transfer are proposed. The thermal hydraulics of a complete fuel assembly are investigated with a sub-channel approach. For the system, the Phenix dissymmetric test is studied with the STH-CFD coupling method.

In the present study, several numerical tools are used for multiple scale approaches. The CFD code OpenFOAM is used for the detailed flow field of the fuel assembly and the 3D phenomena of the hot pool and the cold pool. The sub-channel code MATRA is used to analyze the thermal hydraulics of a complete fuel assembly. In the simulation of the Phenix dissymmetric test, OpenFOAM is coupled with the STH code ATHLET for the study of the system behavior. Besides the multi-scale simulations, two mathematical derivations are carried out for the sweeping flow and local heat transfer. Two new correlations are obtained, and the local heat transfer model is implemented into the code MATRA for detail local heat transfer output.

This chapter is intended to illustrate the conclusions of the present study, and to give an outlook of the future work in this field.

7.1. Conclusion

The main contributions by this study are concluded into the following findings:

- The transverse flow across the gap of a wire wrapped 19-rod bundle is studied in this work. The transverse flow rate is considered as a function of P/D and H/D ratios. Based on the wake and friction force balance model, two new semi-empirical correlations are proposed: (1) The first correlation is used to predict the swirling flow rate induced by a single wire wrapped rod which is surrounded by the bare rods. This correlation considers the P/D ratio as well as the H/D ratio. The present work shows that the new correlation agrees well with the CFD results. (2) The second correlation is based on the first correlation. A cosine like function is used to predict the transverse velocity distribution shape in the axial direction for the central channels of a fully wire wrapped rod bundles. The inter-channel cross flow direction changes periodically as a cosine function. The amplitude is predicted by the first proposed correlation, which is a semi-empirical part of the function including two important geometry parameters. The correlation is also validated by the CFD

results. In the present study, two new findings are presented: the first main finding is the relationship between the sweeping flow rate and the P/D ratio, which has never been investigated in previous studies. The other finding is that the shape of the sweeping flow in a gap is mainly affected by the four neighboring wired rods. The proposed sweeping flow model is also an important boundary condition for the derivation of the local heat transfer model.

- The triangular arrangement of the fuel rods and the wire spacers may result in an uneven local heat transfer. The circumferential heat transfer of the fuel rod is investigated in the present study. First, the governing equations for the finite fuel element of a infinite number triangular arrayed rod bundle is established with the continues and symmetric boundary condition. The governing equations group is solved manually. Several solutions that are of practical engineering interest are obtained. The most important one is the normalized local heat transfer coefficient. With some simplifications, a correlation is proposed for the circumferential heat transfer of the fuel rods in triangular arrangement. The heat transfer coefficient at the rod surface facing to the channel center is higher than in the gap region. Besides the mathematical study, two different CFD models are generated for the bare rod bundle and the wire wrapped rod bundle. Two main findings in this study are: (1) The normalized local heat transfer coefficient distribution around the fuel rod is a periodical oscillation, whose phase number is 6 that is equal to the number of surrounding sub-channels. (2) The CFD model for a bare rod bundle with symmetry boundary and cyclic inlet outlet boundary is used to simulate the conjugated heat transfer of fuel and coolant. The cladding outer surface temperature distribution shape is in contrast to the heat flux distribution shape. The normalized heat transfer coefficient distribution is a cosine like function, which agrees with the correlation proposed in the present study. (3) The simulation result of a 19 wire wrapped rod bundle shows a non-uniform local heat transfer distribution, which is also in a good agreement with the proposed model.

- In the sub-channel analysis, the code MATRA is improved for sodium cooled reactors. The thermal property package for sodium is added to the code. Based on the literature review, the pressure drop model, heat transfer model and turbulent mixing model specified for the liquid metal are implemented into the code. The proposed local heat transfer model is also implemented for the detailed local information output. After the modification of the code, the ORNL 19-rod benchmark test result is used to validate the improved code. The simulation result agrees with the test data. For the application of the complete fuel assembly of ASTRID and New ASTRID, a pre-processing function is developed for the MATRA code. The nodalization and numbering are generated automatically with the user input. A 217-pin rod bundle for the ASTRID fuel assembly, and a 271-pin rod bundle for the New ASTRID fuel assembly are modeled with the MATRA code. The 271-pin model is used for the sensitivity study of the New ASTRID reactor core. The core power is modeled as a chopped cosine distribution in both axial and radial direction. The simulation gives the mean coolant temperature of fuel assemblies at different core positions. The maximum exit temperature is at the outlet position of the central fuel assembly. The exit temperature of the sub-channel mainly depends on the position. The wall sub-channel has a relatively lower exit temperature, but the highest mass flux. The corner channel has the lowest exit temperature, because of the smallest heating perimeter. The position of the peak temperature of the fuel center is at the upper part of the fuel assembly, which depends on the power distribution and also the coolant temperature. The result shows that the heat transfer coefficient is affected by the wire spacer. The output of the local cladding temperature shows that the

fluctuation amplitude of the circumferential temperature is very small.

- The system thermal hydraulic code ATHLET 3.0a and the open source CFD code OpenFOAM are used to investigate the phenomena of Phenix dissymmetric test. Both steady state simulation for nominal state and transient simulation for the test were carried out with both, an ATHLET standalone model and a coupling scheme. The ATHLET-OpenFOAM coupling scheme proposed by the present study includes the ATHLET standalone model, one open loop ATHLET model, one CFD model for hot pool, and one CFD model for cold pool. In the steady state simulation, the temperatures predicted by STH agree well with the nominal state. In the transient state simulation, The ATHLET standalone simulation result is not well agreed with the experimental result. Compared with the ATHLET standalone simulation, the coupling method with CFD model for detailed local 3D effect gives better results on the temperature evolution of the IHX and primary pumps. The difference is mainly because of the pool convection simulation with CFD. The big pools play as an big heat sink, the pool outlet temperature is affected by its internal 3D flow field. The simulation result shows that the coupling simulation can give a more detailed information about the local behavior, for example the pump inlet temperature depends on the instability of the buoyancy flow. The transient temperature fluctuation can be obtained with the coupling scheme, and the result is more close to the experimental data. It is possible to use the coupling scheme to get the detailed local flow and heat transfer phenomena.

7.2. Outlook

Further future work should be carried out based on the results obtained by the present study. Several suggestions for further research are:

- Further experimental studies should be carried out to validate the sweeping flow correlation and the local heat transfer correlation proposed by the present study.
- Further improvement of the sub-channel code MATRA should be carried out, by implementing the proposed new models.

In the present study the proposed sweeping flow is not able to be implemented into the MATRA code, because of the fundamental numerical scheme can not be changed. In MATRA code, the diversion flow velocity is calculated by the lateral pressure difference and the inter-channel form resistance. While, the proposed sweeping flow correlation is a function of the geometry input. This direct calculation of the sweeping flow distribution can not be combined into the pressure-velocity coupling scheme of MATRA code. In the present study, the proposed local heat transfer model is implemented into the MATRA code as a function for post processing. In the future, a 3D fuel rod model is suggested to be implemented into the MATRA code, the circumferential heat transfer correlation will work as the boundary condition for the heat conduction of the fuel rod model. This will give a more detail internal temperature distribution of the cladding. Both the proposed correlations are only validated with the CFD simulation results. The fundamental experimental work is suggested for the studying of the wire induced inter-channel flow velocity and the non-uniform heat transfer of the sodium cooled fuel triangular arrayed rod, and the experimental results are required for the benchmark of the two correlations. With the further work, the proposed correlations may have a potential engineering value.

Bibliography

H. Austregesilo, C. Bals, and A. Hora. Athlet mod 3.0 cycle a: Models and methods. Technical report, Gesellschaft für Anlagen und Reaktorsicherheit (GRS) mbH, Munich, Germany, 2012.

G. Bandini, M. Polidori, A. Gerschenfeld, D. Pialla, S. Li, W. M. Ma, P. Kudinov, M. Jeltsov, K. Kööp, K. Huber, et al. Assessment of systems codes and their coupling with cfd codes in thermal–hydraulic applications to innovative reactors. *Nuclear Engineering and Design*, 281:22–38, 2015.

F. Belloni, G. Bandini, and M. Polidori. Investigation on the heat exchange efficiency of bayonet tube steam generator of lead cooled alfred reactor with relap 5 code. In *Proceedings of ICAP*, pages 2–6, 2011.

T. L. Bergman, F. P. Incropera, D. P. DeWitt, and A. S. Lavine. *Fundamentals of heat and mass transfer*. John Wiley & Sons, Inc., 2011.

H. J. Cha, K. N. Jang, and K. T. Kim. An allowable cladding peak temperature for spent nuclear fuels in interim dry storage. *Journal of Nuclear Materials*, 498:409–420, 2018.

S. K. Chang, D. J. Euh, S. Kim, H. S. Choi, H. Kim, Y. J. Ko, S. R. Choi, and H. Y. Lee. Experimental study of the flow characteristics in an sfr type 61-pin rod bundle using iso-kinetic sampling method. *Annals of Nuclear Energy*, 106:160–169, 2017.

S. K. Cheng and N. E. Todreas. Hydrodynamic models and correlations for bare and wire-wrapped hexagonal rod bundles-bundle friction factors, subchannel friction factors and mixing parameters. *Nuclear engineering and design*, 92(2):227–251, 1986.

X. Cheng and N. I. Tak. Cfd analysis of thermal–hydraulic behavior of heavy liquid metals in sub-channels. *Nuclear Engineering and Design*, 236(18):1874–1885, 2006.

X. Cheng and Y. Q. Yu. Local thermal–hydraulic behaviour in tight 7-rod bundles. *Nuclear Engineering and Design*, 239(10):1944–1955, 2009.

X. Cheng, H. Y. Chen, N. I. Tak, and A. Batta. Turbulent heat transfer to heavy liquid metals in circular tubes. In *ICHMT DIGITAL LIBRARY ONLINE*. Begel House Inc., 2004.

X. Cheng, A. Batta, G. Bandini, F. Roelofs, K. Van Tichelen, A. Gerschenfeld, M. Prasser, A. Papukchiev, U. Hampel, and W. M. Ma. European activities on crosscutting thermal-hydraulic phenomena for innovative nuclear systems. *Nuclear Engineering and Design*, 290:2–12, 2015.

G. P. Dobson and J. M. Neill. Sabre, user guide for version 4. *AEA Technology*, 1992.

J. K. Fink and L. Leibowitz. Thermodynamic and transport properties of sodium liquid and vapor. Technical report, Argonne National Lab., IL (United States), 1995.

M. H. Fontana, R. E. MacPherson, P. A. Gnadt, L. F. Parsly, and J. L. Wantland. Temperature distribution in the duct wall and at the exit of a 19-rod simulated lmfbr fuel assembly (ffm bundle 2a). *Nuclear Technology*, 24(2):176–200, 1974.

P. Gauthé, D. Pialla, D. Tenchine, A. Vasile, and D. Rochwerger. The phenix ultimate natural convection test. Technical report, American Nuclear Society, 555 North Kensington Avenue, La Grange Park, IL 60526 (United States), 2012.

A. Gerschenfeld. Wp2 : Complete core specification for sc/cfd simulations. Technical report, SESAME H2020 project progress meeting, 2018.

T. Ginsberg. Forced-flow interchannel mixing model for fuel rod assemblies utilizing a helical wire-wrap spacer system. *Nuclear Engineering and Design*, 22(1):43–50, 1972.

B. Grosjean and S. Li. Data package for phenix dissymmetrical test benchmarks. Technical report, CEA, 2015.

Li S. Grosjean, B. Datapackage for phenix asymmetrical test benchmarks. Technical report, DEN/DANS/DM2S/STMF/LMES, 2015.

T. P. Grunloh and A. Manera. A novel multi-scale domain overlapping cfd/sth coupling methodology for multi-dimensional flows relevant to nuclear applications. *Nuclear Engineering and Design*, 318:85–108, 2017.

J. Guidez and L. Martin. Phenix: Thirty years of operation for research, reactor renovation overview and prospects. Technical Report 2, International Atomic Energy Agency (IAEA), Vienna, Austria, 2004.

R. Hu and T. H. Fanning. A momentum source model for wire-wrapped rod bundles-concept, validation, and application. *Nuclear Engineering and Design*, 262:371–389, 2013.

K. Huber. *A multiscale method for mixed convective systems-Coupled calculations with ATHLET and OpenFOAM of the PHENIX NCT.* PhD thesis, Karlsruhe Institute of Technology, Karlsruhe, Germany, 2017.

IAEA. Liquid metal cooled reactors: Experience in design and operation. *Vienna: International Atomic Energy Agency*, page 103, 2007.

IAEA. Experience in design and operation. Technical report, IAEA-TECDOC-1569, Vienna, Austria, 2008.

H. Jasak, A. Jemcov, Z. Tukovic, et al. Openfoam: A c++ library for complex physics simulations. In *International workshop on coupled methods in numerical dynamics*, volume 1000, pages 1–20. IUC Dubrovnik, Croatia, 2007.

M. Kaviany. Laminar flow through a porous channel bounded by isothermal parallel plates. *International Journal of Heat and Mass Transfer*, 28(4):851–858, 1985.

W. S. Kim, Y. G. Kim, and Y. J. Kim. A subchannel analysis code matra-lmr for wire wrapped lmr subassembly. *Annals of Nuclear Energy*, 29(3):303–321, 2002.

E. Kreyszig. *Instructor's Manual For Advanced Engineering Mathematics.* John Wiley & Sons, Inc., 2006.

P Le Coz, JFm Sauvage, JP Serpantie, et al. Sodium-cooled fast reactors: the astrid plant project. In *Proceedings of ICAPP*, volume 11, pages 2–5, 2011.

X. J. Liu and N. Scarpelli. Development of a sub-channel code for liquid metal cooled fuel assembly. *Annals of Nuclear Energy*, 77:425–435, 2015.

B. R. Munson, T. H. Okiishi, W. W. Huebsch, and A. P. Rothmayer. *Fluid mechanics*. Wiley Singapore, 2013.

R. Nijsing and W. Eifler. Analysis of liquid metal heat transfer in assemblies of closely spaced fuel rods: A theoretical evaluation of two-dimensional temperature-and heat-flux distribution for conditions of turbulent axial flow at relatively low peclet numbers. *Nuclear Engineering and Design*, 10(1):21–54, 1969.

H. Ninokata, A. Efthimiadis, and N. E. Todreas. Distributed resistance modeling of wire-wrapped rod bundles. *Nuclear Engineering and Design*, 104(1):93–102, 1987.

E. H. Novendstern. Turbulent flow pressure drop model for fuel rod assemblies utilizing a helical wire-wrap spacer system. *Nuclear Engineering and Design*, 22(1):28–42, 1972.

OpenFOAM. Openfoam programmer's guide. *OpenFOAM Foundation*, 2(0), 2011.

A. Papukchiev, M. Jeltsov, K. Kööp, P. Kudinov, and G. Lerchl. Comparison of different coupling cfd–sth approaches for pre-test analysis of a tall-3d experiment. *Nuclear Engineering and Design*, 290:135–143, 2015.

D. Pialla, D. Tenchine, S. Li, P. Gauthe, A. Vasile, R. Baviere, N. Tauveron, F. Perdu, L. Maas, F. Cocheme, et al. Overview of the system alone and system/cfd coupled calculations of the phenix natural circulation test within the thins project. *Nuclear Engineering and Design*, 290:78–86, 2015.

M. N. Raj and K. Velusamy. Characterization of velocity and temperature fields in a 217 pin wire wrapped fuel bundle of sodium cooled fast reactor. *Annals of Nuclear Energy*, 87:331–349, 2016.

K. Rehme. Pressure drop correlations for fuel element spacers. *Nuclear technology*, 17(1): 15–23, 1973.

E. Robertson, V. Choudhury, S. Bhushan, and D. K. Walters. Validation of openfoam numerical methods and turbulence models for incompressible bluff body flows. *Computers & Fluids*, 123:122–145, 2015.

G. Rodriguez, F. Baque, and J. C. Astegiano. Evolution of sodium technology r&d actions supporting french liquid-metal fast breeder reactors. *Nuclear technology*, 150(1):3–15, 2005.

J. F. Sauvage. *Phénix: 30 Years of History: The Heart of a Reactor*. CEA Valrhô, 2004.

R. A. Seban and T. Shimazaki. Heat transfer to a fluid flowing turbulently in a smooth pipe with walls at constant temperature. Technical report, CALIFORNIA UNIV BERKELEY INST OF ENGINEERING RESEARCH, 1949.

C. A. Sleicher, A. S. Awad, and R. H. Notter. Temperature and eddy diffusivity profiles in nak. *International Journal of Heat and Mass Transfer*, 16(8):1565–1575, 1973.

V. Sobolev. Database of thermophysical properties of liquid metal coolants for gen-iv. *SCK-CEN, Mol, Belgium, BLG-1069*, 2011.

D. B. Spalding. A single formula for the "law of the wall". *Journal of Applied Mechanics*, 28(3):455–458, 1961.

C. W. Stewart, C. L. Wheeler, R. J. Cena, C. A. McMonagle, J. M. Cuta, and D. S. Trent. Cobra-iv: The model and the method. Technical report, Pacific Northwest Lab., Richland, WA (USA), 1977.

V. I. Subbotin, P. A. Ushakov, B. N. Gabrianovich, and A. B. Zhukov. Heat exchange during the flow of mercury and water in a tightly packed rod pile. *Atomic Energy*, 9(6): 1001–1009, 1961.

D. Tenchine, R. Baviere, P. Bazin, F. Ducros, G. Geffraye, D. Kadri, F. Perdu, D. Pialla, B. Rameau, and N. Tauveron. Status of cathare code for sodium cooled fast reactors. *Nuclear Engineering and Design*, 245:140–152, 2012.

G. Wang. A review of research progress in heat exchanger tube rupture accident of heavy liquid metal cooled reactors. *Annals of Nuclear Energy*, 109:1–8, 2017.

L. Wang, G. Wu, J. Wang, M. Jin, and Y. Song. Numerical investigation of the core outlet temperature fluctuation for the lead-based reactor. *Annals of Nuclear Energy*, 117:194–201, 2018.

J. L. Wantland. Orrible-a computer program for flow and temperature distribution in 19-rod lmfbr fuel subassemblies. *Nuclear Technology*, 24(2):168–175, 1974.

S. Wei, C. Wang, W. Tian, S. Qiu, and G. Su. Transient thermal-hydraulic evaluation of lead-bismuth fast reactor by coupling sub-channel and system analysis codes. *Nuclear Engineering and Design*, 337:228–235, 2018.

H. Yamaki, K. Inoue, A. Suzuoki, and S. Shingai. Current status of liquid metal-cooled fast breeder reactor safety research. *Hitachi Hyoron*, 64(8):611–614, 1982.

T. Yang, X. J. Liu, and X. Cheng. Investigation on heat transfer non-uniformity in rod bundle. *Nuclear Engineering and Design*, 265:222–231, 2013.

W. S. Yang. An lmr core thermal-hydraulics code based on the energy model. *Nuclear Engineering and Technology*, 29(5):406–416, 1997.

Y. J. Yoo, D. H. Hwang, et al. Development of a subchannel analysis code matra applicable to pwrs and alwrs. *Nuclear Engineering and Technology*, 31(3):314–327, 1999.

P. Zhao, J. Liu, Z. Ge, X. Wang, and X. Cheng. Cfd analysis of transverse flow in a wire-wrapped hexagonal seven-pin bundle. *Nuclear Engineering and Design*, 317:146–157, 2017.

C. Zhou, K. Huber, and X. Cheng. Validation of the modified athlet code with the natural convection test of the phenix reactor. *Annals of Nuclear Energy*, 59:31–46, 2013.

Appendix

A. Boundary conditions for Phenix dissymmetric test

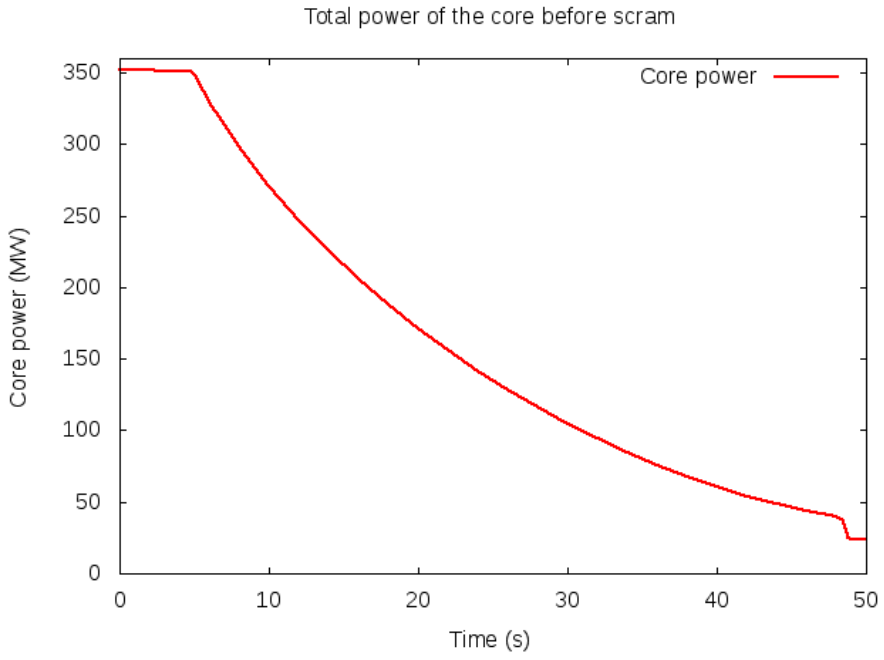

Figure A.1.: Total power of the core before SCRAM

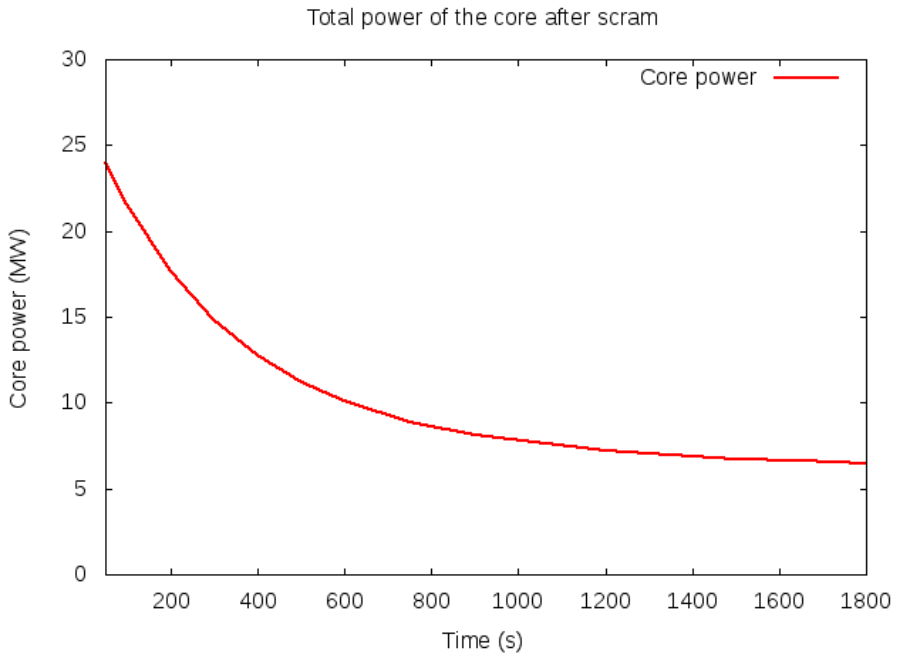

Figure A.2.: Total power of the core after SCRAM

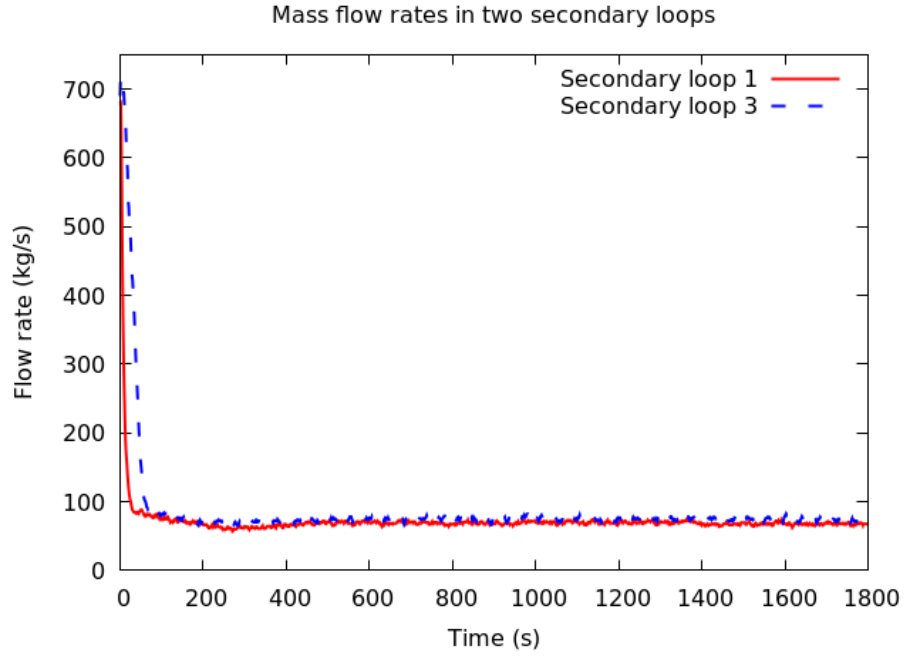

Figure A.3.: Mass flow rate in two secondary loops (long term)

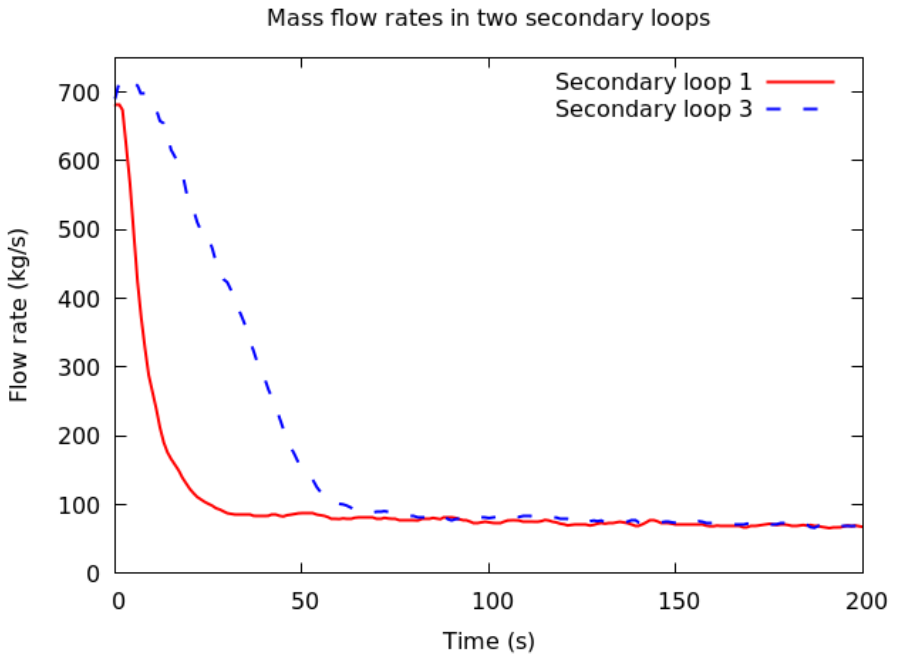

Figure A.4.: Mass flow rate in two secondary loops (short term)

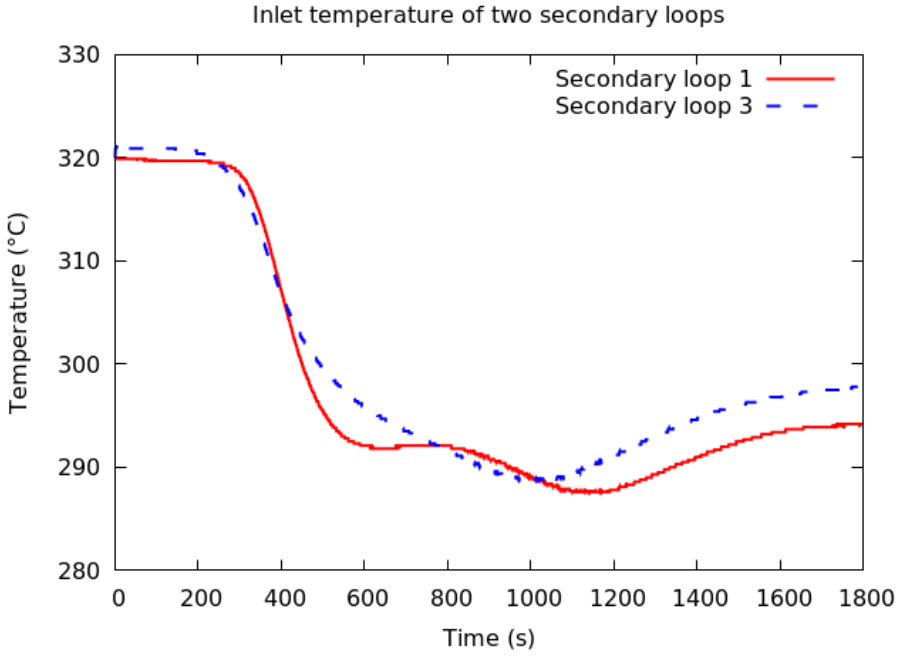

Figure A.5.: Inlet temperature of secondary circuits

B. Top view of the Phenix reactor

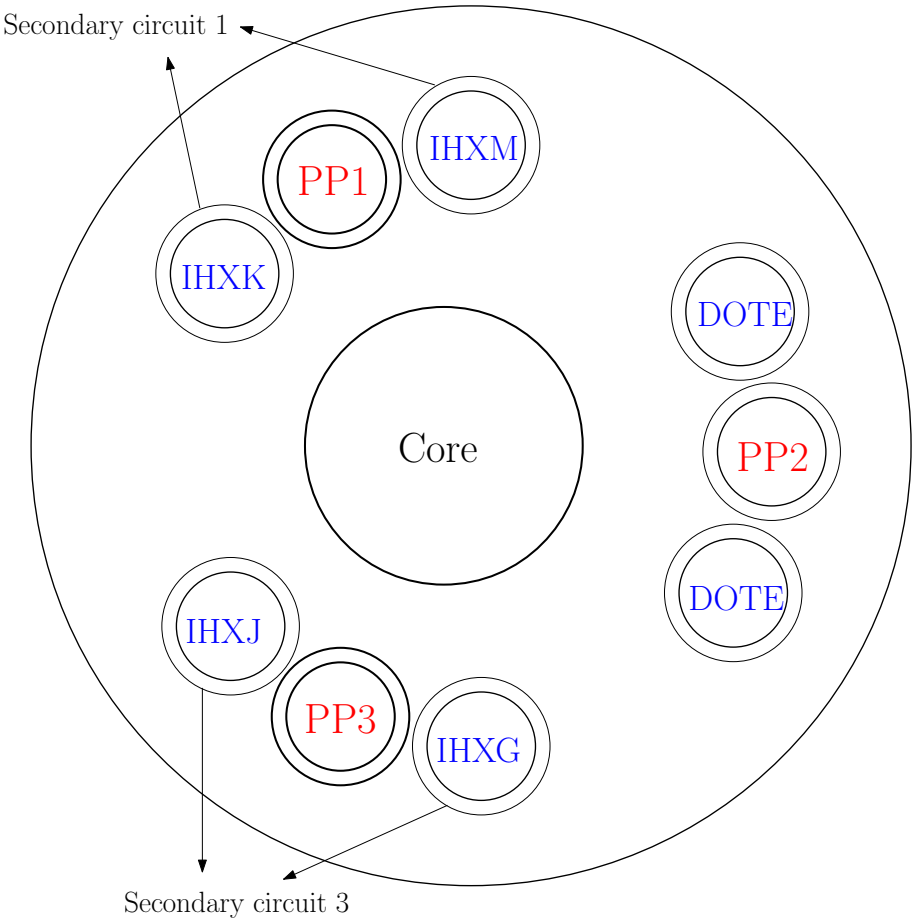

Figure B.6.: Top view of the Phenix reactor